

# *Fluorophores near metal interfaces*

## **Dissertation**

zur Erlangung des akademischen Grades

doctor rerum naturalium (Dr. rer. nat.)

vorgelegt der

Mathematisch-Naturwissenschaftlich-Technischen Fakultät  
(mathematisch-naturwissenschaftlicher Bereich)  
der Martin-Luther-Universität Halle-Wittenberg

von Herrn M.Sc. Krasimir Vasilev  
geb. am 20.08.1972 in Bourgas, Bulgarien

Gutachter:

1. Prof. Dr. Wolfgang Knoll
2. Prof. Dr. Gert Müller
3. Prof. Dr. Karl-Friedrich Arndt

Halle (Saale), 05.10.2004

**urn:nbn:de:gbv:3-000007884**

[<http://nbn-resolving.de/urn/resolver.pl?urn=nbn%3Ade%3Agbv%3A3-000007884>]

# Contents

<b>1. Introduction</b> .....	1
<b>2. Basic concepts</b> .....	3
<b>2.1. Surface plasmons</b> .....	3
2.1.1. Evanescent waves	
2.1.1.1. The surface plasmon - excitation..	
2.1.1.2. Prism coupling	
2.1.1.3. Tuning the environment of surface plasmons (dielectric layers).	
2.1.1.4. Transfer matrix formalism	
2.1.2. Plasmon resonance of small metal clusters.	
<b>2.2. Fluorescence</b> .....	8
2.2.1. Jablonski diagram	
2.2.2. Absorption and emission spectra – Stokes' shift	
2.2.3. Fluorescence lifetime and quantum yield.	
2.2.4. Fluorescence anisotropy	
2.2.5. Quenching of fluorescence	
2.2.6. Energy transfer	
2.2.7. Photobleaching	
<b>2.3. Excitation and emission rates of fluorescing dyes in the vicinity of a metal interface</b> ...	14
<b>2.4. Colloidal systems</b> .....	18
2.4.1. Definition, structure and size of the dispersed species	
2.4.2. Colloidal stability	
<b>3. Sample preparation and measurement techniques</b> .....	23
3.1. Self-assembled monolayers	
3.2. Layer-by-layer deposition	
3.2.1. Layer-by-layer deposition of polyelectrolytes.	
3.3. Template stripping of gold from mica	
3.4. Preparation of colloidal gold nanoparticles.	
3.5. Other sample preparation techniques	
3.6. Surface plasmon fluorescence spectroscopy (SPFS)	
3.7. Other measurement techniques	
<b>4. Fluorescence at a plane metal - dielectric interface</b> .....	32
<b>4.1. Experimental and theoretical evaluation of the fluorescence intensity emitted from an ensemble of fluorescing dyes</b> .....	33
4.1.1. Materials and methods	
4.1.2. Theoretical modelling	
4.1.3. Results and discussion	
4.1.4. Conclusion	
<b>4.2. Reduced photobleaching of chromophores close to a metal surface</b> .....	42
4.2.1. Experimental	
4.2.2. Theoretical modeling	
4.2.3. Results and discussion	
4.2.4. Conclusion	
<b>4.3. Single molecules fluorescence near a flat gold interface</b> .....	49
4.3.1. Introduction	

4.3.2. Experimental	
4.3.3. Results and discussion	
4.3.4. Conclusion	
<b>4.4. Cd-Se semiconducting nanoparticles in the vicinity of a gold interface.....</b>	<b>52</b>
4.4.1. Introduction	
4.4.2. Experimental	
4.4.3. Results and discussion	
4.4.4. Conclusion	
<b>5. Gold nanoparticles and gold nanowires – surface modification and synthesis.....</b>	<b>57</b>
<b>5.1. Surface Modification of Citrate-reduced Colloidal Gold Nanoparticles with 2-Mercaptosuccinic Acid.....</b>	<b>57</b>
5.1.1. Introduction	
5.1.2. Experimental Section	
5.1.3. Results and Discussion	
5.1.4. Conclusion	
<b>5.2. Synthesis of monolayer protected gold nanoparticles.....</b>	<b>73</b>
5.2.1. Introduction	
5.2.2. Materials and methods	
5.2.3. Results and discussion	
5.2.4. Conclusion	
<b>5.3. A simple, one step synthesis of gold nanowires in aqueous solution.....</b>	<b>81</b>
5.3.1. Introduction	
5.3.2. Experimental	
5.3.3. Results and discussion	
5.3.4. Conclusion	
<b>6. Plasmon coupling between a flat gold interface and gold nanoparticles....</b>	<b>92</b>
6.1. Introduction	
6.2. Experimental	
6.3. Results and discussion	
6.4. Conclusion	
<b>7. Summary.....</b>	<b>98</b>

## **1. Introduction**

Nowadays fluorescence spectroscopy is one of the dominant tools used in biomedical research and has become a dominant method enabling the revolution in medical diagnostics, DNA sequencing and genomics. The basic principles of fluorescence are well understood including factors which affect the emission, such as quenching, environmental effects, resonance energy transfer, and rotational motions. All these effects are used to study the structure and dynamics of macromolecules and the interactions of macromolecules with each other. Measurements of intensity, energy transfer, and anisotropy are also widely used in measurements of DNA hybridization, drug discovery, and fluorescence immunoassays.

It is known that the proximity of a metallic object alters the radiative and nonradiative rates of fluorescing species. This could be expressed in quenching (flat metal interface) or enhancement of the emitted fluorescence (rough metal surface or metal particles). The aim of this forward-looking work is to address the behavior of a fluorophore (or an ensemble of fluorophores) in the vicinity of a metal surface, because defining and understanding of the underlying phenomena is very important in all processes where a fluorescing dye is used with a metal interface (solar cells, LEDs) and particularly in sensor applications.

The alteration of the fluorescence lifetime in the vicinity of a flat metal interface has been studied in the past as the pioneering experiments were conducted by Drexhage et. al. In those experiments a separation distance between the chromophore and the metal film was provided by a multilayer sandwich built by the Langmuir-Blodgett deposition technique and as a chromophore a phosphorescent Europium Chelate was used. The theoretical framework of the impact of the nearby metallic surface on the excitation lifetime of the chromophore was developed by Chance et. al. A perfect agreement between theory and experiment was found.

Chapter 4 of this thesis will present a new experimental approach for studying fluorescing species excited by the surface plasmon field of the metal substrate. A well defined multilayer architecture involving the relatively new layer-by-layer deposition strategy was created thus providing precise experimental control of the separation distance between the metal layer and the fluorescing dye. As a fluorescing molecule was employed a commonly used in sensing organic dye, possessing directed transition dipole moment, much stronger oscillation strength than the europium complex used in the past and thus putting our system much closer to the real life in sensing and fluorescing microscopy. This chapter answers in a precise manner how the fluorescence intensity changes with the separation distance between a metal layer and a

fluorescing dye in Kretschmann configuration. The fluorescence intensity, the angular distribution of the fluorescence and the photobleaching rate of an ensemble of fluorescing dyes were experimentally determined and compared with that predicted by the theory. In addition the problem was addressed on single molecule level. The applicability of our experimental and theoretical model for studying other fluorescing species as Cd-Se nanoparticles is also demonstrated.

After the assessment of the behavior of the fluorescing dye in the proximity of a flat gold interface it was interesting to turn to more complex metal objects. It is known that in the vicinity of metal particles or metal islands fluorescence could be enhanced orders in magnitude than in planar system. The attention of the author was drawn to gold nanoparticles since they provide several interesting features as finite size effect, curved interface, local plasmon resonance, size and shape control. Though, research on gold nanoparticles dates at least from the work of Faraday in the middle of the 19<sup>th</sup> century, today they are still of scientific interest due to their potential in numerous applications as sensing, cell biology, electronics, photonics, catalysis, etc. In chapter 5 the surface modification of citrate reduced gold nanoparticles by 2-mercaptosuccinic acid will be presented. Series of comparative tests unambiguously demonstrated the success of the surface modification and led to the novel method of synthesis of monolayer protected gold nanoparticles with size above 10 nm, which is a lack in this field. Inspired of the potential of the new system more detailed investigations were carried out, which resulted in the discovery of an interesting aging effect and the synthesis of gold nanowires. In chapter 6.3. the synthesis in an aqueous solution of long aspect ratio gold nanowires will be described for the first time. The length of the gold wires is in the order of micrometers and the cross section down to 15 nm.

In chapter 6 a model system allowing for the study the optical response of gold nanoparticles in the vicinity of a flat gold interface was constructed. The gold nanoparticles were placed precisely at different separation distance to the gold substrate and their optical response at wavelength range between 480 and 780 nm determined. This system could serve for the study of fluorophores in the enhanced gap mode between the substrate and the gold nanoparticles.

## 2. Basic concepts

This chapter is intended to give a basic idea about the theory behind the work presented in this thesis. Fundamental theoretical considerations will be outlined. Reference literature sources will be suggested for detailed description of the underlying phenomena.

### 2.1. Surface plasmons

#### 2.1.1. Evanescent waves

One example for the existence of evanescent waves is the well known total internal reflection of a plane electromagnetic wave between two interfaces with different refractive indices, for example a glass slide with refractive index  $n_1$  in contact with an optically less dense medium like air, with refractive index  $n_2$  ( $n_2=1$ ,  $n_1>n_2$ ). The geometry is schematically depicted in Fig. 2.1.a. If the reflected light is recorded as a function of angle of incidence,  $\theta$ , the reflectivity,  $R$ , reaches unity when one approaches the critical angle,  $\theta_c$ , for total internal reflection. A closer inspection of the electromagnetic field distribution in the immediate vicinity of the interface shows that above  $\theta_c$  the light intensity does not fall abruptly to zero in air, but there is instead a harmonic wave travelling parallel to the surface with an amplitude decaying exponentially normal to the surface. The depth of penetration  $l$  given by:

$$l = \frac{\lambda}{2\pi\sqrt{(n_1 \cdot \sin \theta)^2 - 1}} \quad 2.1.$$

and is found to be in the order of the wavelength of light. This type of waves is called evanescent wave.<sup>1</sup>

##### 2.1.1.1. Surface plasmon. Excitation of surface plasmon.

Surface electromagnetic modes can only be excited at interfaces between two media with dielectric constants of opposite signs. So, here the interface between a metal with complex dielectric function  $\bar{\epsilon}_m = \epsilon'_m + i\epsilon''_m$  and a dielectric material  $\bar{\epsilon}_d = \epsilon'_d + i\epsilon''_d$  is considered. At specific conditions the evanescent wave penetrating through the dielectric/metal interface can couple to the free electron gas in the metal thus exciting surface plasmon resonance.

In this work surface plasmons (SP) are excited by optical waves from a laser source. For the excitation of surface plasmons, only the optical wave vector projection to the x-direction

(parallel to the interface)  $k_{ph}^0$  is the relevant parameter. For a simple reflection of a laser beam (with photon energy  $\hbar\omega_L$ ) at a planar dielectric/metal interface, this means that by changing the angle of incidence,  $\theta$ , one can tune  $k_{ph}^0 = k_{ph} \cdot \sin\theta$  from zero at a normal incidence to a full wave vector  $k_{ph}$  at a grazing incidence.

The so called coupling angle, at which efficient excitation of surface plasmon is possible, is given by the energy and momentum matching conditions between optical waves and surface plasmons. (See fig. 2.1.b.)

$$k_{sp}^o = k_{ph}^o = n_1 \frac{\omega}{c} \sin\theta \quad 2.2.$$

where,  $k_{sp}^o$  is the SP wavevector,  $k_{ph}^o$  is the  $x$  - component of the wavevector of the incident light,  $c$  is the speed of light in vacuum and  $\omega$  is the angular frequency. Detailed description of the evanescent wave optics and in particular surface plasmons can be found in the literature.<sup>2,3</sup>

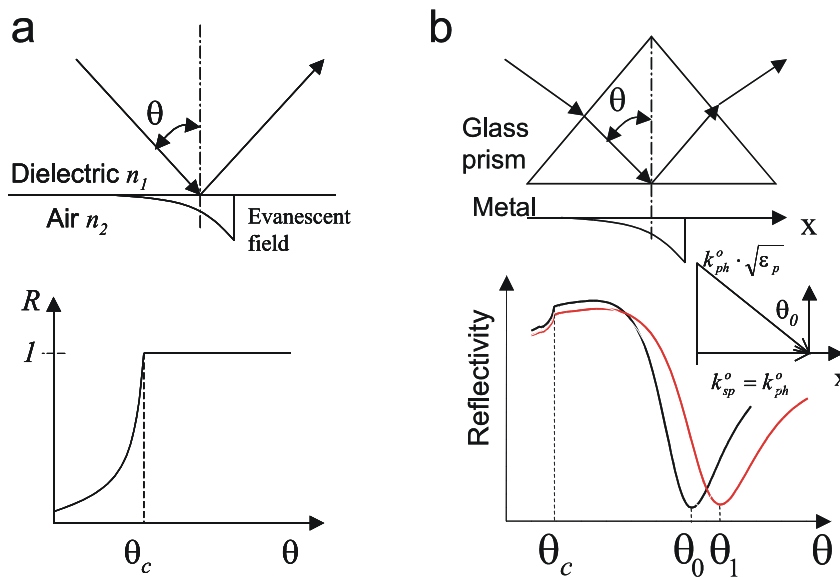


Figure 2.1. a) Total internal reflection of a plane wave at dielectric/air interface.

b) Excitation of surface plasmon resonance in Kretschmann geometry at metal/air ( $\theta_0$ ) and metal/dielectric layer/air ( $\theta_1$ ) interface.

### 2.1.1.2. Prism coupling

In order the momentum matching conditions to be fulfilled the  $x$  - component of the wavevector of the incident light should be sufficiently long. Among the developed methods to increase the momentum of the light in order to couple to surface plasmons the most predominant

techniques are prism coupling and grating coupling. Here only prism coupling in Kretschmann<sup>4</sup> configuration will be addressed, since that way of SP excitation was used in the experiments.

Briefly, a thin metal film (approximately 45-50 nm thick) is evaporated directly onto the base of a high refractive index prism or onto a glass slide, which is then index-matched to the base of prism (Fig. 2.1.b). If the intensity of the reflected light is measured as a function of the angle of incidence ( $\theta$ ), first at a given angle (depending on the refractive index of the prism) the angle of total internal reflection,  $\theta_c$ , is reached. Below  $\theta_c$  the reflectivity is high because the metal acts as a mirror. Above  $\theta_c$ , when the momentum matching conditions are satisfied, a relatively narrow dip (this will depend on the metal and the wavelength) in the reflectivity (at  $\theta_0$  in fig. 2.1.b) indicates the excitation of surface plasmon.

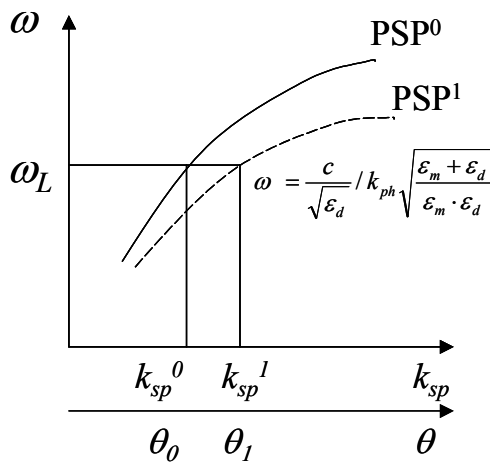


Figure 2.2. Dispersion relation,  $\omega$  vs.  $k_{sp}$  of plasmon surface polaritons at a metal/air and at a metal/dielectric layer/ air interface.

The surface plasmon modes obey a known dispersion relation,  $\omega$  versus  $k_{sp}$ . This is schematically depicted in fig. 2.2. The solid curve represents the dispersion of surface plasmons at a metal (e. g. gold)/air interface (PSP<sup>0</sup>). The horizontal lines at  $\omega_L$  intercepts the dispersion curve at  $k_{sp}^0$  and thus defines the coupling angle  $\theta_0$ . (Equation 2.2.)

### 2.1.1.3. Tuning the environment of surface plasmons (dielectric layers).

A thin dielectric layer deposited on the gold layer will shift the dispersion curve to a higher momentum SPS<sup>1</sup> (Dashed curve in fig. 2.2.).

$$k_{sp}^1 = k_{sp}^0 + \Delta k_{sp} \tag{2.3}$$

which according to equation 2.2 shifts the resonance to higher angle  $\theta_1$ . One example is shown in fig. 2.1.b. From this shift and Fresnel's equations one can calculate the optical thickness of the coated dielectric layer.



2.1.1.4. Transfer Matrix Formalism.

The transfer matrix method is a commonly used technique for the evaluation of the electric and magnetic fields of a layered medium upon plane wave illumination.

This method will be illustrated by calculating the reflection and transmission of electromagnetic radiation through a thin film surrounded by infinite media such this shown in fig. 2.3. and described by:

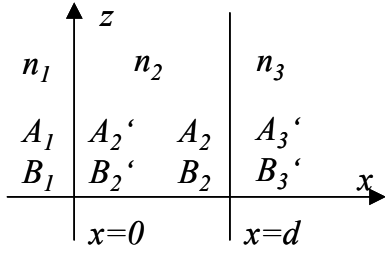
$$n(x) = \begin{cases} n_1, x < 0, \\ n_2, 0 < x < d, \\ n_3, d < x, \end{cases} \quad 2.4$$


Fig2.3. A thin layer of dielectric medium.

where  $n_1$ ,  $n_2$  and  $n_3$  are the refractive indices and  $d$  is the thickness of the film. Since the whole medium is homogeneous in  $z$  and  $y$  direction (i.e.  $\partial n / \partial z = 0$ ) the electric field that satisfies Maxwell's equations has the form

$$E = E(x)e^{i(\omega t - \beta z)} \quad 2.5.$$

where  $\beta$  is the  $z$  component of the wave vector and  $\omega$  is the frequency. It is assumed that the electromagnetic wave is propagating in the  $xz$  plane and it is further assumed that the electric field is either a  $s$  wave (with  $\mathbf{E} \parallel y$ ) or a  $p$  wave (with  $\mathbf{H} \parallel y$ ). The electric field  $E(x)$  consists of a right travelling (transmitted) wave and a left travelling (reflected) wave and can be written as

$$E(x) = \text{Re}^{-ik_x x} + L e^{ik_x x} \equiv A(x) + B(x) \quad 2.6.$$

where  $\pm k_x$  are the  $x$  component of the wave vector and  $A(x)$  and  $B(x)$  are the amplitudes of the transmitted and reflected wave, respectively. To illustrate this method it is defined:  $A_1 = A(0^-)$ ,  $B_1 = B(0^-)$ ,  $A_2' = A(0^+)$ ,  $B_2' = B(0^+)$ ,  $A_2 = A(d^-)$ ,  $B_2 = B(d^-)$ ,  $A_3 = A(d^+)$ ,  $B_3 = B(d^+)$ . If one represent the two amplitudes of  $E(x)$  as column vectors, they are related by:

$$\begin{aligned} \begin{pmatrix} A_1 \\ B_1 \end{pmatrix} &= D_1^{-1} D_2 \begin{pmatrix} A_2' \\ B_2' \end{pmatrix} \equiv D_{12} \begin{pmatrix} A_2' \\ B_2' \end{pmatrix}, \\ \begin{pmatrix} A_2' \\ B_2' \end{pmatrix} &= P_2 \begin{pmatrix} A_2 \\ B_2 \end{pmatrix} = \begin{pmatrix} e^{i\phi_2} & 0 \\ 0 & e^{-i\phi_2} \end{pmatrix} \begin{pmatrix} A_2 \\ B_2 \end{pmatrix}, \\ \begin{pmatrix} A_2 \\ B_2 \end{pmatrix} &= D_2^{-1} D_3 \begin{pmatrix} A_3' \\ B_3' \end{pmatrix} \equiv D_{23} \begin{pmatrix} A_3' \\ B_3' \end{pmatrix}, \end{aligned} \quad 2.7.$$

where  $D_1$ ,  $D_2$  and  $D_3$  are the dynamical matrices.  $P_2$  is the propagation matrix, which accounts for propagation through the bulk of the layer, and  $\phi_2$  is given by  $\phi_2 = k_{2x}d$ .

The matrices  $D_{12}$  and  $D_{23}$  may be regarded as transmission matrices that link the amplitudes of the waves on the two sides of the interface and are given by

$$D_{12} = \begin{pmatrix} \frac{1}{2} \left( 1 + \frac{k_{2x}}{k_{1x}} \right) & \frac{1}{2} \left( 1 - \frac{k_{2x}}{k_{1x}} \right) \\ \frac{1}{2} \left( 1 - \frac{k_{2x}}{k_{1x}} \right) & \frac{1}{2} \left( 1 + \frac{k_{2x}}{k_{1x}} \right) \end{pmatrix} \quad \text{for a } s \text{ wave}$$

$$D_{12} = \begin{pmatrix} \frac{1}{2} \left( 1 + \frac{n_2^2 k_{1x}}{n_1^2 k_{2x}} \right) & \frac{1}{2} \left( 1 - \frac{n_2^2 k_{1x}}{n_1^2 k_{2x}} \right) \\ \frac{1}{2} \left( 1 - \frac{n_2^2 k_{1x}}{n_1^2 k_{2x}} \right) & \frac{1}{2} \left( 1 + \frac{n_2^2 k_{1x}}{n_1^2 k_{2x}} \right) \end{pmatrix} \quad \text{for a } p \text{ wave}$$
2.8.

The expressions for  $D_{23}$  are similar to those of  $D_{12}$  except the subscript indices to be replaced with 2 and 3. The last two equations can be written as

$$D_{12} = \frac{1}{t_{12}} \begin{pmatrix} 1 & r_{12} \\ r_{12} & 1 \end{pmatrix} \quad 2.9.$$

where  $t_{12}$  and  $r_{12}$  are the Fresnel transmission and reflection coefficients.

The amplitudes  $A_1$ ,  $B_1$  and  $A_3'$ ,  $B_3'$  are related by

$$\begin{pmatrix} A_1 \\ B_1 \end{pmatrix} = D_1^{-1} D_2 P_2 D_2^{-1} D_3 \begin{pmatrix} A_3' \\ B_3' \end{pmatrix}. \quad 2.10.$$

Column vectors representing the plane wave amplitudes are related by a product of 2 x 2 matrices in sequence. Each side of an interface is represented by a dynamical matrix, and the bulk of each layer is represented by a propagation matrix. Such a recipe can be extended to the case of multiplayer structures. If  $A_n'$  and  $B_n'$  are the amplitudes in the last layer then

$$\begin{pmatrix} A_0 \\ B_0 \end{pmatrix} = \begin{pmatrix} M_{11} & M_{12} \\ M_{21} & M_{22} \end{pmatrix} \begin{pmatrix} A_n' \\ B_n' \end{pmatrix} \quad 2.11.$$

and reflectance  $R$  and transmittance  $T$  are given by:

$$R = |r|^2 = \left| \frac{M_{21}}{M_{11}} \right|^2, \quad T = \frac{n_n \cos \theta_n}{n_0 \cos \theta_0} |t|^2 = \frac{n_n \cos \theta_n}{n_0 \cos \theta_0} \left| \frac{1}{M_{11}} \right|^2, \quad 2.12.$$

Details regarding the full mathematical treatment can be found in the literature.<sup>5, 6</sup>

### 2.1.2. Plasmon resonance of small metal clusters.

In this section the optical response of small metal clusters due to interaction with light will be addressed. The plasmon resonance is a size dependent phenomenon. Bulk metal reflects

light whereas small molecular clusters do not show any kind of plasmon resonance. This is due to the lack of *quasi* delocalised electrons that are necessary for the interaction with light. On the contrary the electrons between metal atoms in small clusters are localised.

It is common to express the optical properties in terms of absorption and scattering cross section  $\sigma_{\text{abs}}$  and  $\sigma_{\text{sca}}$ . Since there are no purely absorbing and purely scattering particles, practically, it is considered an extinction cross section, which is the sum of both  $\sigma_{\text{abs}}$  and  $\sigma_{\text{sca}}$  or  $\sigma_{\text{ext}} = \sigma_{\text{abs}} + \sigma_{\text{sca}}$ . In the simplest case of a spherical single sized metal clusters in the *quasi-static* regime, where the radius is much smaller than the wavelength ( $R \ll \lambda$ ), the resonance wavelength or frequencies of plasma resonance will be related to the extinction cross section as:

$$\sigma_{\text{ext}}(\omega) = 9 \frac{\omega}{c} \varepsilon_m^{3/2} V_0 \frac{\varepsilon_2(\omega)}{[\varepsilon_1(\omega) + 2\varepsilon_m]^2 + \varepsilon_2(\omega)^2} \quad 2.13.$$

here the wavevector is expressed as  $|k| = \omega/c$ ,  $V_0 = (4\pi/3)R^3$  is the particle volume,  $\varepsilon_m$  is the dielectric function of the embedding medium, and  $\varepsilon(\omega)$  is the dielectric function of the particle material. The extinction cross section is due to dipolar absorption, only. Both the scattering cross section, being proportional to  $(|k|R)^6 / |k|^2$  and higher multidipolar contributions, e.g. the quadrupole extinction ( $\sim (|k|R)^5 / |k|^2$ ) and quadrupole scattering ( $\sim (|k|R)^{10} / |k|^2$ ), are strongly suppressed in this size region ( $R \ll \lambda$ ).

The cross section defined by equation 2.12. has a resonance being at frequency where the denominator  $[\varepsilon_1(\omega) + 2\varepsilon_m]^2 + \varepsilon_2(\omega)^2$  takes its minimum.

The position and shape of the plasmon resonance will depend not only on the size and dielectric functions of the clusters and the surrounding medium. It will depend also on the shape of the particles, aggregations, interactions with substrate etc. The electrodynamics of metal clusters is quantitatively described by the Mie theory and can be found in the applied references.<sup>7, 8</sup>

## 2.2. Fluorescence

Luminescence is the emission of photons from an excited electronic state. Depending on the nature of the ground and excited state luminescence is divided into two types. In a singlet excited state, the electron in the higher-energy orbital has the opposite spin orientation as the second electron in the lower orbital, the two electrons are paired. In a triplet state these electrons are unpaired, their spins have the same orientation. Return to the ground state from an excited

singlet state does not require an electron to change its spin orientation. A change in spin orientation is needed for a triplet state to return to the singlet ground state. Fluorescence is an emission which results from the return to the lower orbital of the paired electron. Such transitions are quantum mechanically allowed and the emissive rates are typically in the range of nanoseconds. Phosphorescence is the emission which results from transition between states of different multiplicity, generally a triplet state returning to a singlet ground state. Such transitions are not allowed and the emissive rates are slow (from milliseconds to seconds).

Substances, which show significant fluorescence generally possess delocalised electrons formally present in conjugated double bonds. More about the principles of fluorescence can be found in the nice textbook of Lakowicz.<sup>9</sup>

### 2.2.1. Jablonski diagram

The absorption and emission of light is nicely illustrated by the energy-level diagram of A. Jablonski<sup>10</sup> and is shown in fig. 2.9. The ground, first and second electronic states are depicted by  $S_0$ ,  $S_1$ , and  $S_2$  respectively. At each of these electronic levels the fluorophores can

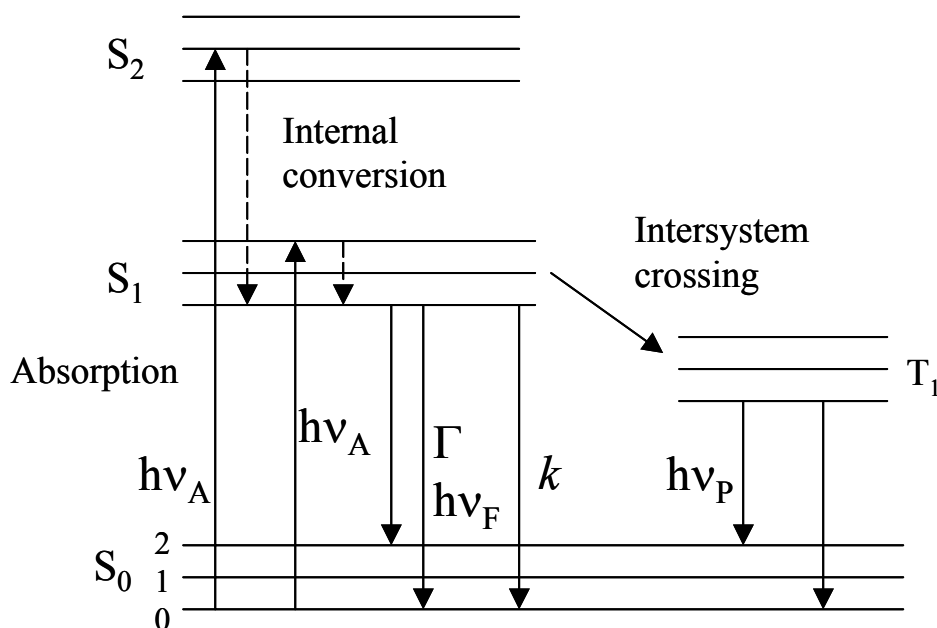


Figure 2.9. The Jablonski diagram.

exist in a number of vibrational energy levels, depicted by 0, 1, 2, etc. The transitions between various electronic levels are vertical. The light absorption occurs instantaneous in about  $10^{-15}$  seconds, a time too short for significant displacement of nuclei (Franck-Condon principle).

Following light absorption, several processes can occur. The fluorophore is usually excited to some higher vibrational level of either  $S_1$  or  $S_2$ . Molecules in condensed phase usually rapidly relax to the lowest vibrational level of  $S_1$  in about  $10^{-12}$  sec. Since fluorescence lifetimes are typically near  $10^{-8}$  sec, internal conversion is generally complete prior the emission. Hence, fluorescence emission generally results from thermally equilibrated excited state.

Molecules in the  $S_1$  state can also undergo conversion to the first triplet state  $T_1$ . Emission from  $T_1$  is called phosphorescence, and generally is shifted to longer wavelength relative to the fluorescence. Conversion of  $S_1$  to  $T_1$  is called intersystem crossing. Transition from  $T_1$  to the ground state is forbidden, and as a result the rate constant of such emission is several order of magnitude smaller than those of fluorescence.

### 2.2.2. Absorption and emission spectra – Stokes' shift

A plot of fluorescence intensity vs. wavelength is called fluorescence spectrum. The absorption and emission spectra of 1,1',3,3,3',3'-hexamethylindico-cyanine iodide (DiIC1(5)) are shown in fig. 2.5. Except for atoms in vapour phase, one invariably observes shift of the emission to a longer wavelength relative to the absorption. This phenomenon is caused by energy losses between excitation and emission and was first observed by Stokes in 1852. One common case for Stokes shift is the rapid decay to the lowest vibrational level of  $S_1$ . Furthermore

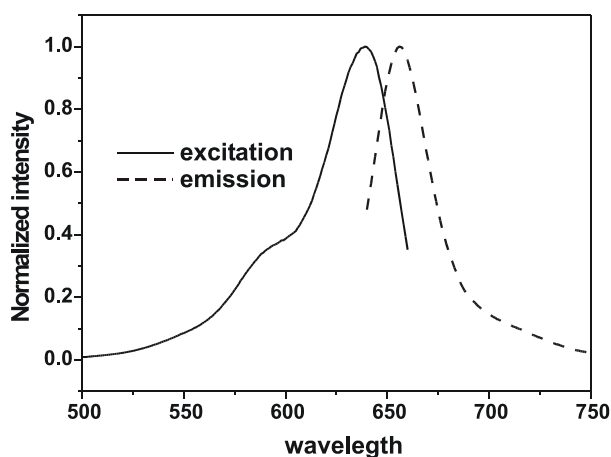


Figure 2.5. Excitation and fluorescence emission spectra of (1,1',3,3,3',3'-hexamethylindico-cyanine iodide (DiIC1(5)))

fluorophores generally decay to excited vibrational level of  $S_0$ , resulting in further loss in vibrational energy. In addition to these effects fluorophores can exhibit further Stokes' shift due to solvent effect and excited state reactions. Generally the fluorescence emission spectrum appear to be a mirror image of the absorption spectrum. The symmetric nature of these spectra is

a result of the same transition being involved in both absorption and emission, and the similarities among the vibrational energy levels of  $S_0$  and  $S_1$ .

### Fluorescence lifetime and quantum yield.

The fluorescence lifetime and quantum yield are two important, frequently measured parameters. The quantum yield is the ratio of the number of photons emitted to the number absorbed. The fraction of fluorophores which decay through emission, and hence the quantum yield, is given by:

$$Q = \frac{\Gamma}{\Gamma + k} \quad 2.14.$$

here  $\Gamma$  and  $k$  denote the radiative emission rate and the nonradiative rate (both are shown in fig. 2.4.) and both depopulate the excited state. It is clear that that  $Q$  can be close to unity only if  $k \ll \Gamma$ . Here,  $k$  denotes all possible nonradiative processes – Stokes' shift, quenching, etc.

The lifetime of the excited state is defined by the average time the molecule spend in excited state prior to return to the ground state.

$$\tau = \frac{1}{\Gamma + k} \quad 2.15.$$

Since the fluorescence emission is a random process and only few molecules will emit their photons at  $t = \tau$ . The lifetime is an average value of the time spent in the excited state.

### 2.2.3. Fluorescence anisotropy

Fluorophores preferentially absorb light whose electric field vectors are aligned parallel to the transition moment of the fluorophore. The transition moment has a defined orientation in the fluorophore. In an isotropic medium the fluorophores are oriented randomly. Upon excitation with polarized light, one selectively excites those fluorophore molecules whose absorption transition dipole is parallel to the electric vector of the excitation. This selective excitation of a partially oriented population of fluorophores results in a partially polarized fluorescence emission. The transition moments for absorption and emission have a fixed orientation within each fluorophore, and the relative angle between these moments determines the maximum measured anisotropy. The fluorescence anisotropy ( $r$ ) and polarization ( $P$ ) are defined by:

$$r = \frac{I_{\parallel} - I_{\perp}}{I_{\parallel} + 2I_{\perp}} \quad 2.16.$$

$$P = \frac{I_{\parallel} - I_{\perp}}{I_{\parallel} + I_{\perp}} \quad 2.17.$$

where  $I_{\parallel}$  and  $I_{\perp}$  are the fluorescence intensities of the vertically and horizontally polarized emission, when the sample is excited with vertically polarized light. From the fluorescence anisotropy the angle of displacement between absorption and emission dipole moment  $\beta$  can be found

$$r = \frac{3 \cos^2 \beta - 1}{2}. \quad 2.18.$$

Details regarding the experimental assessment of  $\beta$  will be described in Chapter 4.

#### 2.2.4. Quenching of the fluorescence

Fluorescence quenching refers to any process which decreases the fluorescence intensity of a given substance. A variety of processes can result in quenching. These include excited state reactions, energy transfer, complex formation and collisional quenching.

Another type of fluorescence quenching will be addressed in this thesis. This is the influence of a metal interface on the fluorescence emission of the fluorophore. Nearby metal surfaces can respond to the oscillating dipole and modify the rate of emission and the special distribution of the radiated energy. The electric field felt by a fluorophore is affected by interactions of the incident light with the nearby metal surface and also by interaction of the fluorophore oscillating dipole with the metal surface. Additionally, the fluorophore oscillating dipole induces a field in the metal. These interactions can increase or decrease the field incident on the fluorophore and increase or decrease the radiative decay rates. Detailed description of this phenomenon can be found in the excellent reviews of Barns<sup>11</sup> and Lakowicz<sup>12</sup>. This problem will be addressed in details in Chapter 4.

#### 2.2.5. Energy transfer

Fluorescence energy transfer is the transfer of the excited state energy from a donor to an acceptor. The transfer occurs without the appearance of a photon, and is primarily a result of dipole-dipole interactions between the donor and the acceptor. The rate of energy transfer depends on the extend of overlap of the emission spectrum of the donor with the absorption

spectrum of the acceptor, the relative orientation of the donor and acceptor transition dipoles, and the distance between donor and acceptor.

The rate of energy transfer from a specific donor to a specific acceptor is given by:

$$k_T = \frac{1}{\tau_d} \left( \frac{R_0}{r} \right)^6 \quad 2.19.$$

where  $\tau_d$  is the lifetime of the donor in the absence of acceptor,  $r$  is the distance between the donor and acceptor, and  $R_0$  is the characteristic distance called Förster distance, at which the efficiency of transfer is 50 %.<sup>13</sup>

### 2.2.6. Photobleaching

Photobleaching occurs when a fluorophore permanently loses the ability to fluoresce due to photon-induced chemical damage and covalent modification. Upon transition from an excited singlet state to the excited triplet state, fluorophores may interact with another molecule to produce irreversible covalent modifications. The triplet state is relatively long-lived with respect to the singlet state, thus allowing excited molecules a much longer timeframe to undergo chemical reactions with components in the environment. The average number of excitation and emission cycles that occur for a particular fluorophore before photobleaching is dependent upon the molecular structure and the local environment. Some fluorophores bleach quickly after emitting only a few photons, while others that are more robust can undergo thousands or millions of cycles before bleaching.

An important class of photobleaching events are photodynamic, meaning they involve the interaction of the fluorophore with a combination of light and oxygen. Reactions between fluorophores and molecular oxygen permanently destroy fluorescence and yield a free radical singlet oxygen species that can chemically modify other molecules. The amount of photobleaching due to photodynamic events is a function of the molecular oxygen concentration and the proximal distance between the fluorophore, oxygen molecules, and other compounds. Photobleaching can be reduced by limiting the exposure time of fluorophores to illumination or by lowering the excitation energy. As it will be demonstrated in Chapter 4 the proximity of a metal interface also can increase the photobleaching lifetime of the fluorophore.



### 2.3. Excitation and emission rates of fluorescing dyes in the vicinity of a metal interface

In the following, the calculation of excitation and emission rates of fluorescing dyes in the vicinity of a metal interface will be presented.

A sketch of the idealised sample geometry is given in Fig. 2.6. The same geometry was used in the experimental study described in Chapter 4. A planar multilayer system is considered consisting of an infinitely extended dielectric medium (a glass prism in the experimental realisation) with a (frequency-dependent) dielectric constant  $\epsilon_{\text{prism}}$ , a gold layer with a thickness

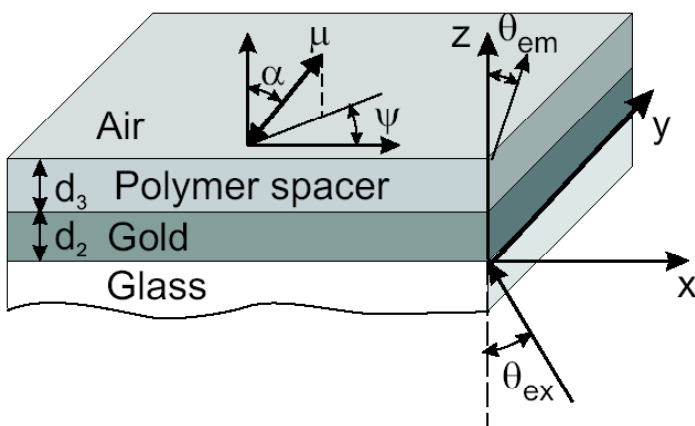


*Fig. 2.6. Sketch the multilayered system with a chromophore being placed at the interface between air and spacer layer. Only one transition dipole  $\mu$  is indicated for clarity, definition of  $\alpha$  and  $\psi$  is identical for absorption and emission dipole*

$d_{\text{gold}}$  (roughly 50 nm) and  $\epsilon_{\text{gold}}$ , a spacer layer ( $\epsilon_{\text{spacer}}$ ,  $d_{\text{spacer}}$ ) and air ( $\epsilon_{\text{air}} = 1$ ) filling the second half space. The dye is located at an infinitely small distance from the interface between spacer and air on the spacer side and assumed to be randomly distributed in the plane, additionally a random orientational distribution is assumed. It is characterised by its nonradiative decay rate  $P_{\text{nr}}$ , and by its absorption and emission dipoles,  $\mu_{\text{ex}}$  and  $\mu_{\text{em}}$ . The orientation of the dipoles is described by pairs of polar angle  $\alpha$  and azimuthal angle  $\psi$  ( $\alpha_{\text{ex}}$ ,  $\psi_{\text{ex}}$ ,  $\alpha_{\text{em}}$ ,  $\psi_{\text{em}}$ ), the angle  $\beta_{\text{em,ex}}$  between  $\mu_{\text{ex}}$  and  $\mu_{\text{em}}$  is a fixed quantity for a given molecule. A plane electromagnetic wave with the excitation wavelength  $\lambda_{\text{ex}}$  is directed on the system under an angle  $\theta_{\text{ex}}$  relative to the surface normal from the glass side. Only TM (transverse-magnetic)-polarisation is considered here because TE (transverse electric) polarisation does not couple to the surface plasmon and therefore does not excite significant fluorescence. The emitted fluorescence with wavelength  $\lambda_{\text{em}}$  is collected in the plane of incidence at some angle  $\theta_{\text{em}}$  in either of the two half spaces ("through prism" or "through air")

For a single dye molecule, the measured fluorescence intensity  $I_{\text{sm}}$  is obtained as

$$I_{sm} = P_{ex} \frac{P_{rad,det}}{P_{rad,tot} + P_{nr}} \quad 2.20$$

with  $P_{ex}$  being the excitation rate,  $P_{rad,det}$  the rate of photons emitted in direction of the detector,  $P_{rad,tot}$  the total electromagnetic decay rate and  $P_{nr}$  the nonradiative decay rate.

The excitation rate  $P_{ex}$  is calculated as

$$P_{ex} = |\boldsymbol{\mu}_{ex} \cdot \mathbf{E}_{ex}|^2 \quad 2.21.$$

with  $\boldsymbol{\mu}_{ex}$  being the absorption dipole moment of the dye and  $\mathbf{E}_{ex}$  the electric field generated by the exciting plane wave at the dipole position.  $\mathbf{E}_{ex} = \mathbf{E}_{ex}(\theta_{ex}, \epsilon_{prism}, \epsilon_{gold}, \epsilon_{spacer}, \epsilon_{air}, d_{gold}, d_{air})$  is calculated by a transfer matrix algorithm (see section 2.1.1.4.). The squared electrical field strength at the dipole position parallel and perpendicular at different separation distance to a gold layer are shown in fig. 2.7. The different contribution of both parallel and perpendicular dipoles

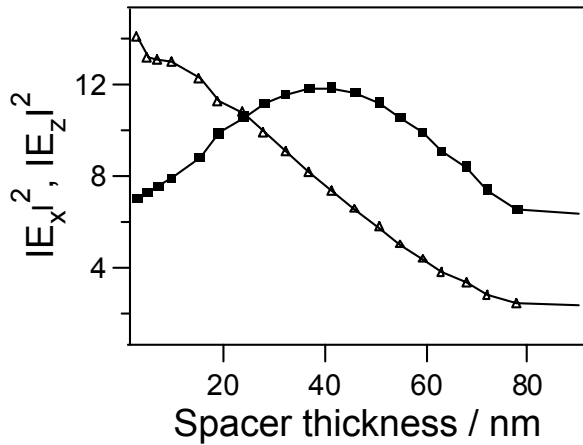


Figure 2.7. Calculated modulus squared of the exciting electromagnetic field perpendicular to the sample surface (z-axis, triangles) and parallel to it (x-axis, squares) for different spacer thickness, normalised to the electric field amplitude of the plane wave incident on the multilayered system. There is no electrical field along y. The incident light has transverse-magnetic polarisation and  $\theta_{ex}$  is adjusted for maximum electrical field.

is notable. At a very small separation distance (0-20 nm) the dipole parallel to the interface is cancelled by its mirror image. Then its contribution increases till roughly 40 nm. In comparison the perpendicular dipole has a very strong contribution to the overall picture close to the interface, which gradually decreases with the separation distance.

For a dipole located in air, infinitely close to the spacer-air interface, the total electromagnetic decay rate  $P_{rad,tot}$  is calculated according to the model of Chance, Prock and Silbey.<sup>14</sup>

$$P_{rad,tot} = P_{rad,0} \cdot \left( 1 + \frac{6\pi \cdot \epsilon_0 \cdot \epsilon_{air}^2}{\mu_0^2 \cdot k_{air}^3} \text{Im}(\mathbf{E}_{br} \cdot \boldsymbol{\mu}_{em}^*) \right) \quad 2.22.$$

With  $P_{rad,0}$  being the decay rate of a dye surrounded by air only,  $k_{air}$  the modulus of the

wavevector in air and  $\boldsymbol{\mu}_{em}$  its emission dipole moment. Note that the expression in brackets is independent of the magnitude of  $\boldsymbol{\mu}_{em}$ .

The back reacted field due to a dipole with some polar angle  $\alpha_{em}$  relative to the surface normal at the dipole position,  $\mathbf{E}_{br}$ , is obtained as a linear superposition of the fields  $\mathbf{E}_{br,para}$  and  $\mathbf{E}_{br,perp}$  that are generated by dipole parallel and perpendicular to the surface plane which are both parallel to the exciting dipole. The back reacted field is generated by the interaction of the free field with the glass and the metal. This back reacted field performs work on the dipole, which may enhance or suppress the emission.

$$\mathbf{E}_{br} = \begin{pmatrix} E_{br,para} \cdot \sin(\alpha_{em}) \\ 0 \\ E_{br,perp} \cdot \cos(\alpha_{em}) \end{pmatrix} \quad 2.23.$$

thus

$$\mathbf{E}_{br} \cdot \boldsymbol{\mu}_{em} = \begin{pmatrix} E_{br,para} \cdot \sin(\alpha_{em}) \\ 0 \\ E_{br,perp} \cdot \cos(\alpha_{em}) \end{pmatrix} \cdot \begin{pmatrix} \boldsymbol{\mu}_{em} \cdot \sin(\alpha_{em}) \\ 0 \\ \boldsymbol{\mu}_{em} \cdot \cos(\alpha_{em}) \end{pmatrix} = \boldsymbol{\mu}_{em,0} \cdot (E_{br,para} \cdot \sin(\alpha_{em})^2 + E_{br,perp} \cdot \cos(\alpha_{em})^2)$$

2.24.

, these fields are calculated according to <sup>15</sup>

$$E_{br,perp} = \frac{i\boldsymbol{\mu}_{em}}{4\pi\epsilon_0\epsilon_{air}} \int_0^\infty dk_{\rho,em} \frac{(k_{\rho,em})^3}{k_{air,z}} \cdot r_{TM}$$

$$E_{br,para} = \frac{i\boldsymbol{\mu}_{em}}{4\pi\epsilon_0\epsilon_{air}} \int_0^\infty dk_\rho \left[ -\frac{k_{\rho,em} \cdot k_{air,z} \cdot r_{TM}}{2} - \frac{k_{\rho,em} \cdot (k_{air,z})^2 \cdot r_{TE}}{2 \cdot k_{air,z}} \right] \quad 2.25.$$

With  $r_{TM}$  and  $r_{TE}$  being the amplitude of the reflected waves for the corresponding polarisations,  $k_{\rho,em}$  the projection of the wavevector in the sample plane and  $k_{air,z}$  the projection of the wavevector in air on the surface normal (z). These values hold for a dipole being displaced from the spacer-air interface by an infinitely small distance to the air side. They serve as a basis to obtain the values for an infinite displacement to the spacer side, which is the geometry relevant for our experiments (see Chapter 4). The values for chromophores inside the spacer are obtained by multiplying the result for the perpendicular dipole by a factor of  $(\epsilon_{spacer})^2$  and the result for the parallel dipole by a factor of  $1^{16}$ .

The rate of the emitted radiation to reach the detector is obtained by application of the reciprocity theorem<sup>17</sup>. This theorem makes use of the reversibility of the propagation of light. It allows for the calculation of the radiation emitted by an oscillating dipole in a certain direction via calculation of the local electrical field generated by a plane wave incident from this direction,

therefore reducing the problem to a calculation which is analogous to the determination of the excitation rate. For this calculation, the appropriate wavelength of light (emission wavelength of the chromophore) and the corresponding dielectric responses of the materials must be used.

Thus, the rate  $P_{\text{rad,det}}$  of emission in the detector covering the solid angle  $\Omega_d$  is obtained from the two electrical field components  $E_{\text{px}}$ ,  $E_{\text{pz}}$  produced by incident light with p-polarisation and  $E_{\text{sy}}$  produced by an incident electromagnetic wave in TE - polarization.

$$P_{\text{rad,det}} \propto \int d\Omega (\mathbf{E}_{\text{em}} \cdot \boldsymbol{\mu}_{\text{em}})^2 \approx P_{\text{em},0} \cdot n_1 \cdot \frac{3}{8\pi} \cdot \Omega_d \cdot (\mathbf{E}_{\text{em}} \cdot \boldsymbol{\mu}_{\text{em}})^2 \quad 2.26.$$

Separate evaluation of the contributions due to TM and TE polarised light for the analysis of polarised detection is straightforward.

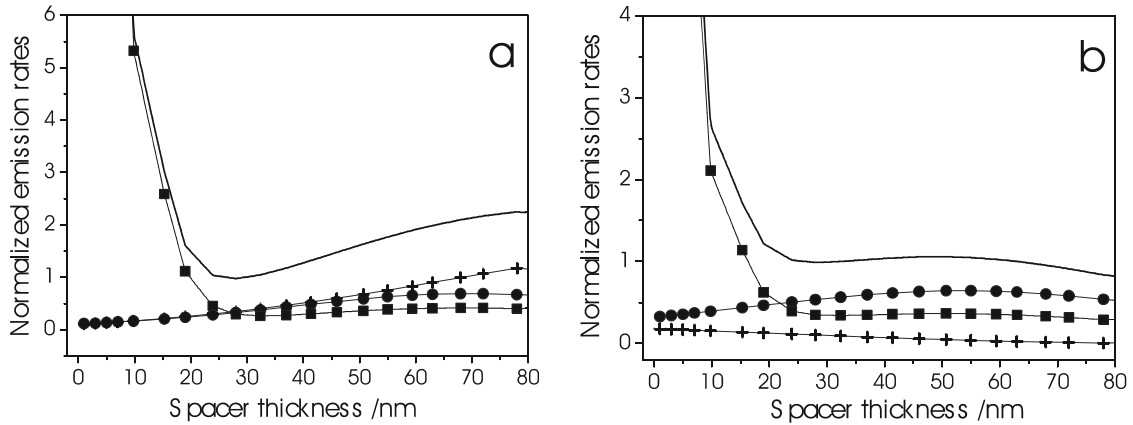


*Fig. 2.8. Normalized emission rates for a parallel dipole (a) and a perpendicular dipole (b). the total decay rate is indicated by the solid line, it is decomposed in contributions due to radiation to the glass side (circles), to the air side (crosses) and the remaining rate not leading to far field photons (squares).*

In Fig. 2.8, The electromagnetic decay rates of a chromophore in the system studied here are displayed as a function of spacer thickness. Three different contributions to the total rate, namely photon emission to the air side, photon emission to the prism side and electromagnetic decay without any emission of far-field photons can be distinguished. In the latter case, the energy is dissipated in the gold layer. For a spacer thickness below roughly 20 nm, this decay channel strongly dominates, leading to a steeply increasing total decay rate. For thicker spacer layers, the emission of far field photons contributes significantly, with emission through air becoming increasingly important for dipoles parallel to the interfaces while dipoles perpendicular to the interface mainly emit via the prism at the intermediate distances displayed here.

### 2.4. Colloidal systems

Since, in this work gold nanoparticles were subject of research, mentioning some basic principles of colloidal systems is justified. It is clear that the diversity of colloidal systems, their complexity and all forces interacting between surfaces can not be captured in just few pages. Here only a brief outline of colloidal systems will be given and the main considerations of stability of charged colloids will be described. A comprehensive description of colloidal systems can be found in literature.<sup>18, 19</sup>

#### 2.4.1. Definition, structure and size of the dispersed species

In homogeneous solutions, there exists a mixture of distinct species that are intermixed or dispersed as individual molecules. However, between pure bulk material and molecularly dispersed solutions lies a wide variety of important systems in which one phase is dispersed in a second, but in units which are much larger than molecular size or in which the molecular size of the dispersed material is significantly greater than that of the solvent or continuous phase. Such systems are generally defined as colloids, although there may be accepted limitations on the unit size of the dispersed phase, beyond which another terminology may be used. To define colloids more or less adequately one must consider two aspects of the system: structure – how the component of the system are put together or mixed – and size – what the dimensions are of the dispersed units in the system.

In general, a colloid is a system consisting of one substance (the dispersed phase: a solid, liquid or gas) finely divided and distributed evenly throughout a second substance (the dispersion medium or continuous phase: a solid, liquid or gas). Depending on the type of the dispersed phase diversity of colloidal systems are known: emulsions, dispersions, foams, gels, aerosols, micellar solutions, etc.

In terms of size of the dispersed units, the general definition refers to the dispersed phase to be “finely divided”. Colloidal properties are usually exhibited by systems in which the size of the dispersed phase falls in the range of 1-1000 nm, although those limits are far from rigid.

The common feature of all dispersed systems is the large interfacial area which exist between the continuous and dispersed phase. As a consequence, 1) dispersions are thermodynamically unstable, because the internal energy of the system is increased, 2) the properties and stability of colloids are determined by the properties of the interfaces.

2.4.2. Colloidal stability

Since in case of colloidal gold nanoparticles charged particles are concerned, here only the main forces responsible for the stability of such system will be addressed.

In the case of charged particle there is an ionic atmosphere created around the interface of the particle. This charged cloud is called electrical double layer (EDL). In a real colloidal system thermal motions of the ions in the solution and the steric requirements lead to a finite amount of space which could be occupied by the charges called Stern layer (fig. 2.9). The Stern layer is a small space separating the ionic atmosphere near an interface, the diffuse double layer, from the steric wall of the charged plane just adjacent to the interface. The thickness of the Stern layer, is usually on the order of a few nanometers and reflects the finite size of charged groups and ions specifically associated with the interface.

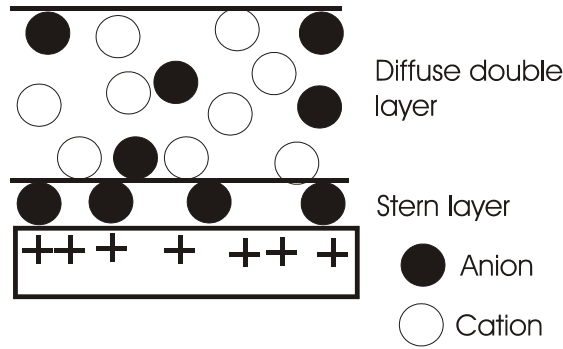


Figure 2.9. Schematic representation of the electrical double layer.

According to the Debye-Hückel approximation the electrical potential falls off exponentially with distance to the surface.

$$\psi = \psi_0 \exp(-\kappa z) \tag{2.27}$$

where  $\psi$  is the electrical potential,  $z$  is the valence and  $\kappa$  is the so called “Debye length”, which is reciprocal of the thickness of the EDL. The equation for the double layer thickness is

$$\frac{1}{\kappa} = \left( \frac{\epsilon_0 \epsilon K T}{\epsilon_i^2 \sum c_i z_i^2} \right)^{1/2} \tag{2.28}$$

Here  $\epsilon_0$  is the dielectric permeability in vacuum or in free space,  $\epsilon$  is the relative permeability of the medium,  $c_i$  is the concentration of electrolyte. One can see that the thickness of the EDL is inversely proportional to the concentration of electrolyte and the square of the valence of the ions involved. In terms of colloidal stability, this means that the distance between two particles that can be maintained under a given set of circumstances will depend upon, among other things,

those two factors. Their important effect gives one a handle for manipulating the characteristics and stability of many colloidal systems.

It is important to understand how the EDL provides stability to a colloidal system. If first the situation of two isolated, similarly charged particles with their associated EDLs is considered, it is relatively easy to understand the basic concepts of the electrostatic stabilization of colloids. In the context of (kinetic) stability, one can say that a system is stable so long as the individual particles maintain their identities – as long as flocculation and/or aggregation do not occur. In order for aggregation to occur, two particles must collide, and do so with sufficient force that the collision will be effective or “sticky”. Therefore two primary criteria must be considered in the discussion of colloidal stability: the number and frequency of particle collisions and the effectiveness of those collisions.

As depicted in fig. 2.10. when two charged particles approach, the two charge clouds or EDLs will begin to interact. Since the EDLs are of the same sign, their interaction will be repulsive, leading to an increase in the electrical potential between the particles. In simple terms, the EDL can be viewed as a spring between the two particles. As they approach, the spring is compressed and develops a force pushing the particles apart. The magnitude of the repelling will depend on the force constant of the spring (i.e. the magnitude of the EDL). The larger the constant, the greater the resistance to mutual approach and the more difficult a sticky collision

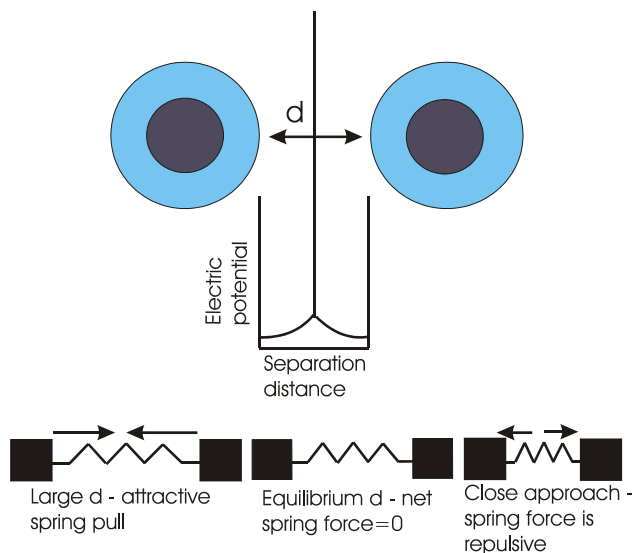


Figure 2.10. The interactions between two colloidal particles and its visualisation as two blocks connected by a spring.

leading to flocculation. The interaction of the respective electrical double layers, therefore, represents an energy barrier in the total interaction curve.

As the two particles approach, there will be two (at least) types of interaction: the repulsive interactions just described and the relentless van der Waals attractive interactions,

which make most colloids inherently unstable. The total interaction energy for the system under consideration will be the sum of the two energies:

$$\Delta G_{total} = -\Delta G_{att} + \Delta G_{rep} \quad 2.29.$$

A simple and relatively good approximation describing the repulsive interaction forces is derived by Reerink and Overbeek.

$$\Delta G_{rep} = \frac{Bek^2T^2a\gamma^2}{z^2} \exp(-\kappa H) \quad 2.30.$$

where H is the distance between spheres of radius  $a$ ,  $B$  is a constant equal to  $3.93 \times 10^{39} A^{-2} \gamma^{-2}$ ,  $z$  is the charge of the counterion,  $e$  is the electrical charge, and

$$\gamma = \frac{\exp(ze\psi_s / 2kT) - 1}{\exp(ze\psi_s / 2kT) + 1} \quad 2.31.$$

As pointed out earlier in this chapter the effective electrical potential of importance will be that of the Stern layer  $\psi_s$  rather than that at the surface,  $\psi_0$ .

If we now add the attractive interactions the total interactions will be:

$$\Delta G_{total} = \frac{Bek^2T^2a\gamma^2}{z^2} \exp(-\kappa H) - \frac{A_H}{12\pi H^2} \quad 2.32.$$

It should be clear that the key element in determining the height of the energy barrier imposed by the EDL is the concentration and valence of the electrolyte in the system. An increase in the electrolyte concentration reduces the repulsive electrostatic interactions, reducing the energy barrier and facilitating effective particle collisions – the system is less stable.

## References:

- <sup>1</sup> See for example: *Optics*, Möller, K. D. **1988**
- <sup>2</sup> Knoll, W. *Annu. Rev. Phys. Chem.* **1998**, 49, 569
- <sup>3</sup> Knoll, W. *MRS BULL* **1991** 16, 29-39
- <sup>4</sup> Kretschmann, E. *Opt. Commun.* **1972**, 6, 185
- <sup>5</sup> Pochi Yeh, *Optical waves in layered media*, Wiley-VCH, New York, **1999**.
- <sup>6</sup> M. Born, *Principles of optics*. Pergamon Press, Oxford, **1984**
- <sup>7</sup> Mie, G. *Annal. Phys.* **1908**, 5, 377.
- <sup>8</sup> U. Kreibig, , M. Vollmer, ,*Optical properties of metal clusters*; Springer, Berlin **1995**.
- <sup>9</sup> J. R. Lakowicz, *Principles of fluorescence spectroscopy*, Plenum Press, New York, **1986**.
- <sup>10</sup> Jablonski, A., *Z. phys.* **1935**, 94, 38-46.



- <sup>11</sup> Barnes, W. L. *J. of Modern Optics* **1988**, 45, 661-699.
- <sup>12</sup> Lakowicz, J. R. *Analytical Biochemistry* **2001** 298, 1.
- <sup>13</sup> Förster, Th., *Ann. Phys* **1948**, 2, 55-57
- <sup>14</sup> Chance, R. R. Prock, A., Silbey, S. *Adv. Chem. Phys.* **1978**, 37, 1-65.
- <sup>15</sup> L. Novotny, Ph.D. thesis, ETH Zürich, **1996**.
- <sup>16</sup> Khoshravi H., Loudon, R. *Proc. R. Soc. Lond. A* **1991**, 433, 337.
- <sup>17</sup> Mendez, E. R., Greffet, J. J., Carminati, R. *Opt. Commun.* **1997**, 142, 7.
- <sup>18</sup> Mayers, D. *Surfaces, interfaces and colloids*, Wiley-VCH, New York, 1999.
- <sup>19</sup> Israelachvili, J. N. *Intermolecular and surface forces*, Academic Press, London, 1992

### 3. Sample preparation and measurement techniques

In this chapter the major sample preparation and measurement techniques that were used for this work will be briefly outlined. The corresponding working recipes will be described in details and results from the sample characterisation will be presented

#### 3.1. Self-assembled monolayers

Self-assembled monolayers (SAM) are molecular assemblies that are formed spontaneously by the immersion of an appropriate substrate into a solution of an active surfactant (see for more details<sup>1</sup>). There are several types of self-assembly methods that yield organic monolayers. This include organosilicon on hydroxylated surfaces ( $\text{SiO}_2$  on Si,  $\text{Al}_2\text{O}_3$  on Al, glass, etc.); alkanethiols on gold, silver and copper; dialkyl sulfides on gold; dialkyl disulfides on gold; alcohols and amines on platinum; carboxylic acids on aluminium oxide and silver.

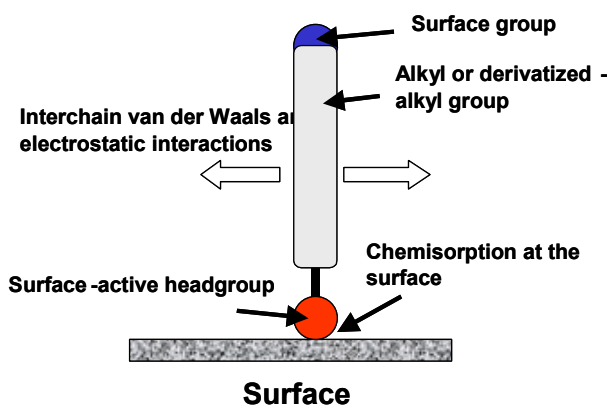


Figure 3.1. A surfactant molecule.

From energetic point of view, a self-assembling surfactant molecule can be divided into three parts (fig. 3.1). The first part is the head group that provide the most exothermic process, i.e., chemisorption on the substrate surface. The very strong molecular-substrate interactions result in an apparent pinning of the head group to a specific site on the surface through a chemical bond. This can be a covalent Si-O bond in the case of silanes on hydroxylated surfaces, a covalent Au-S bond in the case of alkanethiols on gold; or an ionic  $-\text{CO}_2^-\text{Ag}^+$  bond in the case of carboxylic acids on AgO/Ag. As a result of the exothermic head group-surface interactions, molecules try to occupy every available binding site on the surface, and in this process they push together molecules that have been already adsorbed.

The second molecular part is the alkyl chain. Van der Waals interactions are dominant along a simple alkyl chain. Only after the molecule is chemisorbed the formation of a closely packed monolayer can start.

The third molecular part is the terminal functionality which can be just a methyl group or whatever functional group (amino, carboxylic, etc.).

In this work two types of self-assembly methods were used - 3-Aminopropyltriethoxysilane (3-APTES) on silicon oxide and 3-Mercaptopropionic acid (MPA) on gold.

MPA was self-assembled on a freshly prepared gold surface as the substrate was immersed in a 0.03 M Milli-Q water solution of the thiol for one hour. Then the substrate was carefully washed with water in order to remove all unbound thiol. Thus prepared surface carries carboxylic groups. In water the carboxylic groups are dissociated and the surface is negatively charged.

3-APTES was self-assembled on silicon wafer and glass. The wafers were first carefully cleaned with surfactants and water. Then the surface were activated in a mixture of  $\text{H}_2\text{O}_2 : \text{NH}_3 : \text{H}_2\text{O}$  (1 : 1 : 5) for 30 minutes at 80 °C. Two means of self assembly were used. 1) The substrates were immersed for 1 hour in a 0.1 M Milli-Q water solution of 3-APTES. Then washed with water, dried with nitrogen and put in an oven for one hour at 120 °C.<sup>2</sup> The layer of 3-APTES self-assembled this way is rather rough with a domain structure (proved by AFM). 2) The second approach was the deposition of the silane from the vapour phase. The wafers were carefully dried and then placed in a sealed container in the presence of 3-APTES. Then the container was put in an oven at 130 °C for 3 hours. After cooling the wafers were washed first with ethanol and then with water for the removal of all not chemically bound silane. This way of preparation provides a smooth monolayer of 3-APTES on the surface. Such samples were used as a substrate for the layer-by-layer deposition of PSS/PAH for small angle X-ray reflectivity. Silanes in general provide a three dimensional network. Each silane molecule is bound with one Si-O bond to the surface and other two Si-O bonds to two neighbouring silane molecules. 3-APTES provides a surface with  $\text{NH}_2$  functional groups which in water are dissociated and the surface is positively charged.

#### **3.2. Layer-by-layer deposition**

The so called layer-by-layer deposition technique falls into the category of template assisted assembly. Template assisted assembly is much faster than self-assembly/chemical modification cycles whose outcome is often uncertain and difficult to predict. For the layer-by-layer assembly, it can be tailored to even allow multimaterial assembly of several compounds without specific chemical modification, thus giving access to multilayer films with complex properties and functionalities.

Layer-by-layer deposition is an environmentally friendly (it is conducted in aqueous medium), simple and ultra-low-cost technique. The materials can be small organic molecules or

organic compounds, macromolecules, biomolecules, colloids, nanoparticles with various shapes and from diversity of materials. The technique can be applied to solvent accessible surfaces of almost any kind and any shape.

A comprehensive summary of layer-by-layer deposition technique and its diversity of applications is the excellent book of the father of layer-by-layer deposition technique Gero Decher.<sup>3</sup>

In the following the layer-by-layer deposition of polymers and gold nanoparticles with the corresponding conditions of assembly will be described.

#### 3.2.1. Layer-by-layer deposition of polyelectrolytes.

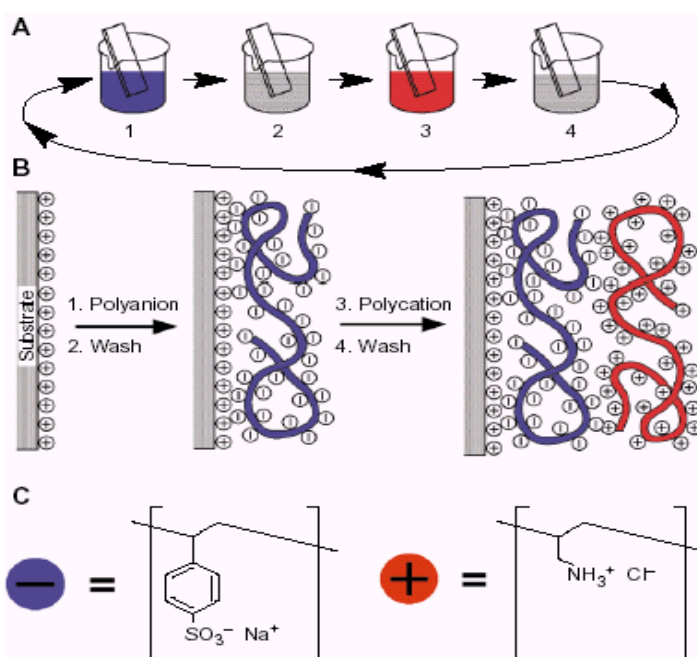


Figure 3.2. Schematic representation of Layer-by-Layer deposition process.

(picture from G. Decher., *SCIENCE* 1997, 277, 29)

Layer-by-layer deposition is a simple process based on the attractions of opposite charges. So in order to build a multilayered system one needs only two oppositely charged polyelectrolytes. The process of multiplayer build-up is depicted in fig 3.2. It works as follows: If the substrate positively functionalised for example first it is immersed in a solution of negatively charged polyelectrolytes for certain time. Then it is washed with water. The charge on the surface is inverted and it is immersed in a solution of the other polyelectrolyte (the positively charged one). Then it is washed with water again. The charge on the surface is inverted again. Repeating these steps in a cyclic fashion it is possible to build as many layers as needed.

In the work presented here polyallylamine hydrochloride (PAH), molecular weight of 70 000 bought from Aldrich was used as a positively charged polyelectrolyte. Polystyrenesulfonate

sodium salt (PSS), molecular weight of 70 000 bought from Aldrich was used as a negatively charged polyelectrolyte. The assembly process was carried out at the following conditions: Both polyelectrolytes were adsorbed from aqueous solutions containing 0,02 monomol/l polymer (monomol refers to the molar concentration of monomer). 0,001 mol HCl was added to both polymer solutions. Salts were also added to the solutions,  $MnCl_2$  for PSS and NaBr for PAH, 0.5 and 2 M concentrations, respectively. The substrate was immersed sequentially into both solutions for 20 minutes at room temperature, washed with Milli-Q water after each step and dried. The deposition was started with PAH or PSS depending on the initial charge of the substrate surface (positive when the surface is modified by 3-APTES and negative on a 3-MPA modified gold surface).

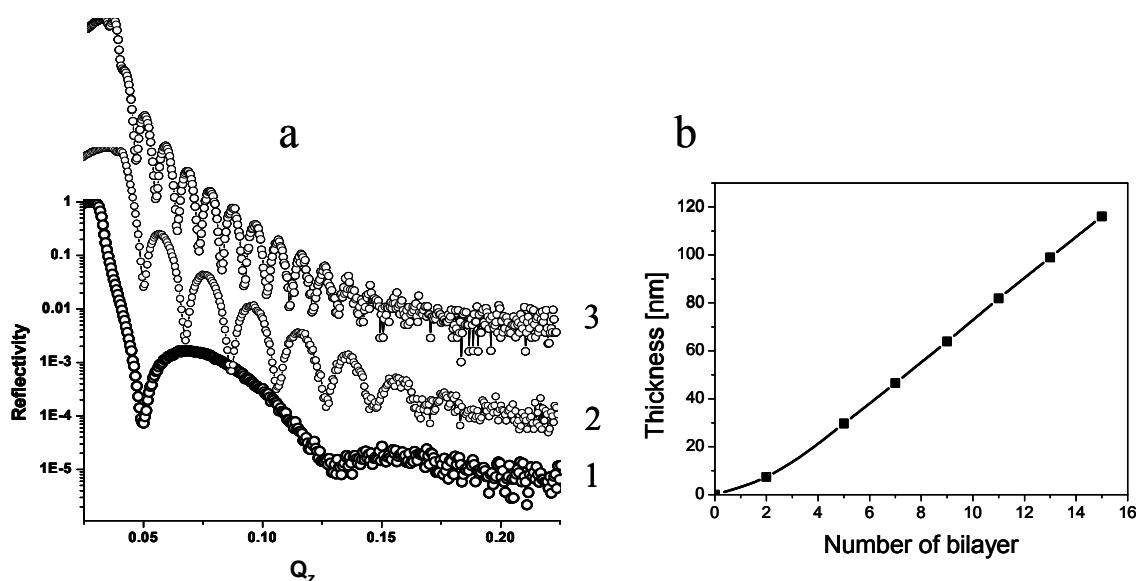
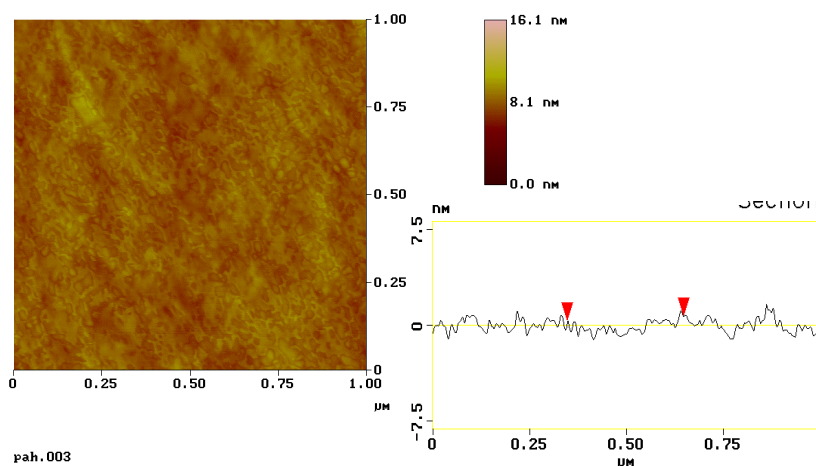


Figure 3.3. a) Small angle X-ray reflectivity spectra of samples composed of 1 – 2 bilayer, 2 – 5 bilayer and 3 – 7 bilayer. The thicknesses obtained are 7.4 nm, 29.7 nm and 46.5 nm respectively. b) growth of the thickness is plotted as a function of the number of bilayer.

Small angle X-ray reflectivity was measured in order to obtain information about the thickness of the obtained polyelectrolytes multilayer systems. Fig. 3.3.a shows the X-ray reflectivity spectra of 2, 5 and 7 bilayer PSS/PAH deposited on a silicon wafer premodified by a self assembled monolayer of 3-APTES. The thickness of the silane layer was measured by ellipsometry to be 1 nm. The plot in fig. 3.3.b represents the thickness as a function of the number of bilayer. The dependence is linear after the deposition of the second bilayer. The thickness of one bilayer is 9 nm while the first two bilayers are a little thinner.

The surface of the polymer layers obtained by this recipe is very smooth. The average roughness on the surface of the layers obtained from the X-ray reflectivity spectra was below 1 nm. More interesting for the current research was the surface peak to peak roughness. This information was obtained by AFM. Fig. 3.4. shows an AFM image of the surface of a PAH/PSS multilayer system composed of 6 bilayer which was deposited on template stripped gold (TSG). It clearly seen that the maximum height (peak to peak) of the roughness on the surface is about 2 nm.



*Figure 3.4. AFM image representing the surface of a sample containing 6 bilayer.*

Multilayer system build in the way described above can be terminated by either PAH or PSS and consequently can carry positive or negative charges. In the research presented in this book fluorescing dyes 1,1',3,3',3,3'- hexamethylindodicarbocyanine iodide (DiIC<sub>1</sub>(5)) possessing positive charges in water were deposited on a negatively charged surface of PSS. Gold nanoparticles carrying negative charges on the surface were deposited on positively charged surfaces of PAH or 3APTES. More details will be given in the next sections. (Section 4 regarding the deposition of DiIC<sub>1</sub>(5) and Sections 5 regarding deposition of gold nanoparticles).

### 3.3. Template stripping of gold from Mica

Template stripping of gold from Mica is a method for the preparation of ultrasmooth gold surfaces described for the first time by Wagner in 1995.<sup>4</sup> It is based on making profit of the atomically smooth Mica surface.

The process of preparation template stripped gold consists of a sequence of steps depicted in fig. 3.5. First, a mica sheet is cleaved. The fresh mica surface is atomically smooth and clean. Then it is put into an oven at 650 °C for one minute. This process serves for the removal of moisture from the surface, which could cause defects in the gold film. As a next step a thin gold

layer is thermally evaporated on the fresh mica surface. This mica/gold compound is then glued with the gold side to a clean glass slide. The glue (Epotek 377) has the same refractive index as the glass. As a final step this Mica/Gold/Glass composite is immersed in THF for about 10 minutes. This solvent reduces the adhesion between mica and gold without affecting the glue. Then the mica sheet is separated. The surface of a gold layer prepared in this fashion is very smooth as can be seen in fig. 3.5. The AFM measurement revealed that the maximum height (peak to peak) roughness on the surface is below 0.5 nm.

Template stripping of gold can be also prepared from silicon wafer. The roughness (peak to peak) is about 1.3 nm but the process is simplified. The silicon wafer is just mechanically separated from the gold film glued on glass slide without using any solvents.

The importance of TSG for the study on fluorescence intensity near gold layer will be presented in section 4. Moreover TSG turned out to be very useful in studies on lipid bilayers.<sup>5</sup>

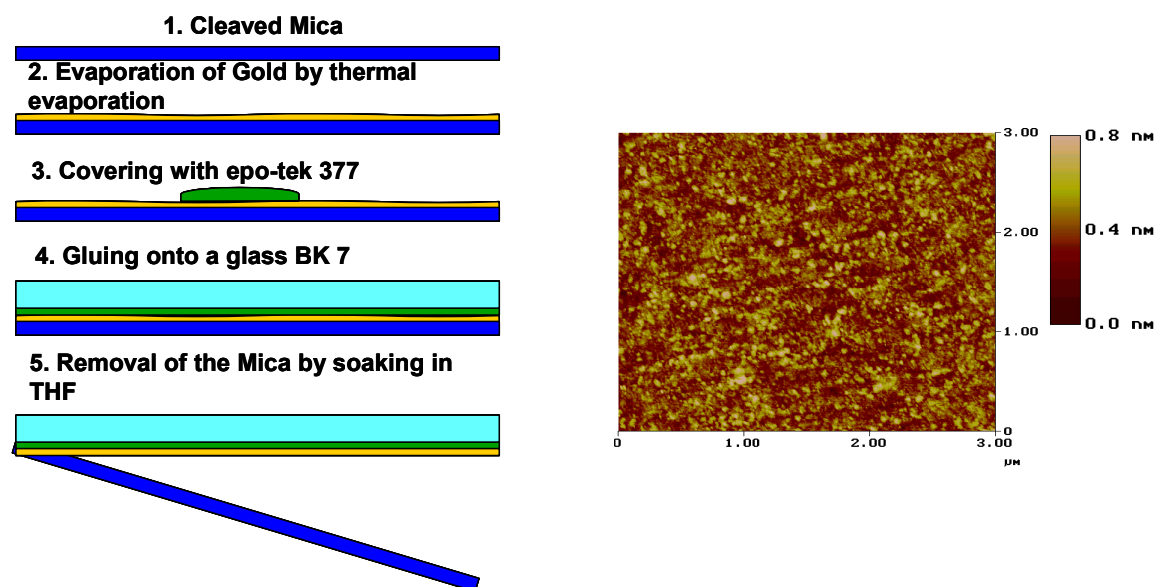


Figure 3.5. Left – The process of template stripping gold from mica depicted step by step. The AFM image on the right shows the surface of the gold layer prepared in such fashion .

#### 3.4. Preparation of colloidal gold nanoparticles.

Among the numerous methods for the production of gold nanoparticles by chemical routes is the citrate reduction method.

Citrate reduction of gold chloride in water is a well-documented method for colloidal gold nanoparticles preparation, which produces nano-sized gold particles with a narrow size distribution.<sup>6, 7</sup> These particles are well-dispersed in water by obtaining negatively charged surfaces from adsorbed ionic species from the reaction mixture. However, due to the complexity

of the adsorbed surface layer and its liability to medium changes, it is difficult to draw a clear picture of the detailed surface structure of individual particles.

The synthetic procedure is as follows: in a 500 ml 2-neck round bottom flask, 300 ml of a 0.01 % solution of  $\text{HAuCl}_4$  are brought to boiling under refluxing and stirring, then 10.5 ml of 1% trisodium citrate in water is injected quickly. After the color transition in the first 3 to 5 minutes, the mixture is kept boiling for another 20 minutes. The heating source is removed, and stirring is kept until the solution cooled down to room temperature. The colloidal suspension prepared this way had a conductivity of  $380 \pm 20 \mu\text{S}/\text{cm}$ , an initial pH of  $6.0 \pm 0.3$ , and a mean particle size of  $19 \pm 2 \text{ nm}$  as determined by scanning electron microscopy (SEM).

A characteristic of all gold colloids is the color which can vary between light red via purple-red to bluish-red. This effect is caused by a plasmon resonance, quantitatively described by the Mie theory, as already mentioned in chapter 2.1.1. The wavelength of plasmon resonance, in the case of gold usually in the region of 500-600 nm, depends on the size of the particle and on the shape and the dielectric properties of the surrounding medium. A spectrum of a colloidal solution of gold nanoparticles with size of about 15 nm is shown in fig. 3.6.

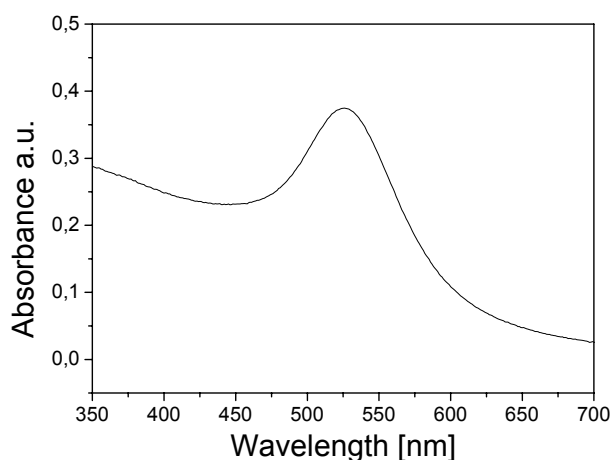


*Figure 3.6. Absorption spectrum with the characteristic plasmon resonance of a colloidal solution of gold nanoparticles.*

#### 3.5. Other sample preparation techniques

Thermal evaporation of metals and spin coating were also used in sample preparation. Substrates of glass and silicon wafer were cleaned by ultrasonication. For purification dialysis and a method of dissolution and selective precipitation of polymers were used.



### 3.6. Surface plasmon fluorescence spectroscopy (SPFS)

In this section the set up for surface plasmon fluorescence measurements will be described since it was the most commonly used analytical technique used in the research described in this thesis.

Fig. 3.7. shows the basic components of SPFS set up. In the common case a laser beam is directed to the sample. Before reaching the sample the beam is guided through a number of

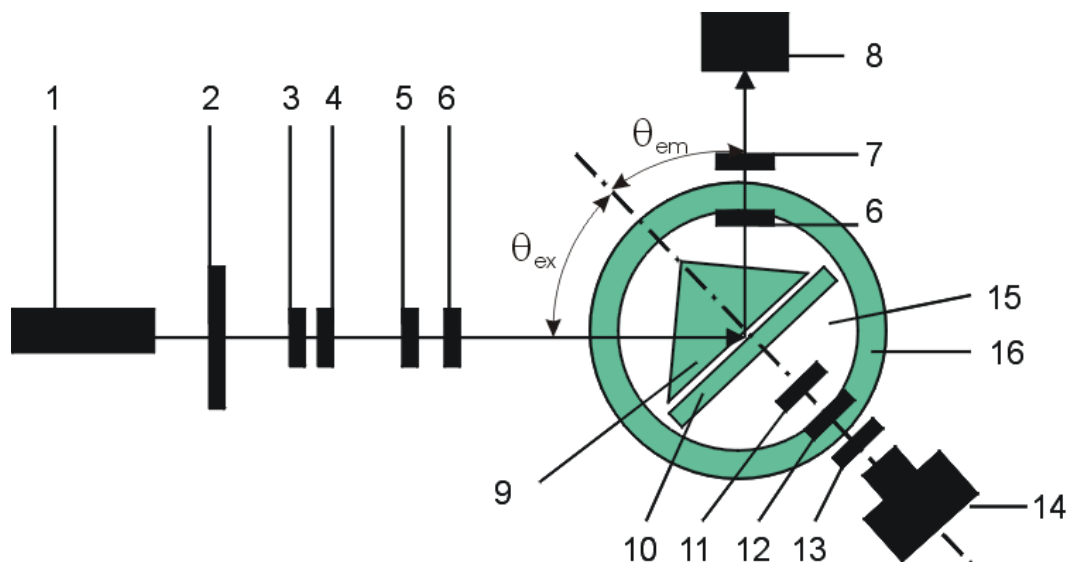


Figure 3.7. Surface Plasmon Fluorescence measurement set-up: 1 – HeNe laser (633 nm), 2 – chopper, 3 – polarizer for control of the intensity of the laser beam, 4 – polarizer for control of the polarization of the excitation light, 5 – line filter 633 nm, 6 – aperture for alignment of the incoming and reflected beam, 7 – lens, 8 silicon photodiode, 9 – prism, 10- sample, 11 – polarizer for control of the polarization of the collected light, 12 – notch filter (633 nm), 13 - line filter (670 nm), 14 – photomultiplier tube, 15 – goniometer for rotation of the sample, 16 – goniometer for rotation of the photodiode

optical elements. A chopper (2) is used to set the reference frequency thus the frequency of the periodically modulated laser light can be separated from all other frequencies. Then the beam passes through two polarizers. It has been mentioned earlier that only p-polarized light can excite surface plasmon resonance. Polarizer (4) is used to select the polarisation and by (3) the excitation intensity is regulated. The line filter (5) is used to select only the desired wavelength. The apertures 6 serve for facilitating the alignment of the excitation and reflected light.

The sample is attached to a sample holder, which is mounted to a rotation stage consisting of two goniometers. Goniometer (15) serves for the rotation of the sample holder thus

setting the angle of incidence ( $\theta_{\text{ex}}$ ). The second goniometer serves for the movement of the detector (8) at an angle  $\theta_{\text{em}}$ . In the general case detector (8) (a silicon photodiode) is used for collection of the reflected laser light at an angle of  $2\theta_{\text{ex}}$ .

In case of performing fluorescence measurements the emitted fluorescence is collected by a photomultiplier tube (14). Filters for cutting the laser light (12) and another one for selecting the emission wavelength (13) are used. A polariser (11) can be also mounted for selecting the polarisation of the light reaching the PMT.

Modifications of the instrument were done for conducting several kinds of experiments, which will be described in section 4 and 6.

#### **3.7. Other measurement techniques**

A number of other analytical tools were used in order to make this research possible. These are Scanning Electron Microscopy (SEM), Atomic Force Microscopy (AFM), Fourier Transform Infrared Spectroscopy (FTIR), Small Angle X-ray Reflectivity, Transmission Electron Microscopy (TEM), UV-visible spectroscopy (UV-vis), Contact Angle, Raman Spectroscopy, Scanning Tunnelling Microscopy (STM), Dynamic Light Scattering, Fluorescence Spectroscopy, Confocal Microscopy. Details about these analytical techniques will not be given here since they are well known and well described in the literature.

#### **References**

- 
- <sup>1</sup> A. Ulman, *Ultrathin organic films*, Academic Press, Inc., San Diego, CA, **1991**.
  - <sup>2</sup> Wang, J., Zhu, T., Song, J.Q., Liu, Z.F. *Thin Solid Films* **1998**, 327, 591.
  - <sup>3</sup> G. Decher, J. B. Schlenoff, *Multilayer thin films*, Wiley-VCH Verlag GmbH & Co. KgaA, Weinheim, **2003**.
  - <sup>4</sup> Wagner, P., Hegner, M., Guntherodt, H-J., Semenza, G. *Langmuir* **1995**, 11, 3867-3875
  - <sup>5</sup> Naumann, R., Schiller, S. M., Giess, F., Grohe, B., Hartman, K. B., Karcher, I., Koper, I., Lubben J, Vasilev, K., Knoll, W. *Langmuir* **2003**, 19, 5435-5443.
  - <sup>6</sup> Turkevich, T., Stevenson, P. S., Hiler, J. *Faraday Soc.* **1951**, 11, 55.
  - <sup>7</sup> Frens, G. *Nature Phys. Sci.* **1973**, 241, 20.

### 4. Fluorescence at a plane metal dielectric interface

A nearby metallic surface significantly influences the absorption and emission properties of a fluorophore placed in its vicinity. These effects must be always taken into account if fluorescence-related methods are applied to study objects close to a metal surface. Firstly, the excitation rate is altered via changes in the local strength of the electrical field. This field enhancement may vary over several orders of magnitude upon changing the experimental geometry due to surface plasmon excitation.<sup>1</sup> Secondly, the metal introduces both additional electromagnetic decay channels, dissipating energy in the metal and alters the free-space radiation rate in a nontrivial way. Thirdly, if the metal layer is thin enough (thickness in the order of 50 nm), the radiation emitted through the metal is polarised and concentrated into a narrow angular range due to intermediate excitation of a surface plasmon.<sup>2, 3, 4, 5</sup>

Some of the effects that influence molecular fluorescence close to a metal surface has led to the development of new experimental techniques and therefore found its way to applications. One example is the utilisation of the localised and highly amplified surface plasmon field for sensing<sup>6</sup> where a sensitive detection of the adsorption of fluorescence labeled biomolecules to a gold interface was demonstrated. Even single molecule detection in the vicinity of a metal surface has been found<sup>7</sup>, although quantitative interpretation has led to some discrepancies to the theoretical predictions<sup>8</sup>. As a consequence, a complete understanding of the relevant processes is expected to contribute to the further development of optimised experimental strategies.

In this study, the chromophore DiIC<sub>1</sub>(5) was used, a dye often employed in fluorescence microscopy while most earlier studies utilized phosphorescent europium complexes. This chromophore has a much lower oscillator strength than typical organic dyes and does not possess transition dipole moments with defined directions which is of great importance for the excitation and emission characteristics of organic dyes as was demonstrated by single-molecule experiments on a purely dielectric interface.<sup>9, 10, 11</sup>

The scope of this work is to present a careful comparison of measured data with the classical theory, taking into account the physical properties of the chromophore that must be known for a quantitative evaluation of experimental results.

In the following the fluorescence intensity, the angular distribution of the emission and the photobleaching rates were measured and compared with the theory. In addition the problem was addressed on a single molecule level.

### 4.1. Experimental and theoretical evaluation of the fluorescence intensity emitted from an ensemble of fluorescing dyes

A considerable number of experimental investigations on the influence of a nearby metal layer on fluorescence emission were carried out, though, most quantitative studies concentrated on the changes in excited state lifetime because this quantity, being only influenced by changes in the emission process, requires less modelling in order to be compared to theory but gives less detailed information about the emission channels.

Following the pioneering experiments of Drexhage<sup>12, 13, 14</sup>, excited state lifetimes at very small distances from the metal were investigated as well as the additional effects that come into play when the thickness of the metal layer is finite<sup>15</sup>. Careful investigations on the influence of the direction of excitation and detection have been performed on a dielectric-air interface.<sup>16</sup>

Intensity measurements were used to access the enhanced excitation efficiency when surface plasmons are excited on a thin metal film in the Kretschmann-configuration. There, it was qualitatively discussed that the enhanced fluorescence emission upon excitation of the surface plasmon resonance is due to the enhanced electric field strength. To our knowledge no full quantitative analysis of measured intensities from an ensemble of molecules was published upon variation of the distance from a metal surface as well as the directions of excitation and emission.

#### 4.1.1. Materials and methods

For the experiments it is crucial to obtain multilayered samples where the roughness of the relevant interfaces (metal/spacer) and (spacer/air) is small compared to the lengthscales to be studied experimentally which are in the order of 10 - 80 nm. An ultrasmooth gold surface was prepared by the method of template stripping: Gold is evaporated on freshly cleaved mica (ASTM V-2, S&J Trading) then the coated side is glued (Epotec 377, Polytec) on a glass slide (BK7, Menzel). Subsequent removal of the mica after 1h immersion in THF (Riedel-deHaen, 99,9%) leaves a gold surface with a roughness below 1 nm peak to peak as verified by atomic force microscopy (AFM). Details are given in Chapter 3.3.

The spacer layer is built up by alternating deposition of polyelectrolyte layers of opposite charge. The model sample is depicted in fig. 4.1

#### 4. Fluorescence at a plane metal dielectric interface

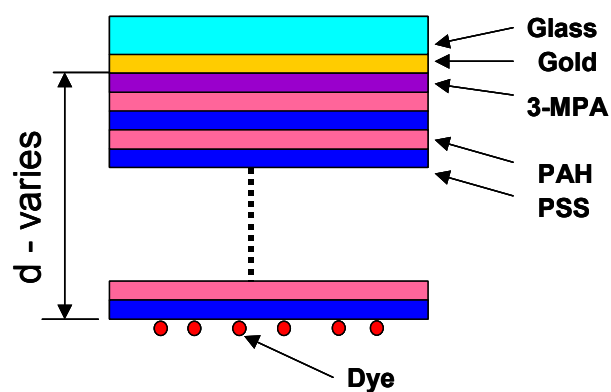


Figure 4.1. The experimental approach. Multilayer system of poly-electrolytes is build of TSG functionalised by a SAM of 3-MPA. The fluorescing dye is electrostatically deposited on a negatively charged layer of PSS. The distance between the fluorescing dye and the gold interface can be altered by the number of PAH/PSS layers.

First, the freshly stripped gold surface is functionalized by 3-mercaptopropionic acid (Aldrich), providing negative charge on the surface due to deprotonated carboxylic groups. Alternating immersion of the sample in an aqueous solution of Poly(allylamine) (PAA, Aldrich, Mw=100000) and Poly(styrenesulfonate) (PSS, Aldrich, Mw=70000), finishing with PSS, leads to a negatively charged surface. As described in Chapter 3.2., Manganese Chloride (Merck, 99%) and Sodium Bromide (Aldrich, 99+%) were added to the solutions of PSS and PAH respectively in order to adjust the ionic strength. In a last step, the sample was immersed in an aqueous solution with a concentration of  $10^{-5}$  Mol/l of the Chromophore (1,1',3,3,3',3'-hexamethylindico-cyanine iodide DiIC<sub>1</sub>(5)), Molecular Probes, maximum excitation at  $\lambda_{ex}=638$ nm, maximum emission at  $\lambda_{em} = 670$  nm. The structural formula of the dye and its absorption and emission spectra are shown in fig. 4.2. The roughness of the resulting surface was again investigated by AFM and found to be below 3 nm peak-to-peak.

**H-14700**  
**(1,1',3,3,3',3'-hexamethylindico-cyanine iodide (DiIC<sub>1</sub>(5)))**

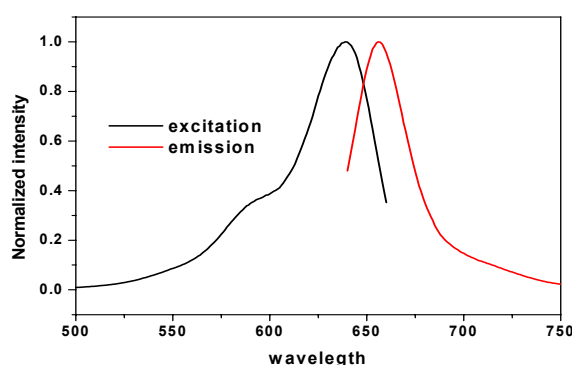
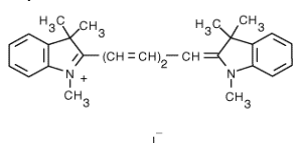


Figure 4.2. The chemical structure with the excitation and emission spectra of the chromophore.

Independent thickness information was obtained by small angle X-ray reflectivity (using copper K<sub>α</sub> radiation). Reference samples for X-ray reflectivity measurements were prepared by

functionalizing a Silicon waver (CrysTec) with 3-Aminopropyltriethoxy-silane (Sigma, 98%) following the procedure described in Chapter 3.1. and proceeding as with the gold surface.

Optical characterisation of the sample was carried out in a setup as depicted schematically in Fig. 4.3. The sample is attached to the base of a glass prism optically matched by index oil. A beam of a HeNe Laser (632.8 nm) with transverse-magnetic polarization is directed through the prism. By rotating the prism, the angle  $\theta_{\text{ex}}$  of the incident beam relative to the surface normal of the sample and consequently the in-plane wavevector  $\mathbf{k}_{\text{p,ex}}$  is adjusted. Collection of the reflected light with a photodiode mounted on a second, collinear goniometer, allows angle-resolved reflectivity measurements, details about this experimental scheme ("surface plasmon spectroscopy") can be found in Chapter 3.6., it essentially allows for the determination of the thickness and dielectric constant of the gold layer and, given its dielectric constant, the thickness of the spacer layer. For fluorescence measurements, the photodiode is replaced by a photomultiplier tube (PMT, Hamamatsu, H 6240 SERIES) operated in photon counting mode. Stray light of the laser is blocked from the PMT by a notch filter (Holographic Notch-Plus<sup>TM</sup> Filter, 638.2 nm, Kaiser) and a line filter (670 nm, LOT).

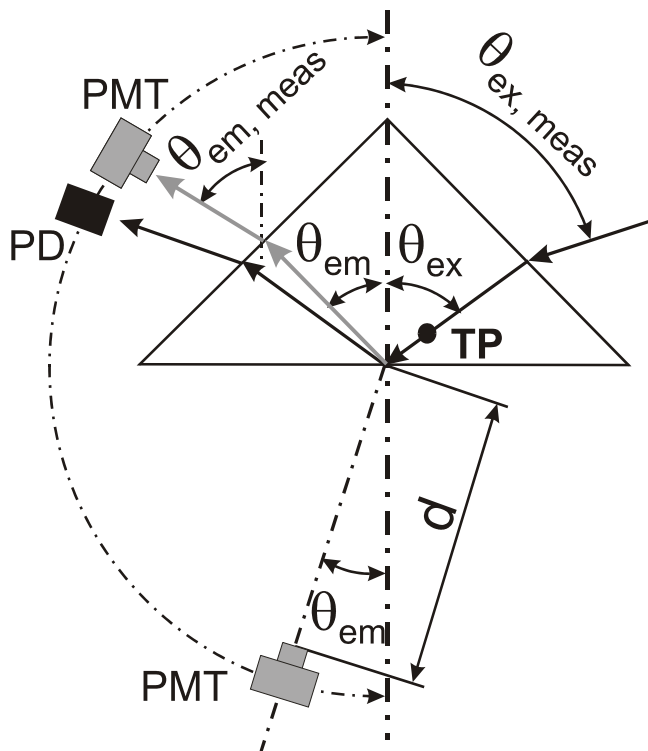


Fig. 4.3: Sketch of the experimental geometry. TP indicates the turning point of the prism,  $d$  is the distance of the photomultiplier tube (PMT) from the spot where fluorescence is excited. PD denotes the silicon photodiode.

Additionally, a polariser was mounted in front of the PMT for polarisation-sensitive detection. The experimentally determined directions of exciting and emitted light,  $\theta_{\text{ex, meas}}$  and

$\theta_{em, meas}$  are transformed to the angles describing the light propagation inside the prism,  $\theta_{ex}$  and  $\theta_{em}$ , by applying Snellius' law.

By moving the PMT a full half circle around the prism, both the emission through air and through glass are recorded in one experimental step.

In order to be able to compare light intensities emitted through the prism and through air, it must be taken into account that the effective solid angle  $\Omega_d$  covered by the PMT can be calculated simply as  $\Omega_d = A_{PMT}/4\pi d^2$  for emission through air with  $A_{PMT}$  being the active area of the PMT and  $d$  being the distance of the PMT from the goniometer axis. For the detection of the intensity emitted through the prism refraction at the interface leads to an effective reduction of covered solid angle

$$\Omega_{d,Pris} = \frac{A_{PMT}}{4\pi d^2} \cdot \frac{\cos(\theta_{int})}{n_{pris} \sqrt{1 - \frac{\sin(\theta_{int})^2}{(n_{pris})^2}}} \cdot \frac{1}{n_{pris}} \quad 4.1.$$

Additionally, reflection losses at the interface are taken into account as well as a minute correction term due to the turning point of the prism being slightly displaced from the middle of the prism base.

In order to determine the apparent angle between absorption and emission dipole moment,  $\beta_{em,ex}$ , an aqueous solution of PSS and DiIC<sub>1</sub>(5) was spin-coated on a glass slide, yielding a thick (ca. 1  $\mu$ m) film with randomly distributed chromophores. Schematically the measurements are shown in fig. 4.4. Fluorescence was excited by placing the glass slide in a linearly polarised laser beam with the glass slide being oriented perpendicular to the beam. Fluorescence emitted normally through the slides' back side was recorded for the linear polarisations parallel and perpendicular to the exciting beam. From the two measured intensities,  $\beta_{em,ex}$  could be determined as described in Chapter 2.2.3.

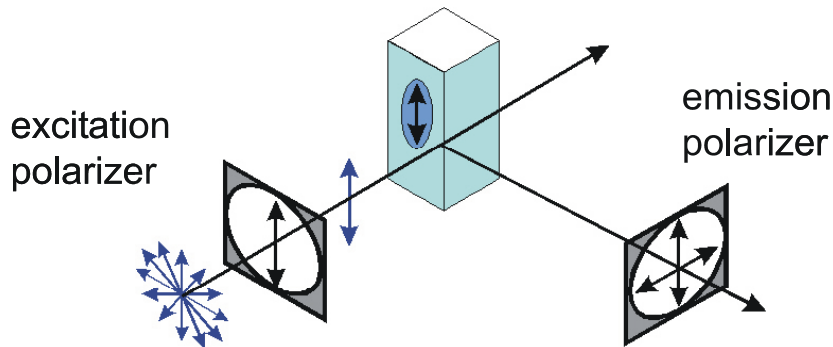


*Figure 4.4. Scheme of the experimental assessment of the displacement between absorption and emission dipole moment of the dye.*

### 4.1.2. Theoretical modelling

The calculation of the excitation probability, the total emission probability and the probability the light to reach the detector in case of a chromophore near a metal interface, together with the geometry in consideration are presented in Chapter 2.3.

In order to calculate the fluorescence intensity originating from an ensemble of molecules, averaging over all possible orientation of absorption and emission dipole moments is performed, assuming that absorption and emission dipole moments have a relative angle  $\beta_{em,ex}$ . Given a fixed orientation of the emission dipole  $\alpha_{em}$ ,  $\psi_{em}$ , for a given  $\beta_{em,ex}$  the average of the excitation dipole will contribute  $\cos(\beta_{em,ex})$  in the direction parallel to the emission dipole and  $2^{1/2}\sin(\beta_{em,ex})$  along each of the two Cartesian coordinates perpendicular to  $\mu_{em}$  where one of the latter two coordinates is chosen to be perpendicular to the plane of incidence and therefore not contributing upon illumination with TM polarised light. As a consequence, the measured intensity can be calculated as

$$I_{measured} \propto \int d\Omega_{\mu,em} \left[ \cos(\beta_{em,ex}) \cdot I_{sm}(\langle \mathbf{\mu}_{ex} \rangle = \langle \mathbf{\mu}_{em} \rangle) + \frac{\sin(\beta_{em,ex})}{\sqrt{2}} \cdot I_{sm} \left( \langle \mathbf{\mu}_{ex} \rangle = \frac{\mathbf{\mu}_{em} \times \langle \mathbf{y} \rangle}{|\mathbf{\mu}_{em} \times \langle \mathbf{y} \rangle|} \right) \right] \quad 4.2.$$

Here the integration is to be taken over all possible orientations of the emission dipole, brackets indicate unit vectors,  $\langle \mathbf{y} \rangle$  is the Cartesian unit vector perpendicular to the plane of incidence.

### 4.1.3. Results and discussion

In a first set of experiments, the excitation angle ( $\theta_{ex}$ ) was varied continuously, recording both the intensity of the reflected laser beam and the fluorescence intensity emitted vertically  $\theta_{em} = 0^\circ$  to the air side. Fig 4.5.a displays reflectivity data for samples with varying spacer thickness. Based on the position and shape of the surface plasmon minimum, a full characterisation of the optical parameters of each system was performed. They yield  $\epsilon_{prism}(\lambda_{ex})=2.26$ ,  $\epsilon_{gold}(\lambda_{ex})= -12,65 + i * 1,01$ ,  $d_{gold} = 44$  nm and  $\epsilon_{spacer}(\lambda_{ex})=2,38$ . The values for  $d_3$  from curve 1 to 7 are 9.8 nm, 15.3 nm, 23.9 nm, 32.4 nm, 41.4 nm, 50.7 nm, and 59.4 nm. The good agreement of the theoretical reflectivity curve with the measured data supports the applicability of the simple multilayer model to our system.



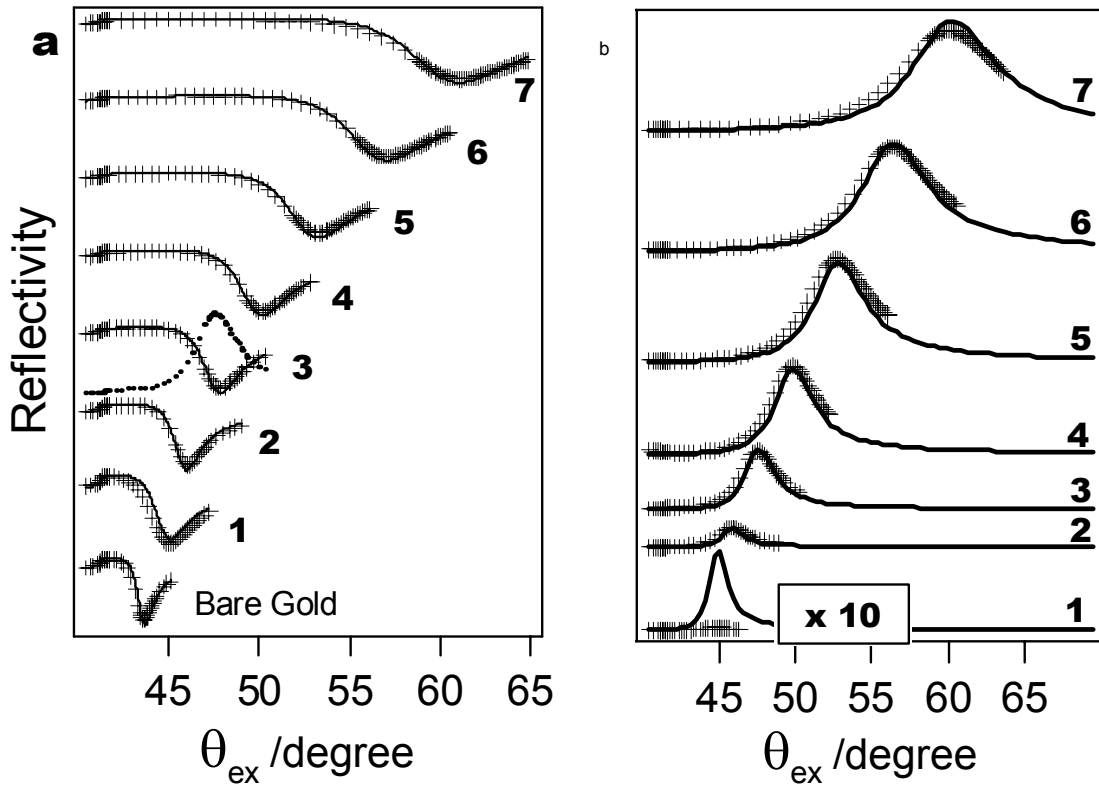


Fig. 4.5. (a) Measured reflectivity curves (crosses) for different spacer thickness. The solid lines are theoretical fits to the data. The datasets are vertically offset for clarity. In dataset 3 the fluorescence intensity is plotted over the reflectivity curve to illustrate the relative positions of reflectivity minimum and fluorescence maximum.

(b) – measured fluorescence intensity (crosses) emitted under  $\theta_{em}=0^\circ$  to the air side and the corresponding fit (solid line) Both experimental and theoretical values for the thinnest spacer were multiplied by 10 for clarity.

The experimentally obtained fluorescence is displayed together with the theoretically predicted curves in Fig 4.5.b. The curves exhibit a clear maximum following roughly the surface plasmon minimum with a slight displacement, indicating excitation of the dye via the surface plasmon electromagnetic field. To illustrate this, one extra fluorescence curve is added to the reflectivity data in Fig. 4.5.a. A factor common to all data sets was applied to scale the experimental data to theory. In addition, the nonradiative decay rate was adjusted for optimum agreement to be 0.5 times the radiative decay rate of a free dipole in vacuo. A remarkable agreement of experimental data with theory is found for all samples except the one with the thinnest spacer. For this sample, the measured fluorescence intensity is significantly reduced (roughly by a factor of 24). This observation was very surprising.

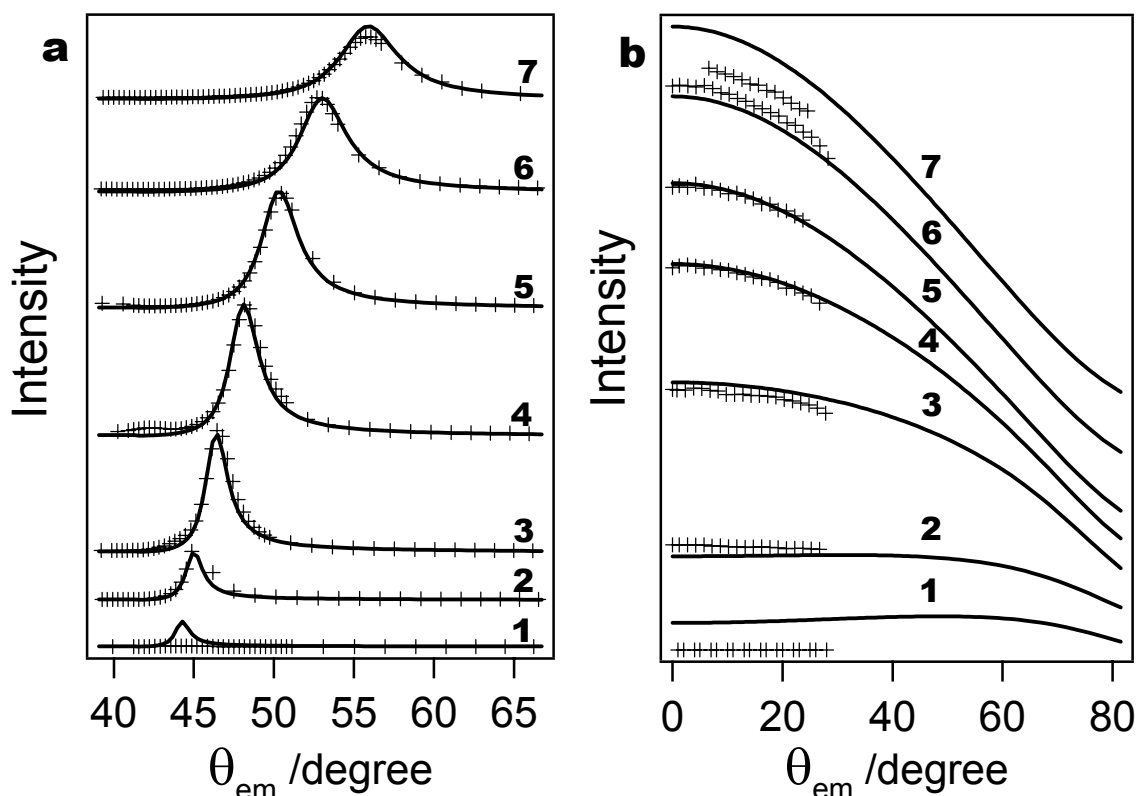


Fig. 4.6. Fluorescence intensity as a function of  $\theta_{em}$ , recorded through the prism (a) and through air (b). The numbers correspond to the same spacer thickness as in Fig. 4.5. Crosses are experimental data, straight lines the theoretical prediction. Different factors were applied to the experimental data in the two cases to obtain optimum agreement with theory (470000 for (a) and 640000 for (b)). The theoretical plots are based on the same material parameters as in Fig. 4.5. The curves are vertically offset for clarity. Note that the scaling on the intensity axis is different in a and b in order to make the wavelength dependence clearer.

Nonetheless it should be noted that intensity measurements were carried out by Campion et al.<sup>17</sup> for the phosphorescence of pyrazine in front of a nickel surface. In this study, a perfect agreement with theory was found for a spacer thickness that varied continuously between 0.5 and 10 nm. For the thickest spacer layer studied here ( $d_{spacer} = 59.4$  nm) the measured fluorescence intensity is somewhat lower than theoretically predicted, this deviation is tentatively assigned to the large resonance angle  $\theta_{ex}$  which leads to a wider area illuminated by the exciting beam which is not imaged perfectly onto the active area of the PMT.

In a second experiment, the direction of the incident light was kept fixed at a value leading to maximum excitation of the dye and the angle-resolved emission was measured by scanning the emission angle  $\theta_{em}$  with the PMT. This way, in one run both the angular distribution of the fluorescence emitted to the glass side and to the air was recorded. In Fig. 4.6., the experimental data are shown together with the corresponding calculations. As a basis for the calculation of the theoretical curves, the dielectric constants of gold and spacer at the emission wavelength ( $\lambda_{em} = 670$  nm) were determined by an independent surface plasmon reflectivity measurement at this wavelength (data not shown). The dielectric constants are found to be ( $\epsilon_{prism}(\lambda_{em})=2,25$ ,  $\epsilon_{gold}(\lambda_{em})=-14,94 + i 1.1$ ,  $\epsilon_{spacer}(\lambda_{em})=2.32$ ). The experimentally determined angular distribution of the emitted intensity is well described by the classical theory if emission through prism and emission to air are evaluated separately. It must be noted, though, that slightly different factors were used to scale the theoretical to the experimental values for the two sets of measurements. In the experiment the intensity emitted through the prism appears to be enhanced by a factor of 1.34 relative to the emission in air. The reduced intensities for the thinnest and thickest spacer layer appear in this measurement again.

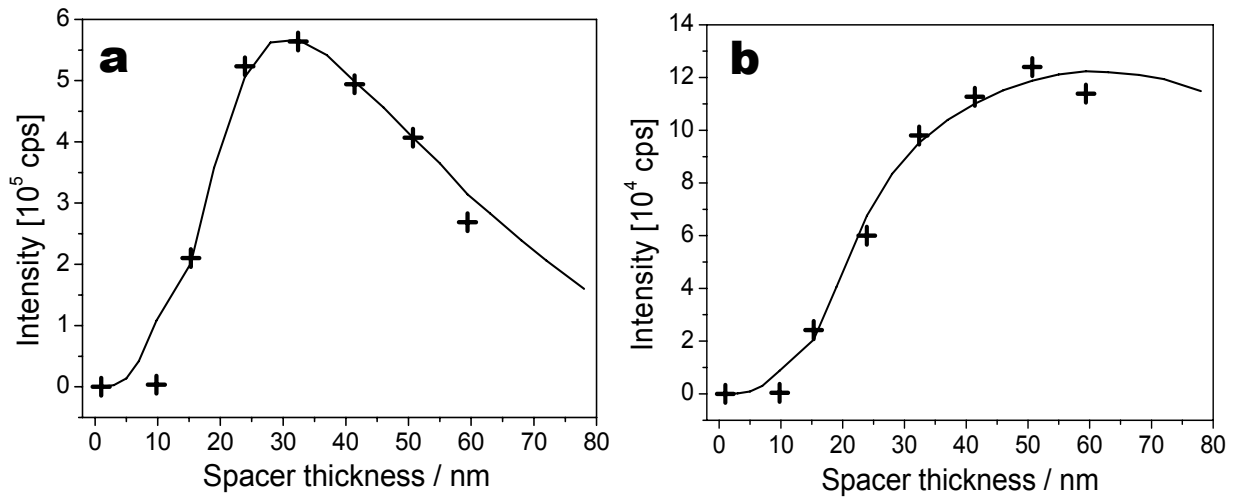


Fig. 4.7. Quantitative comparison between the maximum intensities measured through the prism (a) and through air (b). Crosses are experimental data, the straight line is the theoretical prediction. Identical material parameters and scaling factors as in Fig. 4.6. were used.

The intensity emitted to the air side is only slowly varying as a function of  $\theta_{em}$ , while for the thicker spacer layers maximum fluorescence is found at emission normal to the sample plane for thin spacer layers maximum intensity is found for different values for  $\theta_{em}$ . This observation should be of some importance for experimental designs where optimum fluorescence detection

along with suppression of background is sought. The radiation to the prism side is concentrated in one direction. This effect is due to intermediate surface plasmon excitation at the emission frequency.

The maximum fluorescence intensities through air and through the prism are compared in Fig. 4.7. Fluorescence emission through glass goes through a maximum at a spacer thickness of roughly 30 nm while maximum intensity through air is reached roughly at 50 nm. This clearly shows that surface plasmon - mediated emission is very effective for spacer thickness below roughly 40 nm. Note that for spacer thickness below 30 nm the intensity detected through the prism is roughly ten times higher than the intensity detected through air. For very thin spacer layers, the electromagnetic decay is dominated by processes that do not lead to photons at all, therefore only a very weak fluorescence signal is detected in this case.

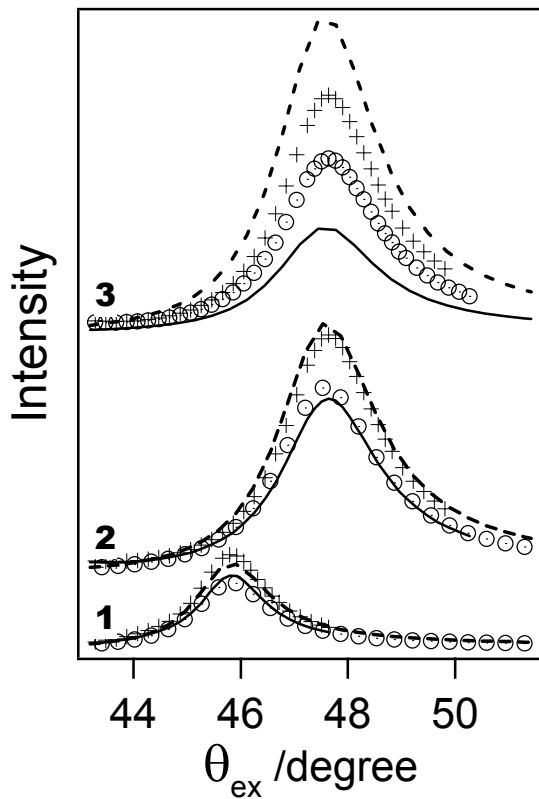


Fig. 4.8. Fluorescence intensity emitted to the air side normal to the sample plane, recorded separately for polarisation in the plane of incidence (crosses) and perpendicular to this (circles) for a spacer thickness of 15.3 nm (curve 1) and 23.9 nm (curve 2). The theoretical predictions which are assuming a  $\beta_{em,ex}=32.25^\circ$ , are plotted as solid and dashed line for polarisation in the plane of incidence and perpendicular to it, respectively. Curve 3 represents again the same data as curve 2 but the corresponding calculation is based on the assumption of collinear absorption and emission dipole moment ( $\beta_{em,ex}=0^\circ$ ).

Polarisation anisotropy was measured by placing a polariser in front of the PMT which was positioned to collect fluorescence to air at  $\theta_{em}=0^\circ$ . In Fig. 4.8., the measured data are displayed together with the theoretical prediction, assuming an angle  $\beta_{em,ex}$  of  $32.25^\circ$  between excitation and emission dipole moment in comparison to the result that would be obtained for collinear absorption and emission dipoles. With this value for  $\beta_{em,ex}$  satisfactory agreement between theory and experiment is reached, the calculation based on the assumption of collinear absorption and emission dipole  $\beta_{ex,em} = 0^\circ$  shows clear deviations from the experimental finding.

This proves that the relative orientation of transition dipoles must be taken into account in order to apply the classical electromagnetic model to molecular fluorescence close to a metal surface.

### **4.1.4. Conclusion**

The fluorescence of chromophores placed at variable distance from a metal surface was studied on a model system based on polyelectrolyte multilayers deposited on ultraflat template-stripped gold. A series of experiments was performed to verify the applicability of the classical theoretical model which was extended to take into account all photophysical parameters relevant to the real experiment. Intensities were recorded for varying excitation and emission direction and the polarisation anisotropy of the emitted light was studied. All experiments with spacer thickness above 15 nm indicate that the classical theoretical framework is appropriate for a quantitative description of the behaviour of fluorophores in front of a metal surface. The drastically reduced intensity for the sample with a thickness of 9 nm is clearly beyond our model. This work provides a full experimental verification of the theoretical description of a chromophore with dipolar character in front of a metal, taking into account several parameters that are of direct relevance for the experimentalist. This proves the usefulness of the classical theory in the design and optimisation of experimental schemes towards increased sensitivity in fluorescence-based sensor applications.

### **4.2. Reduced photobleaching of chromophores close to a metal surface**

In fluorescence spectroscopy, including studies on biological systems as well as for single molecules studies, it is crucial to obtain as many photons as possible from one molecule before it undergoes irreversible photobleaching. Working at liquid helium temperatures as well as embedding the dyes in a solid matrix have proven to enhance the lifetime of chromophores by orders of magnitude. In low temperature experiments individual dyes have been studied for hours, emitting more than  $10^{12}$  photons<sup>18</sup>. When working at room temperature with molecules in contact with the environment, exclusion of oxygen is another strategy to increase the lifetime of the molecules.<sup>19</sup> Though, these strategies are not applicable as soon as fluorescence spectroscopy is used as an analytical tool to elucidate biological processes, where temperature and chemical composition of the environment are determined by the needs of the process to be studied. In this case, another approach to increase the number of excitation-emission cycles, proposed in a theoretical paper by Enderlein<sup>20</sup> should prove to be useful. It relies on the concept of enhancing

the electromagnetic decay rate of the molecule by placing it in front of a metallic surface. As a consequence, the molecule will in average stay in the excited state for a shorter time and, assuming that photobleaching happens from the excited state with a constant rate, be able to undergo more excitation-emission cycles before being bleached. As an additional effect, the metal introduces new electromagnetic decay channels to the system, reducing the probability that a photon reaches the far field and is therefore detectable. As a consequence, careful optimisation is required to increase the total number of detectable photons for a given chromophore<sup>21</sup>.

A related concept has proven experimentally to enhance the brightness of semiconductor quantum dots. Shimizu et al.<sup>22</sup> placed semiconducting quantum dots on a rough metal film. They observed a strongly enhanced luminescence which they ascribed to enhancement of the electromagnetic emission rate, allowing the quantum dot to emit more photons before entering a dark state. They did not know the local environment of the emitters, therefore the observed effect could only be discussed qualitatively.

In the work presented in this chapter a planar multilayered system is used as a model structure for a quantitative experimental investigation of the effect of a nearby metal surface on the photostability of fluorescing dyes.

### 4.2.1. Experimental

For the measurements which will be discussed in this section the sample preparation techniques and the sample realization were the same as described in the previous section (section 4.1.). The experimental apparatus and geometry are as shown in fig. 4.3. The measurements were conducted at fixed emission angle  $\theta_{em}=0$ . The angle of excitation was also fixed at an angle  $\theta_{ex}$ , which was the angle of excitation of surface plasmon resonance or the angle where maximum fluorescence intensity was detected for a given sample thickness. The decrease of the fluorescence intensity with time was recorded for samples with separation distance between the fluorescing dye and the gold layer 11.5, 17.2, 26, 35.5, 43.9, 54 and 64 nm, respectively.

### 4.2.2. Theoretical modeling

In the previous section (4.1) it was demonstrated that the classical electromagnetic model as proposed by Chance et al.<sup>23</sup> is appropriate to predict the measured fluorescence intensities for varying spacer thicknesses if photobleaching effects are neglected. For this case, a random distribution of transition dipoles which does not change during the experiment could be assumed.

In this section, the rate equations based on this model are extended to include photobleaching from excited states of the individual chromophores in order to model the experimentally observed bleaching kinetics.

In the following, it is assumed that moderate excitation intensities are used such that the molecule is in the excited state only a very small fraction of the time and that intersystem crossing and saturation effects can be neglected.

In this case, the detectable intensity from a single dye molecule  $I_{sm}$  can be calculated from the excitation rate  $P_{ex}$ , the nonradiative emission rate  $P_{nr}$ , the total radiative emission rate  $P_{rad,tot}$  and the rate of emission into the solid angle covered by the photomultiplier,  $P_{em,PMT}$ .

$$I_{sm}(\boldsymbol{\mu}, \mathbf{x}) = C_1 P_{ex}(\boldsymbol{\mu}, I(\mathbf{x})) \frac{P_{em,PMT}(\boldsymbol{\mu})}{P_{rad,tot}(\boldsymbol{\mu}) + P_{nr}} = C_1 \frac{I_{ex}(\mathbf{x})}{I_{ex,0}} P_{ex}(\boldsymbol{\mu}, I_{ex,0}) \frac{P_{em,PMT}(\boldsymbol{\mu})}{P_{rad,tot}(\boldsymbol{\mu}) + P_{nr}} \quad 4.3.$$

with some constant  $C_1$  taking into account that not every photon is detected due to effects such as the quantum efficiency of the detector or losses at the filters. The rates are functions of the orientation of the transition dipole moment  $\boldsymbol{\mu}$  and, due to the inhomogeneous illumination, of the lateral position  $\mathbf{x}$  of the chromophore. This lateral dependence can be explicitly written by introducing  $P_{ex}$  for some arbitrary local  $I_{ex,0}$ .

Assuming that photobleaching happens exclusively from the excited state, the photobleaching rate  $P_{pb}$  is proportional to the time-averaged probability of finding the molecule in the excited state which is directly obtained from the transition rates. Therefore

$$P_{ph} = C_2 \frac{P_{ex}(\boldsymbol{\mu}, I(\mathbf{x}))}{P_{rad,tot}(\boldsymbol{\mu}) + P_{nr} + P_{ex}(\boldsymbol{\mu}, I(\mathbf{x}))} = C_2 \frac{P_{ex}(\boldsymbol{\mu}, I_0)}{P_{rad,tot}(\boldsymbol{\mu}) + P_{nr}} \quad 4.4.$$

with some constant  $C_2$  and assuming again sufficiently small excitation rates. The rates that are influenced by the nearby interface are displayed in Fig. 4.9. as a function of the layer thickness. In Fig. 4.9.a, the squared electrical field strength at the dipole position parallel and perpendicular to the gold surface is shown assuming illumination with unit intensity. Since  $P_{ex}$  is proportional to this quantity, a corresponding variation of the photobleaching rate with distance is to be expected for low excitation rates. For an ensemble of molecules, at spacer thicknesses below 30 nm, the increased electrical field parallel to the surface is on average almost compensated by the decreased perpendicular field. For thicker spacer layers, a decreased photobleaching simply due to decreased excitation rate for any orientation of the molecule is expected.  $P_{rad,tot}$  for the dye molecules is displayed in Fig. 4.9.b.

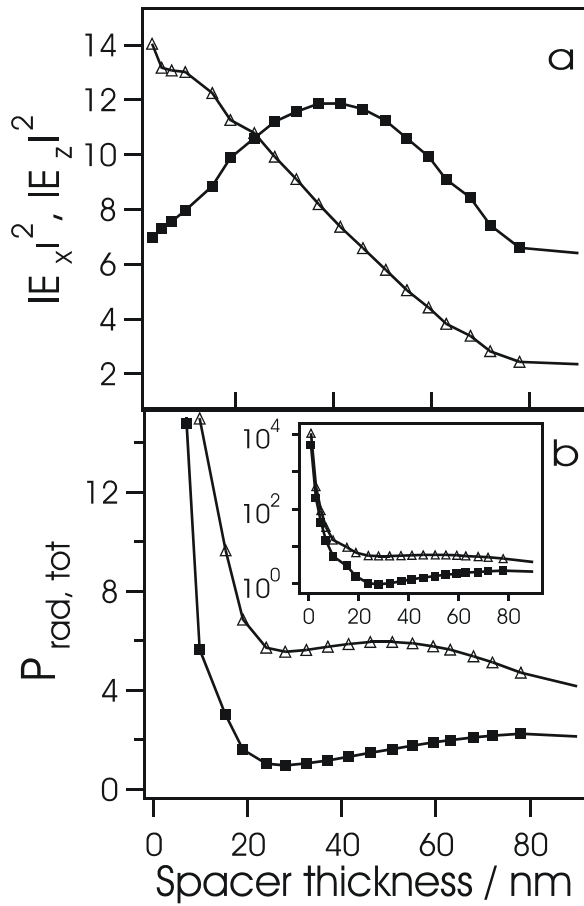


Figure 4.9. a) Calculated modulus squared of the exciting electromagnetic field perpendicular to the sample surface (z-axis, triangles) and parallel to it (x-axis, squares) for different spacer thickness, normalised to the electric field amplitude of the plane wave incident on the multilayered system. There is no electrical field along y. The incident light has transverse-magnetic polarisation and  $\theta_{ex}$  is adjusted for maximum electrical field. b) Total electromagnetic decay rate  $P_{em,tot}$  for a radiating dipole oriented parallel (triangles) and perpendicular (squares) to the sample surface as a function of layer thickness. In the inset of Fig. b, the same data is displayed with a logarithmic scale to show the behaviour for very small distances.

Again, a significantly different behaviour is found for dipoles oriented parallel and perpendicular to the interface. While at a spacer thickness of 26 nm perpendicular dipoles reach a minimum in the emission rate well below the value far away from the interface, there is still significant electromagnetic decay for the dipole parallel to the interface. As a common trend, a steep increase in the electromagnetic decay rate for spacer thicknesses below 20 nm is seen which should lead to a significantly increased photostability in this regime. After this more qualitative discussion of the general expected trend, we turn to a more quantitative description of our experimental situation.

The excitation rate of a molecule depends both on its lateral position on the sample (because the exciting beam has a nonuniform intensity distribution  $I(\mathbf{x})$ ) and on its orientation. Therefore, the detected intensity  $I_{tot}$  is obtained by performing a lateral and orientational integration over a chromophore population density  $n(\boldsymbol{\mu}, \mathbf{x})$  consisting of the single molecule contributions given by equation 4.3:

$$I_{tot} = \int d\mathbf{x} \int d\boldsymbol{\mu} \frac{I(\mathbf{x})}{I_0} \cdot n(\boldsymbol{\mu}, \mathbf{x}) C_1 P_{ex}(\boldsymbol{\mu}, I_0) \frac{P_{em,PMT}(\boldsymbol{\mu})}{P_{rad,tot}(\boldsymbol{\mu}) + P_{nr}} \quad 4.5.$$



It is assumed that the absorption and emission dipoles are collinear and the integration is to be taken over all possible dipole orientations. Time evolution of this quantity is given by the time dependence of the population density and can therefore be expressed by

$$\frac{dI_{tot}}{dt} = \int d\mathbf{x} \int d\boldsymbol{\mu} \frac{I(\mathbf{x})}{I_0} \frac{d}{dt} [n(\boldsymbol{\mu}, \mathbf{x})] \cdot C_1 P_{ex}(\boldsymbol{\mu}, I_0) \frac{P_{em,PMT}(\boldsymbol{\mu})}{P_{rad,tot}(\boldsymbol{\mu}) + P_{nr}} \quad 4.6.$$

The temporal evolution of the population density is obtained from Eq. 4.4. as

$$\frac{d}{dt} [n(\boldsymbol{\mu}, \mathbf{x})] = C_2 \frac{I(\mathbf{x})}{I_0} \cdot \frac{P_{ex}(\boldsymbol{\mu}, I_0)}{P_{rad,tot}(\boldsymbol{\mu}) + P_{nr}} n(\boldsymbol{\mu}, \mathbf{x}) \quad 4.7.$$

The solution of this differential equation would require the exact knowledge of the intensity profile of the exciting laser light which is not trivial to obtain. Nonetheless, the initial change in fluorescence intensity can be extracted without solving equation (4.7.). This calculation only requires the initial chromophore distribution which can be assumed to be homogenous and isotropic for the as-prepared sample, therefore  $n = n_0$ . In this case, Eqns. 4.6. and 4.7. yield

$$\begin{aligned} \left. \frac{dI_{ges}}{dt} \right|_{t=0} &= C_2 \cdot \int d\mathbf{x} \left( \frac{I(\mathbf{x})}{I_0} \right)^2 \cdot \int d\boldsymbol{\mu} n_0 \cdot C_1 P_{em,PMT}(\boldsymbol{\mu}) \cdot \left( \frac{P_{ex}(\boldsymbol{\mu}, I_0)}{P_{rad,tot}(\boldsymbol{\mu}) + P_{nr}} \right)^2 = \\ &= C_3 \cdot \int d\boldsymbol{\mu} P_{em,PMT}(\boldsymbol{\mu}) \cdot \left( \frac{P_{ex}(\boldsymbol{\mu}, I_0)}{P_{rad,tot}(\boldsymbol{\mu}) + P_{nr}} \right)^2 \end{aligned} \quad 4.8.$$

This quantity is directly calculated by classical electromagnetic theory.  $C_3$  is a constant prefactor. In order to extract a quantity that is independent of the (arbitrary) concentration of chromophores, the initial intensity change is normalised by the total initial intensity  $I_{ges,t=0}$ , which is calculated (up to a constant factor) from equation 4.5. assuming again homogeneously distributed chromophores. The resulting quantity, the relative change in intensity, can be interpreted as an averaged photobleaching rate. This will be the quantity to be compared with the experimental data.

### 4.2.3. Results and discussion

Fig. 4.10. shows the measured intensities as a function of time, normalised to the initial intensity. It was observed in the experiment that the intensity showed some irregular changes like accelerated decrease or even increase in the range of  $\pm 1\%$  during the first 20 seconds. This may be due to thermal effects in the optical components in the exciting beam, probably heating of the gold layer and the underlying glue. For this reason, in all datasets the first 20 seconds were not

used for the further evaluation, this procedure is justified in the present case since the overall change in intensity during this time is small enough that the assumption of a homogenous and isotropic dye distribution is still justified. For two values of the spacer thickness, five datasets each are shown, already indicating a slower decay for the sample with  $d_{spacer} = 17.2$  nm compared to the one with  $d_{spacer} = 26$  nm.

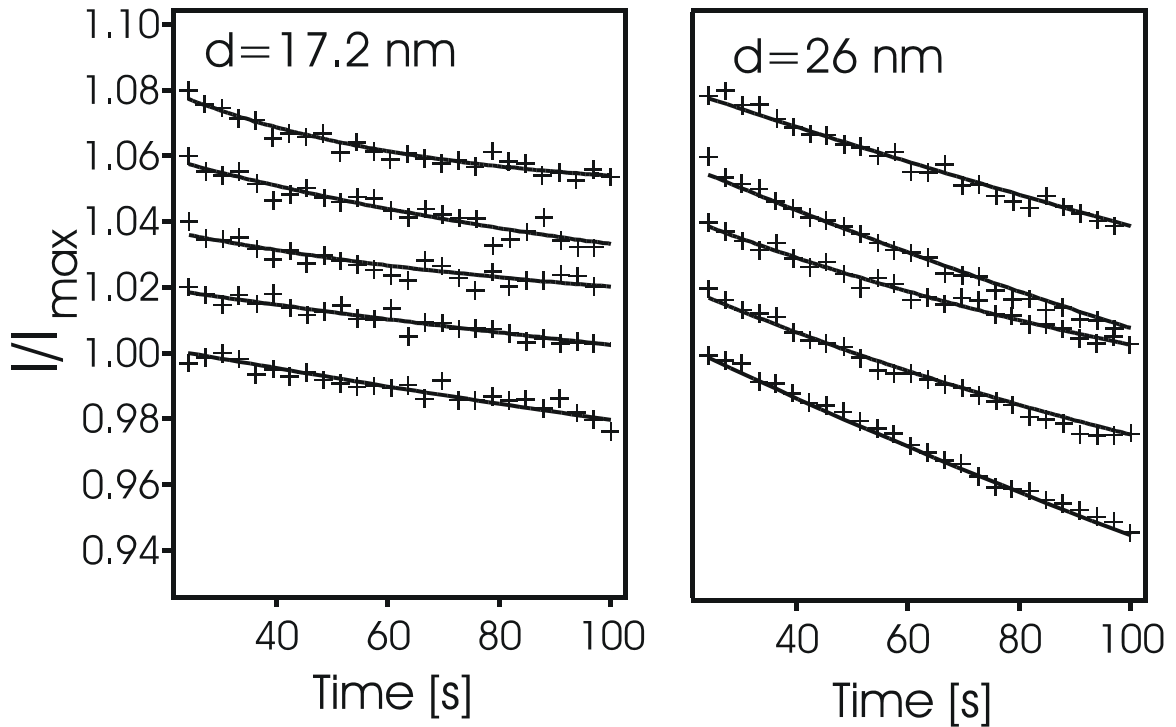


Fig 4.10. Normalised fluorescence intensity as a function of time, for two representative values for  $d_{spacer}$  as indicated in the plot, five measurements were taken each. The crosses are experimental data and the straight lines fits as explained in the text. The curves are vertically offset for clarity.

From this data, initial slopes were calculated by fitting an exponential function with an offset to the experimental points and calculating the slope of this function for  $t = 0$ . This fitting function was chosen for convenience. It describes the initial behaviour satisfactorily and allows for a precise determination of the initial slope. It is not based on a physical model and not suited to describe the experimental data for longer time intervals after significant bleaching has taken place.

The comparison between experiment and theory for the relative initial change in intensity is given in Fig. 4.11. Good agreement between the theoretical prediction and the experimental

result is found, with a maximum photobleaching occurring at a spacer thickness of roughly 25 nm.

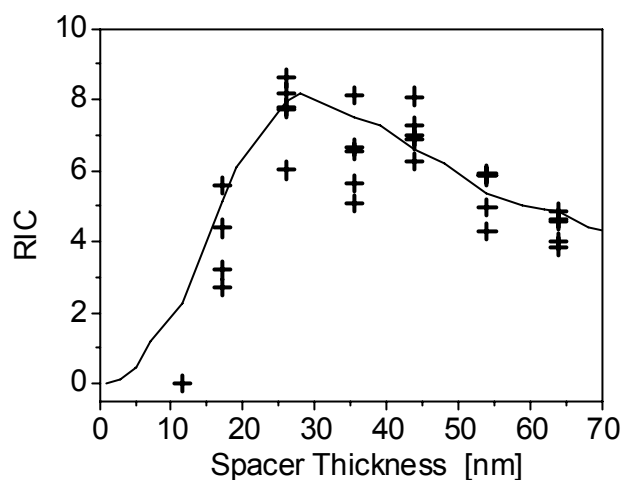


Fig. 4.11. Initial intensity change as determined experimentally (each cross corresponds to decay curve as displayed in Fig. 4) in comparison to the theoretical prediction (straight line). The theoretical curve was scaled to optimum matching of the data.

Closer to the interface, metal-enhanced emission leads to a longer (chemical) lifetime while for thicker spacer layers the increased photosability can be mainly ascribed to the decreasing excitation rate. The experimental point at a spacer thickness of 10.5 nm is not described by the model, actually, a slight increase of fluorescence intensity with time was observed experimentally, indicating a failure of the classical electromagnetic model. In the previous chapter (4.1.) on fluorescence intensities in this multilayered system, a similar disagreement for very thin spacer layers was found. This led already at that point to the conclusion that the classical model is not applicable for layer thickness below 15 nm.

### 4.2.4. Conclusion

Nonetheless, for larger spacer thicknesses the conclusion can be drawn that the experiment gives quantitative support for the model describing the photostability of organic dyes that was outlined above. Essentially, for spacer layers below 20 nm, the strongly increased electromagnetic decay rate allows the chromophore to undergo more excitation-emission cycles before photobleaching while the longer lifetime for larger spacer thickness is due to a decrease in excitation rate.

### 4.3. Single molecules fluorescence near a flat gold interface

#### 4.3.1. Introduction

Although single molecule optical spectroscopy became possible in the last decade<sup>24, 25</sup> to our knowledge there is only one reported study on single fluorescing molecules in the vicinity of a metal interface<sup>26</sup>. In this work Yokota et al. imaged single fluorescent-labeled proteins with a surface plasmon fluorescence microscopy set-up.

In this experiment the chromophore was placed at different separation distance to a metal film by a dielectric spacer layer and excited by the surface plasmon field of the metal. In comparison to the work of Yokota, here the excitation and imaging of the fluorescing dye was conducted from the gold side thus providing a novel experimental geometry in single molecule studies, leaving the other side free, which can potentially be used for a characterization by another technique (for example AFM). This study aims to answer some important questions as what the shape of the excitation pattern of a single fluorescing dye with different dipolar orientation is and how it compares with the theoretically calculated one. Secondly the discrepancy between theory and experiment in the ensemble experiments at the very close proximity to the gold film, noted in the previous sections (4.1.), will be addressed at a single molecule level.

#### 4.3.2. Experimental

Samples were prepared as in the previous section (4.1.). Polyelectrolyte layers of PAH/PSS were deposited on gold functionalized by 3-MPA. The gold film was thermally evaporated on Microscope cover slip (Menzel Glässer). Before use both polyelectrolytes were purified in order to reduce to minimum the fluorescence background due to contamination. PAH was cleaned by dialysis (Membrane tube MWCO 3 500, Spectrum Laboratories, Inc., USA, was used). The dialysis was conducted for six days as the water was exchanged twice a day. PSS was purified by a controlled precipitation method. The polymer was dissolved in water and then the solution was transferred slowly (drop by drop) in cooled near the frizzling temperature ethanol. The precipitation was then filtered and dried in vacuum. After this treatment the fluorescence background was reduced about 8 times thus allowing for single molecules measurements. Single fluorescing dyes were deposited electrostatically by immersing the samples in a dye solution with concentration of  $10^{-10}$  mol/l for 1 minutes.

The measurements were conducted in a confocal microscope set up as depicted in fig. 4.12. A beam of a He-Ne laser is directed to a microscope objective and focused on the gold

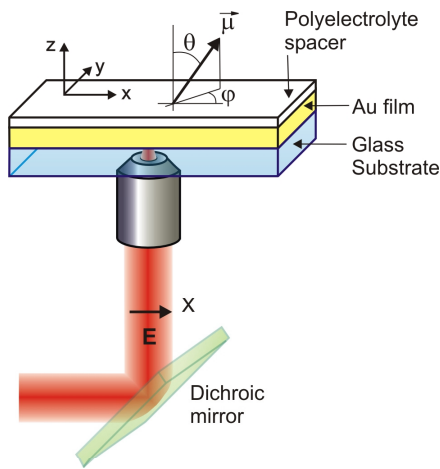


*Figure 4.12. The experimental geometry. The laser beam is directed to the objective and focused on the gold side of the sample. Fluorescence is collected at the same side with the same microscope objective. Here,  $x$ ,  $y$  and  $z$  are the Cartesian coordinates.  $\theta$  is the polar angle,  $\varphi$  is the azimuthal angle and  $\mu$  is the dipole moment.*

side of the sample. Fluorescence coming through the gold film is collected from the same side by a microscope objective, as the appropriate filters for blocking the reflected laser beam are set. Images were created by scanning in  $x$  and  $y$  direction over a given area of the interface.

### 4.3.3. Results and discussion

The images shown in figure 4.13. are the theoretically calculated excitation patterns of dipoles with  $x$ ,  $y$  and  $z$  orientation placed at 20 nm separation distance to the metal interface. Firstly, remarkable is the different shape of the patterns. Secondly, it is not surprising the difference in the intensity. It is clear that the image showing the dipoles lying in  $y$  direction looks dark, because the excitation light is linearly polarized along the  $x$ -axis. The  $z$  pattern is approximately 2.5 times stronger than the  $x$  one. This is due to the electromagnetic boundary conditions at an interface and due to the presence of the gold interface.

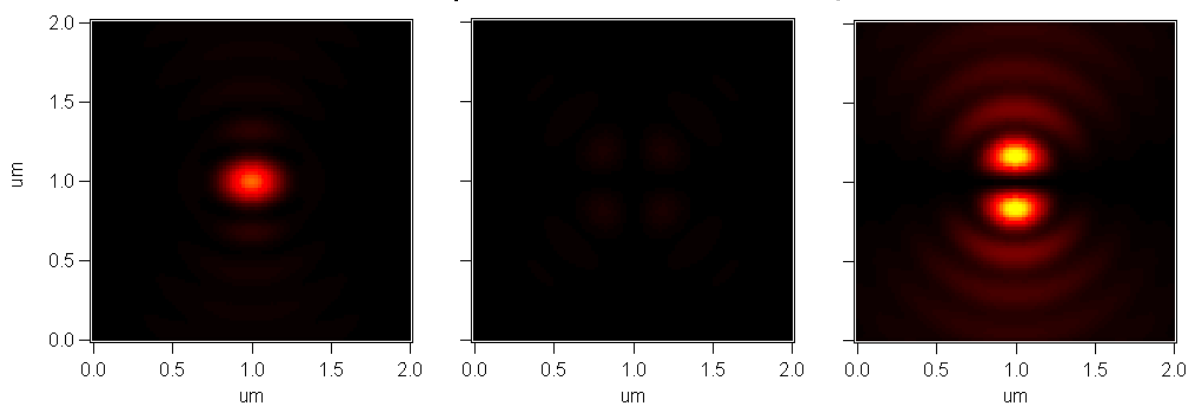


*Figure 4.13. Calculated excitation patterns of dipoles with  $x$ ,  $y$  and  $z$  orientation at a separation distance to the metal interface of 20 nm.*

Fig. 4.14.a shows an image of the surface of a PAH/PSS multiplayer system composed of 4 bilayer and DiIC1(5) subsequently deposited. It is not surprising why only the dipoles possessing components lying in z direction appear on the image. As it was discussed above z patterns are much stronger than x and y. The perfect similarity between measured and calculated z pattern is remarkable (fig. 4.14.b).

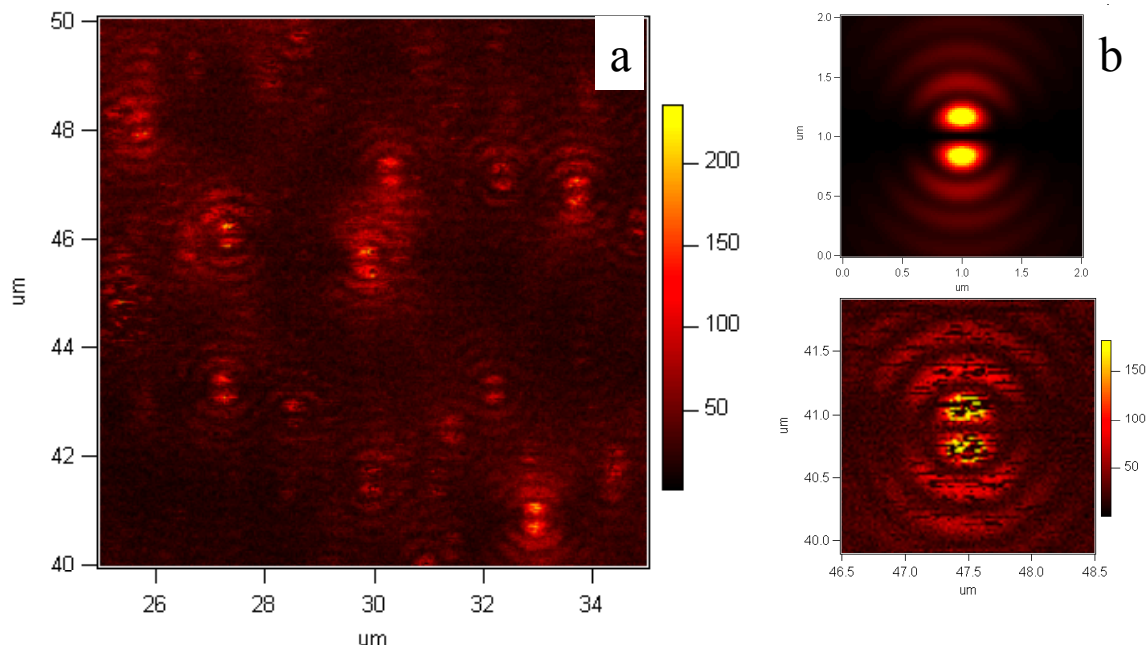


Figure 4.14. a) Confocal image of single molecules at approximately 23 nm separation distance to a gold interface. b) shows comparison between experimentally measured (down) and theoretically calculated (up) pattern of a dipole lying in z direction.

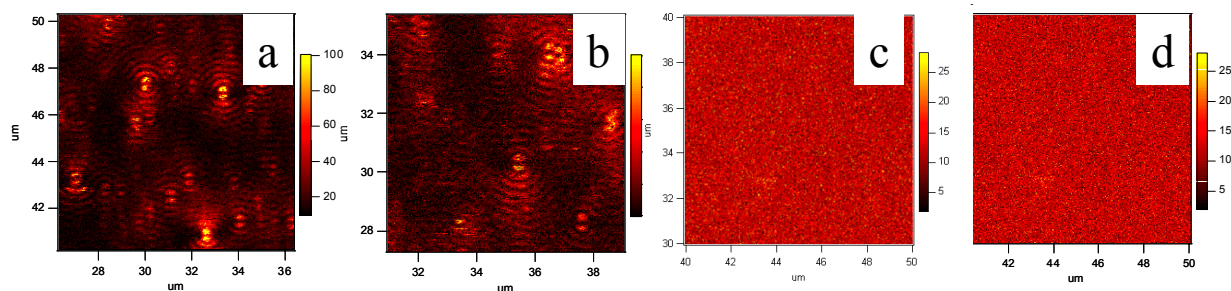


Figure 4.15. Images of DiIC1(5) single molecules at separation distances of 23 nm a), 15 nm b), 10 nm c) and 4.5 nm d) to a gold interface.

Fig. 4.15. shows an images of dipoles separated from the gold interface with four a), three b), two c) and one d) bilayer of PAH/PSS. The intensity of the patterns in image a) is about 2.7.times stronger compared to that in b). In images c) and d) no patterns can be seen, which means then the fluorescence is completely quenched due to the proximity of the gold

interface This inspection at single molecule level is one important confirmation of the experimental results with an ensemble of molecules discussed in the previous section 4.1, where strongly reduced fluorescence intensity at the very short separation distance was found (fig. 4.7.).

### **4.3.4. Conclusion**

This study was the first experimental demonstration of the behaviour of single fluorescing molecules at different separation distance to a gold interface. Excitation patterns were imaged and a perfect correlation in shape and intensity was found. Only  $z$  patterns were found since they are much stronger than  $x$  and  $y$ . In addition this study was a confirmation of the findings discussed in section 4.1., where the measured intensity at the very close proximity (0-10 nm) to a gold film was much lower than theoretically predicted one.

## **4.4. Cd-Se semiconducting nanoparticles in the vicinity of a gold interface**

### **4.4.1. Introduction**

In this section the applicability of the model calculation of the fluorescence near a metal interface to semiconducting nanoparticles will be addressed. Cd-Se nanoparticles have attracted a great scientific attention in recent years due to their size dependent fluorescence properties, which makes them interesting in sensing and device fabrication.<sup>27, 28</sup>

### **4.4.2. Experimental**

Samples for this experiment were prepared as in section 5.1. except few details. Firstly, the thickness of the gold film was about 30 nm. Secondly, the polyelectrolyte multiplayer system was terminated by a positively charged layer of PAH thus allowing for the electrostatic deposition of negatively charged species.

Cd-Se nanoparticles were obtained in collaboration with Alf Mews<sup>29</sup>. The particles consist of Cd-Se core covered by a ZnS shell. The particles surface is covered by ligand shell of mercaptoacetic acid thus the particles are negatively charged in water. The size of the particles was 3-4 nm. The excitation and emission spectra of the particles showed maximum excitation wavelength of 536 nm, and maximum emission wavelength of 548 nm. A layer of Cd-Se

semiconducting nanoparticles was deposited on a positive PAH surface by the immersion of the substrate into the solution of particles for 30 minutes. Then the sample was washed with water and dried.

The experimental set-up was the same as in section 5.1. The measurements were conducted at constant angle of emission (0 degree) and varying the angle of excitation. For the excitation was used green,  $\lambda = 532$  nm laser. 550 nm Raman filter was used for the selection of the emission wavelength.

**4.4.3. Results and discussion**

The reflectivity scans of bare gold film (solid curve), 7 layers of PHA/PSS (dot dashed curve) and after deposition of Cd-Se nanoparticles are shown in fig. 4.16 . The first impression is the very broad plasmon resonance dip of the reflectivity curves. The plasmon resonance shifts to a very large angle after deposition of even thin dielectric spacer layer. After deposition of a layer of particles the resonance angle shifts further on the right. All this is due to the optical response of the gold film at that wavelength. However, one can fit the reflectivity curves and extract the thickness of each layer as well as the dielectric constants

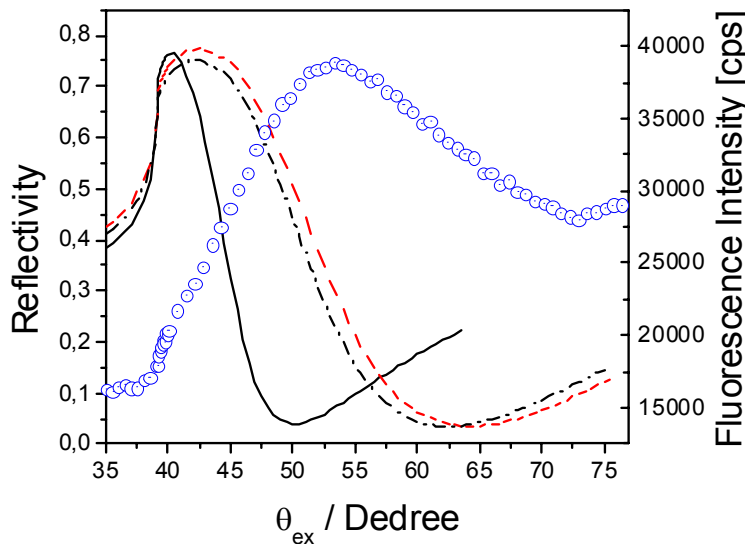


*Figure 4.16. Reflectivity curves of bare gold (solid curve), 7 layers of PHA/PSS (dash-dotted curve) and after deposition of Cd-Se nanoparticles (dashed curve). The open circles show the fluorescence emitted from the nanoparticles.*

at that wavelength. The thickness of the gold film was estimated to be 37.3 nm with  $\epsilon' = -4.85$  and  $\epsilon'' = 2.35$ . The polyelectrolyte spacer was 17 nm with  $\epsilon' = 2.8$ . Thickness and optical constants of the layer of semiconducting nanoparticles were not extracted since independent



AFM measurements showed that the particles tend to aggregate and pile of the surface which leads to inhomogeneous film in thickness and optical density.

The fluorescence intensity (fig. 4.16. open circles) follows the minimum of the reflectivity but the maximum is much more displaced on the left compared to the measurements with 633 nm laser shown in section 4.1.

Model calculations were carried out in order to show the applicability of the model described in the previous section to this system. Fig. 4.17.a shows the calculated intensities for 7, 11, 17, 26, 34 nm spacer thickness (solid curves) as a function of the angle of excitation. The markers are the measured fluorescence at 17 nm separation distance. In fig. 4.17.b are shown only the measured and calculated intensities for 17 nm separation distance. The good angular correlation between measurement and calculations is notable. This shows the applicability of our model systems to study variety of fluorescing species in the vicinity of a metal interface.

Samples with larger separation distance between the Cd-Se semiconducting nanoparticles and the gold interface are not investigated experimentally since the large shift of the plasmon dip of the reflectivity curves to the right makes the measurements not possible.

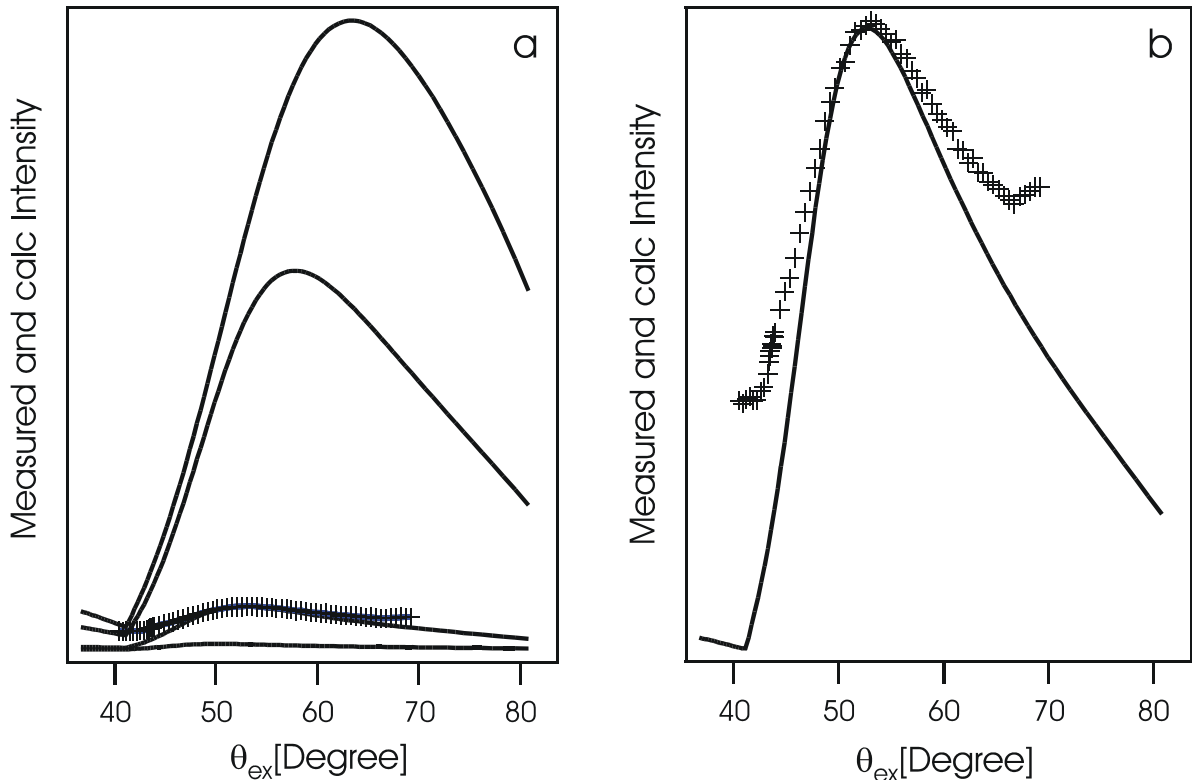


Figure 4.17. a) Calculated fluorescence intensity for 7, 11, 17, 26, 34 nm spacer thickness (solid curves) as a function of the angle of excitation. The markers represent the measured data. b) Measured and calculated data for 17 nm separation distance.

One possibility would be the use of a higher refractive index prism and glass substrate. However, in that case the utilisation of template stripped gold would be impossible since appropriate optical glue with an appropriate refractive index is not available. Another possibility would be a silver layer. Unfortunately, all attempts for preparation of template stripped silver layer failed. It was impossible to fabricate silver surface with acceptable quality due to sheets of mica sticking to the metal. This is probably due to the stronger adhesion of mica to silver compared to gold.

### 4.4.4. Conclusion

The behaviour of Cd-Se semiconducting nanoparticles in the vicinity of a gold interface was probed experimentally and modelled theoretically. Although a detailed experimental study was not possible due to the optical response of the system at the wavelength needed for the excitation of the nanoparticles, this study shows the applicability of our model system to a different kind of fluorescing species.

### References:

- <sup>1</sup> Knobloch, H., Brunner, H., Leitner, A., Aussenegg, F. Knoll, W. *J. Chem. Phys.* **1993**, *98*, 10093.
- <sup>2</sup> Gerbshtein, Y. M., Merkulov, I. A., Mirlin, D. N. *Pis'ma Zh. Eksp. Teor. Fiz.* **1975**, *22*, 80.
- <sup>3</sup> Weber, W. H., Eagen, C. F. *Opt. Lett.* **1979**, *4*, 236.
- <sup>4</sup> Benner, R. E., Dornhaus, R., Chang, R. K. *Opt. Comm.* **1979**, *30*, 145.
- <sup>5</sup> Pockrand, I., Brillante, A., Möbius, D. *Chem. Phys. Lett.* **1980**, *69*, 499.
- <sup>6</sup> Liebermann, T., Knoll, W. *Colloids and Surfaces A*, **2000**, *171*, 115.
- <sup>7</sup> Yokota, H., Saito, K., Yanagida, T. *Phys. Rev. Lett.* **1998**, *80*, 4606.
- <sup>8</sup> Enderlein, J. *Biophys. J.* **2000**, *78*, 2151.
- <sup>9</sup> Bartko, A.P., Dickson, R.M. *J. Phys. Chem. B* **1999**, *103*, 11237.
- <sup>10</sup> Sick, B., Hecht, B., Novotny, L. *Phys. Rev. Lett* **2000**, *85*, 4482.
- <sup>11</sup> Kreiter, M., Prummer, M., Hecht, B. Wild, U.P. *J. Chem. Phys.* **2002**, *117*, 9430.
- <sup>12</sup> Drexhage, K.H., Fleck, M., Kuhn, H. Schäfer, F.P., Sperling, W. *Ber. Bunsenges. Phys. Chem.* **1966**, *70*, 1179.
- <sup>13</sup> Drexhage, K.H. *Sci. Am.* **1970**, *222*, 108.
- <sup>14</sup> Kuhn, H. *J. Chem. Phys.* **1970**, *53*, 101.

- <sup>15</sup> Amos R.M., Barnes, W.L. *Phys. Rev. B* **1997**, *55*, 7249.
- <sup>16</sup> Fattering, C., Lukosz, W. *J. Luminesc.* **1984**, *31 & 32*, 933.
- <sup>17</sup> Campion, A., Gallo, A.R., Harris, C.B., Robota, H.J., Whitmore, P.M. *Chem. Phys. Lett.* **1980**, *73*, 447.
- <sup>18</sup> Kummer, S., Basche, T., Bräuchle, C. *Chem. Phys. Lett.* **1994**, *229*, 309.
- <sup>19</sup> Mei, E., Tang, J. Y., Vanderkooi, J. M., Hochstrasser, R. M. *J. Am. Chem. Soc.* **2003**, *125*, 2730.
- <sup>20</sup> Enderlein, J. *Chem. Phys* **1999**, *241*, 1.
- <sup>21</sup> Aussenegg, F. R., Leitner, A., Lippitsch, M.E., Reinisch, H. Riegler, M. *Surf. Sci.* **1987**, *189*, 935.
- <sup>22</sup> Shimizu, K. T., Woo, W. K., Fisher, B. R., Eisler, H. J., Bawendi, M. G. *Phys. Rev. Lett.* **2002**, *89*, 117401.
- <sup>23</sup> Chance, R.R., Prock, A. Silbey, S., *Adv. Chem. Phys.* **1978**, *37*, 1-65.
- <sup>24</sup> Xie, X. S., Dunn, R. C. *Science*, **1994**, *265*, 361–364.
- <sup>25</sup> X. S. Xie and J. K. Trautman, *Annu. Rev. Phys. Chem.* **1998**, *49*, 441–480.
- <sup>26</sup> Yokota, H., Saito, K. Yanagida, T. *Phys. Rev. Lett.* **1998**, *80*, 4606–4609.
- <sup>27</sup> Peng, X., Manna. L., Yang, W., Wickham, J., Scher, E., Kadavanich, A., Alivisatos, A. P. *Nature* 2000, *404*, 59-61.
- <sup>28</sup> Peng, Z. A., Peng, X. *J. Am. Chem. Soc.* 2001, *123*, 183-184
- <sup>29</sup> Department of Physical Chemistry, University “Johannes Gutenberg”, Mainz

## **5. Gold nanoparticles and gold nanowires – surface modification and synthesis**

The current chapter is devoted to monolayer protected gold nanoparticles and gold nanowires. Firstly, in section 5.1. a strategy for surface modification of citrate reduced gold nanoparticles is presented. In section 5.2. a new route for the synthesis of monolayer protected gold nanoparticles with sizes above 10 nanometers is described. In the last section 5.3. the synthesis of long aspect ratio gold nanowires in aqueous solution is demonstrated.

### **5.1. Surface Modification of Citrate-reduced Colloidal Gold Nanoparticles with 2-Mercaptosuccinic Acid**

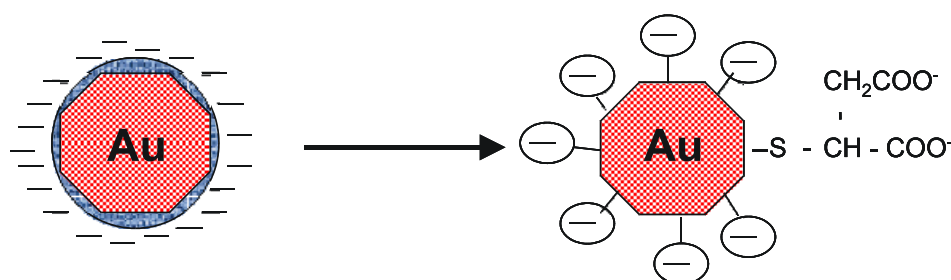
#### **5.1.1. Introduction**

According to the well-established gold-thiol chemistry in the formation of self-assembled monolayers (SAMs),<sup>1,2</sup> the undefined ionic species on citrate-reduced gold nanoparticle surface can be replaced with a self-assembled monolayer of certain thiolate derivatives, as demonstrated by a few early papers.<sup>3,4,5,6</sup> In their pioneering work on the electrophoretic deposition of a 2-D array of colloidal gold particles on a conductive solid surface, Giersig and Mulvaney demonstrated that the stabilizing citrate could be replaced on the particle surface by several water soluble or insoluble thiols.<sup>3</sup> Later on, as an extension of their interest on the self-assembled monolayer formation on planar gold surfaces, Whitesides et al. systematically explored the chemical adsorption of a series of alkanethiols with different terminal groups onto aqueous phase dispersed gold nanoparticles.<sup>4</sup> A similar approach was adopted by Sastry et al., who introduced carboxylic terminals on the gold nanoparticle surface by exchanging the adsorbed ionic layer with a chemically adsorbed monolayer of 4-carboxythiophenol.<sup>5</sup> Very recently, Aslan and Perez-Luna accomplished the surface modification of gold nanoparticles with 11-mercaptopundecanoic acid and 16-mercaptohexadecanoic acid in the presence of a nonionic surfactant, Tween 20.<sup>6</sup>

In this work, the goal was to modify citrate-reduced gold nanoparticles with 2-mercaptosuccinic acid (MSA). The modifier was chosen on the basis of the following considerations: Firstly, as a normal thiol derivative, chemical adsorption to the particle surface

## 5. Gold nanoparticles and gold nanowires – surface modification and synthesis

through Au-S bonding is anticipated; secondly, it has similar structural features as citric acid with dissociable carboxylic groups that will enable the electrostatic repulsion required to maintain the colloid stability after modification without a need for additional additives; thirdly, it is well-soluble in water so that surface modification reactions can be conducted in an aqueous phase without the risk of irreversible flocculation induced by the organic additives, which are necessary to facilitate the solubilisation of particular thiols used before.<sup>3-6</sup> Scheme 5.1. shows the surface structure of unmodified and modified particles.



*Scheme 5.1. (left) Gold nanoparticles obtained by the citrate reduction method possessing just physically adsorbed ions on their surface. The image on the right shows the surface structure of the particles after surface modification.*

It should be noted that functionalised Au particles with a mean diameter below 10 nm are easily accessible following the method of Brust et al.,<sup>7</sup> by which MSA-capped gold nanocrystals in this size regime were reported by Chen et al..<sup>8</sup> However, this synthetic scheme is not suitable to obtain functionalized gold particles with a size above this limit. In contrast, the citrate reduction method is more flexible in terms of size control; therefore, surface modification of the citrate reduced gold nanoparticles might be a choice to bridge this size gap. We are not the first to choose MSA as the modifier, an idea first applied by Kimura et al., who described a simple procedure for the surface modification of 5.8 nm citrate-reduced gold nanoparticles with MSA.<sup>9</sup> More recently, the same group used the MSA-modified gold nanoparticles as a model system for the theoretical calculation and experimental measurement of surface potentials by taking advantage of the molecularly-defined particle surface.<sup>10</sup> Both papers focused mainly on a particular application of the MSA modified gold nanoparticles, with only a brief description of the modification procedure,

and even less attention was paid on the characterization of the properties of the modified system.

In order to derive a better understanding of the characteristics of the MSA-modified gold nanoparticles, we performed a series of comparative experiments to see the difference between the as-prepared samples and the modified ones, and to evaluate the influence of the surface modification. Such differences should reflect structural change(s) of the surface due to the presence of the chemically adsorbed thiol monolayer on the modified particles.<sup>11</sup> The present work will add some new insight into the physico-chemical features of modified gold nanoparticles.

### **5.1.2. Experimental Section**

Hydrogen tetrachloroaurate(III) trihydrate, trisodium citrate dihydrate (99+%), hydroxylamine hydrochloride(99 %), and potassium cyanide (97 %) were obtained from Aldrich, 2-mercaptosuccinic acid (MSA, 99 %), and sodium sulfate from Acros, hydrochloric acid (37 %), sodium hydroxide, and sodium chloride from Riedel-de Haen. All the reagents were used as received. Milli-Q water with resistivity  $>18\text{M}\Omega\cdot\text{cm}$  was used throughout the experiments.

Gold colloids were synthesized by citrate reduction of Hydrogen tetrachloroaurate(III) trihydrate, as described in Chapter 3.4. The colloidal suspension prepared this way had a conductivity of  $380\pm 20\mu\text{S}/\text{cm}$ , an initial pH of  $6.0\pm 0.3$ , and a mean particle size of  $19\pm 2$  nm as determined by scanning electron microscopy (SEM).

Surface modification reactions were performed under stirring at  $50\text{ }^\circ\text{C}$  for 8~12h by mixing a certain volume of as-prepared gold colloids with an aqueous solution containing a large excess of MSA (typically, 100 ml as-prepared colloid with 15 ml  $1\times 10^{-2}$  mol/l  $\text{Na}_2\text{-MSA}$ ), equivalent to 50~100 monolayers/particle, estimated by assuming that the occupied surface area by a single thiol molecule is ca.  $0.20\text{nm}^2$ .<sup>12</sup> The thiol was introduced as its sodium salt by stoichiometrical neutralization with sodium hydroxide. The resulting suspension had a conductivity of  $580\pm 20\mu\text{S}/\text{cm}$ , and an initial pH of  $6.0\pm 0.3$ .

After reaction, both the as-prepared colloids and the modified samples were dialyzed against freshly prepared milli-Q water or a 0.1%  $\text{Na}_3\text{-citrate}$  solution through Spectra/Por 3 tubing (Spectrum Laboratories, Inc.) for a certain period of time during which water or citrate solution outside the tubing was refreshed for several times, until the two systems reached the same level of

conductivity ( $120\pm 10\mu\text{S}/\text{cm}$  for dialysis against water and  $820\pm 10\mu\text{S}/\text{cm}$  against  $\text{Na}_3\text{-citrate}$ ) and pH ( $5.2\pm 0.1$  against water and  $7.4\pm 0.1$  against  $\text{Na}_3\text{-citrate}$ ), monitored with an integrated pH/conductometer (Hanna Instruments, Inc.). Although this treatment can not completely remove the excess MSA from the modified sample, it is an indispensable measure to ensure that the modified and unmodified samples have similar supporting electrolytes enabling the comparative tests described in the next section.

Optical absorption spectra were measured with a UV/VIS/NIR spectrophotometer (Lambda 9, Perkin-Elmer) in a standard  $1\text{cm}\times 1\text{cm}\times 3.5\text{cm}$  quartz cuvette. Particle morphology was observed with a LEO 1500 field-emission scanning electron microscope (LEO Electron Microscopy Ltd). Samples for the SEM characterization were prepared by immobilization of gold nanoparticles onto silicon wafers pre-modified with 3-aminopropyltrimethoxysilane<sup>13</sup> as described in Chapter 3.1. For transmission FTIR measurements a Nicolet 730 FTIR spectrometer was used. A lab-made surface plasmon resonance spectrometer (SPR), as described elsewhere,<sup>14</sup> (Chapter 3.6.) was used for the on-surface etching experiments.

### **5.1.3. Results and Discussion**

#### **Spectral evidence for the modification**

In order to obtain direct evidence for the surface modification, FTIR measurements were performed on both the unmodified and modified samples. By salting out from suspensions of both samples with  $1\text{mol}/\text{l}$   $\text{NaCl}$  or  $1\text{mol}/\text{l}$   $\text{Na}_2\text{SO}_4$ , solid precipitates could be collected after centrifugation.<sup>15</sup> The precipitates were repeatedly re-dispersed in sufficient water and centrifuged for several times in order to remove any residual salt, unbound thiol, and citrate, then dried in vacuum at room temperature. During this process, the modified particles could be easily re-dispersed in water while the unmodified one could not, indicating that the modified particles might have a stabilizing layer persistent to the copious rinsing with water.

KBr pellets of the precipitates were prepared for transmission FTIR measurements. Due to the low relative amount of thiol with respect to the nano-sized gold core, it was hard to get a full range spectrum with reasonable signal/noise ratio. In addition, the spectra were somehow distorted by

the interference from the gold core and absorption of water from the atmosphere. Still a major difference between the spectra of the modified and unmodified particles can be seen, as shown in Figure 5.1.

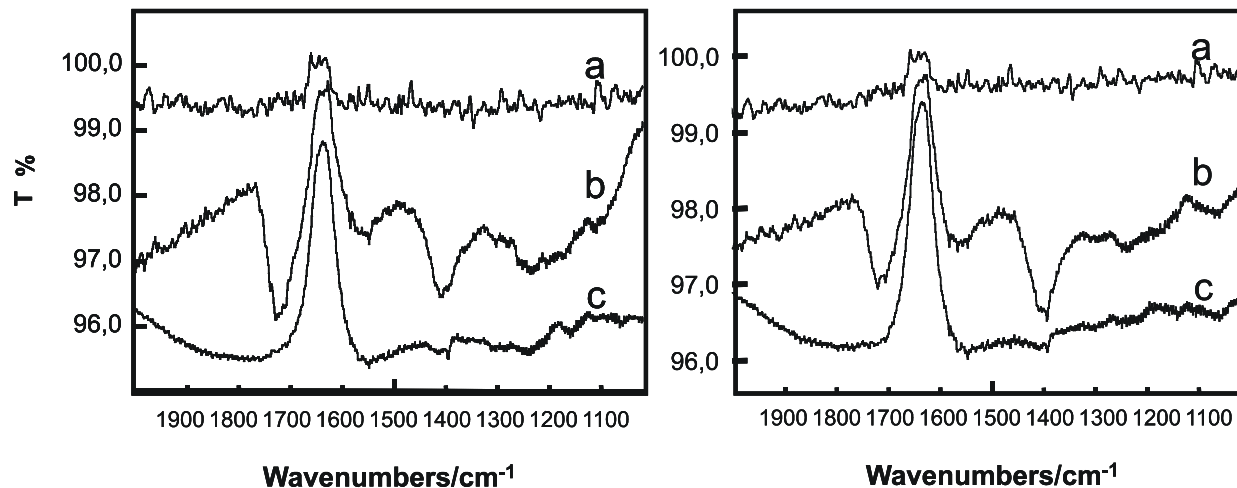


*Figure 5.1. FTIR spectra of gold nanoparticles precipitated by NaCl (left frame) and Na<sub>2</sub>SO<sub>4</sub> (right frame). a) a blank KBr pellet ; b) the MSA-modified gold nanoparticles; c) the unmodified gold nanoparticles.*

In both cases of the modified samples, i.e., precipitated by NaCl (curve b in the upper panel of Figure 5.1) and Na<sub>2</sub>SO<sub>4</sub> (curve b in the lower panel of Figure 5.1), respectively, characteristic bands, i.e., at around 1710cm<sup>-1</sup> for the stretching of C=O in the free -COOH and at around 1390cm<sup>-1</sup> for the symmetric stretching of COO<sup>-</sup> are clearly present, suggesting a very stable carboxylic group-carrying species (partially dissociated) on the modified gold particles. Another characteristic band, the antisymmetric stretching of COO<sup>-</sup>, ~1580cm<sup>-1</sup>, was buried in the negative peak in that region, which appear in the spectra for all samples, probably due to the interference from the water band. In comparison, no pronounced peaks can be found in the corresponding spectra (curves c in both panels) of the unmodified particles. This can be attributed to the fact that during the process of precipitation, water rinsing and re-dispersion, the physically adsorbed ions on the surface of the as prepared particles have been washed away. It can be concluded that chemical adsorption of MSA on the particle surface occurred, although the exact surface coverage remains undetermined.



### **Stability against pH change**

An interesting feature of the modified sample is its improved stability against changes in pH. This was investigated by a comparison between the suspension stability of the modified and unmodified particles against pH changes induced by HCl titration. In a 3.5 ml quartz cuvette, an appropriate amount of the as-prepared sample and the modified sample (both were dialyzed against milli-Q water to the same level of conductivity,  $120 \pm 10$  S/cm and pH,  $5.2 \pm 0.1$ ) was diluted to 2.7 ml with milli-Q water to get the same level of initial peak intensity in the in situ recorded UV-Vis spectra, respectively. Then 0.1 mol/l HCl in 100  $\mu$ l aliquots were added at an 1h interval. After each addition, optical absorption spectra were captured in cycles of 10min.

Figure 5.2.a and b, respectively, show the gradual change in the UV-Vis spectra of an unmodified and of a modified sample, respectively, upon each addition of HCl. From top to bottom, the spectra are displayed in groups of 6 spectra corresponding to each HCl addition. The absorption decrease due to dilution effects was not calibrated deliberately in order to avoid the overlap of the spectra. Absorption at wavelengths above 600 nm, which corresponds to the collective plasmon resonance of closely-spaced gold nanoparticles, can be used as an indication of particle flocculation in the dispersion.<sup>16</sup>

As can be seen from Figure 5.2.a for the unmodified sample, the spectral change was initiated even by the first addition of HCl and became more obvious after the 2<sup>nd</sup> addition. More drastic changes were found with the 5<sup>th</sup> addition, evidenced by the systematic increase of the absorption above 600 nm, suggesting that a gradual flocculation of primary particles was happening due to the change of pH and was accelerated at the lower pH. A pseudo-isosbestic point at around 580nm is clearly visible indicating that no precipitation happened during the course of the experiment, at least by the end of 5<sup>th</sup> addition. However, the 6<sup>th</sup> addition to this sample initiated a settlement of the flocculated particles from the suspension, indicated by a drastic drop down of the spectrum of the whole range approaching the baseline (not shown in the figure).

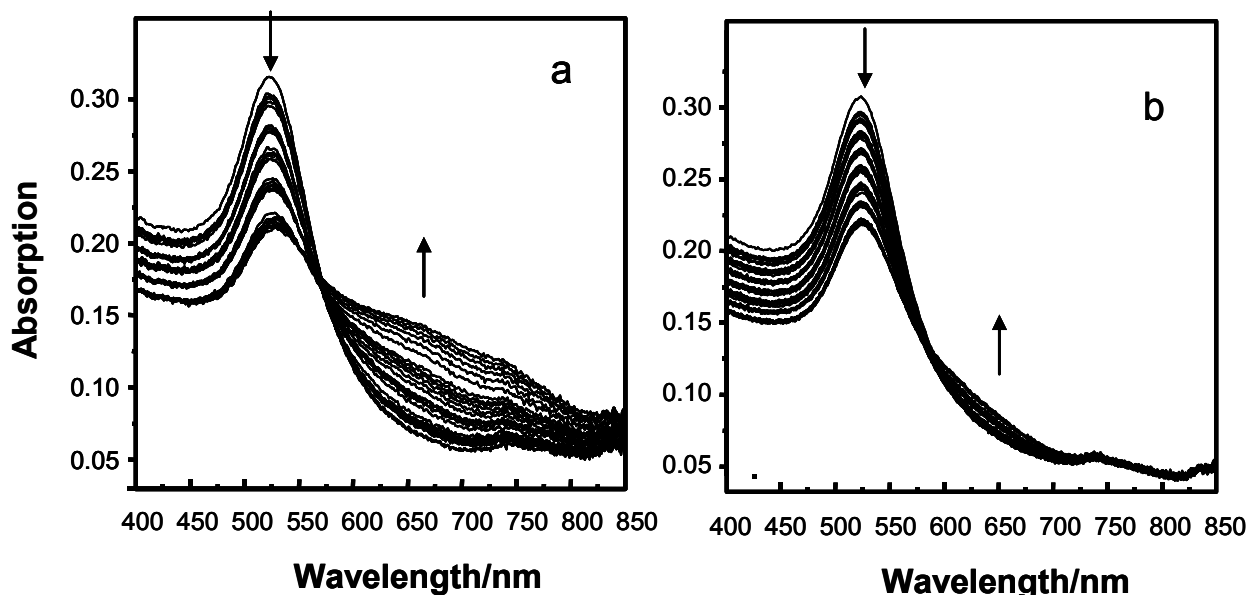


Figure 5.2. UV-Vis spectral changes upon HCl titration. a) the unmodified gold colloid; b) after MSA-modification. Both samples were dialyzed against milli-Q water for sufficient time with frequently changing water outside, to reach a same level of conductivity ( $120 \pm 10 \mu\text{S/cm}$ ) and pH ( $5.2 \pm 0.1$ ). From top to bottom, each group of spectra corresponds to the 0<sup>th</sup>, 1<sup>st</sup>, 2<sup>nd</sup>, ... addition of 0.1 mol/L HCl in 100  $\mu\text{L}$  portions.

A clear difference is found for the modified sample, as shown in Figure 5.2.b, in which only a slight spectral change above 600 nm was observed, mainly after the 6<sup>th</sup> and 7<sup>th</sup> addition, suggesting that the modified sample needs much more HCl to induce the same extent of flocculation as the unmodified one. Although this test was not followed further until the settlement happened due to the volume limit of the cuvette, the difference mentioned above is convincing enough to conclude that, under the same conditions, the modified sample has an improved stability against flocculation induced by pH change.

Such a difference in stability against flocculation might be a reflection of the difference in the electric double layer structure between the unmodified and modified particles, presumably attributed to the presence of adsorbed MSA on modified particles and/or free MSA in solution for the latter case. An electric double layer surrounding a charged particle consists of two parts, i.e., the inner shell of charge and the outer ionic atmosphere, which prevents particles from aggregation by electrostatic repulsions. It should be noted that citric acid and MSA have very similar first-step and second-step dissociation constants in solution, i.e.,  $\text{pK}_{\text{a}1}=3.13$ ,  $\text{pK}_{\text{a}2}=4.76$ ,  $\text{pK}_{\text{a}3}=6.40$  for citric

## **5. Gold nanoparticles and gold nanowires – surface modification and synthesis**

acid,<sup>17</sup> and  $pK_{a1}=3.30$ ,  $pK_{a2}=4.94$  for MSA,<sup>18</sup> respectively. As previously mentioned, after dialysis, both samples have identical pH ( $5.2\pm 0.1$ ) and conductivity ( $120\pm 10$   $\mu\text{S}/\text{cm}$ ). At this pH, the dissociation behavior of citric acid and MSA in solution would be similar, producing mainly bivalent citrate anions and bivalent MSA anions by the first-step and the second-step dissociation.

Assuming that a bivalent citrate anion and a bivalent MSA anion will contribute equally to the conductivity, the same value of conductivity implies that the total concentration of anions (from citrate and MSA, as well as  $\text{Cl}^-$  released from  $\text{AuCl}_4^-$  during reduction, and  $\text{OH}^-$ ) and counterions ( $\text{Na}^+$ ,  $\text{H}^+$ ) would be roughly the same, although the relative concentration of each species is slightly different between the modified and unmodified samples. This means there is no significant difference in the outer ionic atmosphere of the electric double layer of the modified and unmodified particles in the pH range from 5.2 to lower values upon HCl addition. However, some differences in the inner shell of charge of the electric double layer as well as their differences in response to the pH change could be expected, because the particles presumably got charged in different ways for the modified and unmodified samples, as discussed below.

For the unmodified citrate-reduced gold colloids, the particles were negatively charged by adsorbing ions from solutions, most likely remaining citrate and/or its oxidized intermediates.<sup>19, 20</sup> The exact bonding between citrate ions and gold surface is still uncertain, however, it is more likely a carboxylate coordination to a certain surface adsorbed gold ionic species but definitely not a covalent bonding to surface gold atoms. Therefore, by lowering the pH with the addition of HCl, neutralization of the adsorbed citrate ions will decrease the net charges on the particle surface, leading to less repulsion between the particles; on the other hand, with more HCl being introduced, depletion of adsorbed citrate ions is possible, either due to exchange by chlorine ions, or due to reduction of the coordination with the protonated citrate ions at lower pH. Altogether, these effects will contribute to a decrease of the electrostatic repulsion, leading to a faster flocculation of approaching particles.

In the case of the modified samples, the particles were negatively charged mainly by the dissociation of the carboxylic groups being covalently bound on the particle surface via the Au-S bonding. Although lowering the pH will also decrease the repulsion through neutralization by protonation, the desorptive processes in the inner shell of charge could be prevented, thus explaining slower flocculation.

It was reported that the dissociation coefficient (pK) of the carboxylic groups in ordered self-assembled monolayer on flat gold surface may be shifted to a higher value than that in solution.<sup>21</sup> If this is the case for the MSA monolayer adsorbed on the modified gold particles, the surface-bound MSA anions would get fully protonated at a higher pH than citrate, leading to a faster flocculation of modified sample compared to the unmodified one. Nevertheless, the experimentally observed decreased tendency for flocculation of the modified particles indicates that this process does not play the dominant role in the system studied here, suggesting that the major contribution might be attributed to the simultaneous desorptive process in the inner shell of charge.

The same titration test was performed on the sample pair (unmodified and modified) being dialyzed against a 0.1 % citrate solution, which gives both samples a final conductivity of  $830 \pm 10 \mu\text{S}/\text{cm}$  and a pH of  $7.4 \pm 0.1$ , the corresponding UV-Vis data are shown in Figure 5.3. In this case, the unmodified sample changed even faster than in the case of dialysis against water, obvious flocculation began with the 1<sup>st</sup> HCl addition and the settlement started at the beginning of the 3<sup>rd</sup>

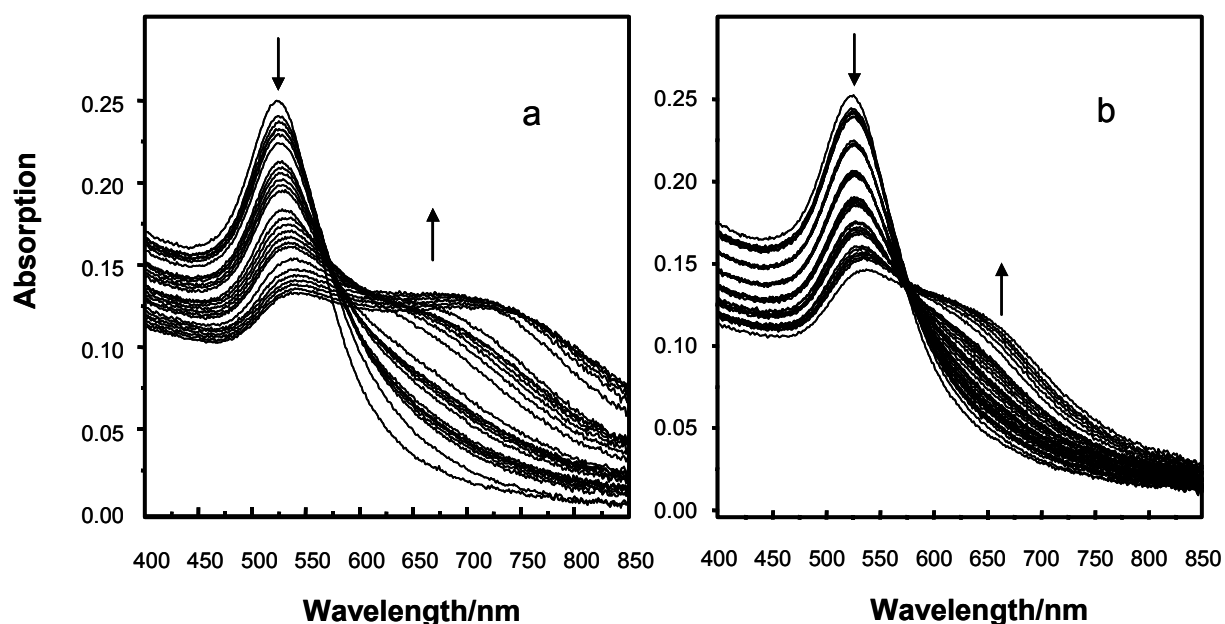
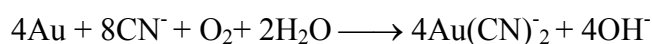


Figure 5.3. UV-Vis spectral changes upon HCl titration. a) the unmodified gold colloid; b) after MSA-modification. Both samples were dialyzed against a 0.1%  $\text{Na}_3\text{Citrate}$  solution for ~24 hrs with 2 times changing of solution outside, to reach a same level of conductivity ( $830 \pm 10 \mu\text{S}/\text{cm}$ ) and pH ( $7.4 \pm 0.1$ ). Spectra are displayed in the same way as in Figure 5.2.

addition. The modified sample also changed a slightly faster, obvious flocculation began with the 2<sup>nd</sup> and 3<sup>rd</sup> addition, and settlement started at the beginning of the 7<sup>th</sup> addition. This observation again supports the argument that the modified sample has improved stability compared to the unmodified one. It should be pointed out that dialysis against citrate gave a final conductivity ca. 7 times higher than that against water, suggesting a more compressed outer ionic atmosphere which will be less effective to prevent flocculation. That is why both the unmodified and modified samples show a faster change when dialyzed against citrate.

### **Stability against CN<sup>-</sup> etching**

It is known that cyanide can be used to dissolve atomic gold to form a gold-cyanide complex in the presence of oxygen, based on Elsner's equation:<sup>22</sup>



A self-assembled monolayer on a gold surface may prevent such kind of etching, depending on the thickness and packing density of the protecting layer.<sup>23,24</sup> In order to evaluate the influence of the chemically bound MSA on the modified gold nanoparticles against cyanide etching, comparative tests were conducted on both the unmodified and modified samples, by in-situ monitoring of the etching of surface-bound particles by SPR spectroscopy.

Gold nanoparticles were deposited from a suspension onto evaporated gold substrates pre-modified with a self-assembled monolayer of 3-mercaptopropionic acid and alternating bilayers of polyelectrolytes (4 layers of polyallylamine and 3 layers of polystyrenesulfonate) following a procedure described in Chapter 3.2. The polyelectrolyte bilayers (total thickness ca. 17 nm) were used to protect the evaporated gold from being etched by the cyanide. The deposition was facilitated by the electrostatic interaction between the negatively charged gold nanoparticles and the positively charged polyallylamine top-layer. Figure 5.4.a shows the deposition kinetics of both the modified and unmodified particles which were obtained by monitoring the shift of the minimum reflectivity angle of the surface plasmon resonance. For the deposition of particles, suspensions of the modified or unmodified samples were injected into the fluid cell. The deposition was terminated after a certain angle shift was reached, by replenishing the fluid cell with milli-Q water. The same final angle of resonance was

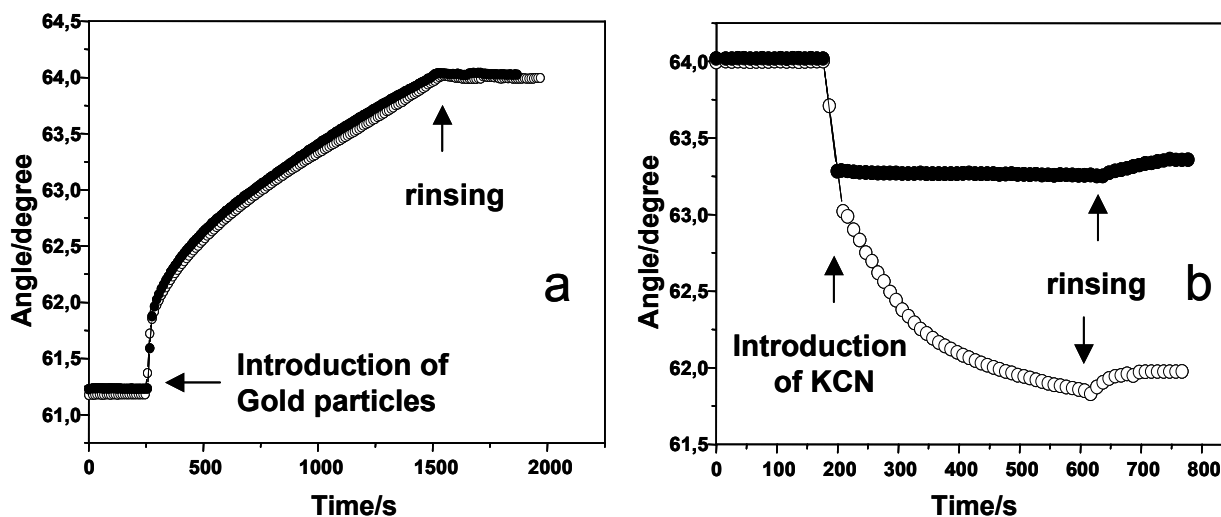
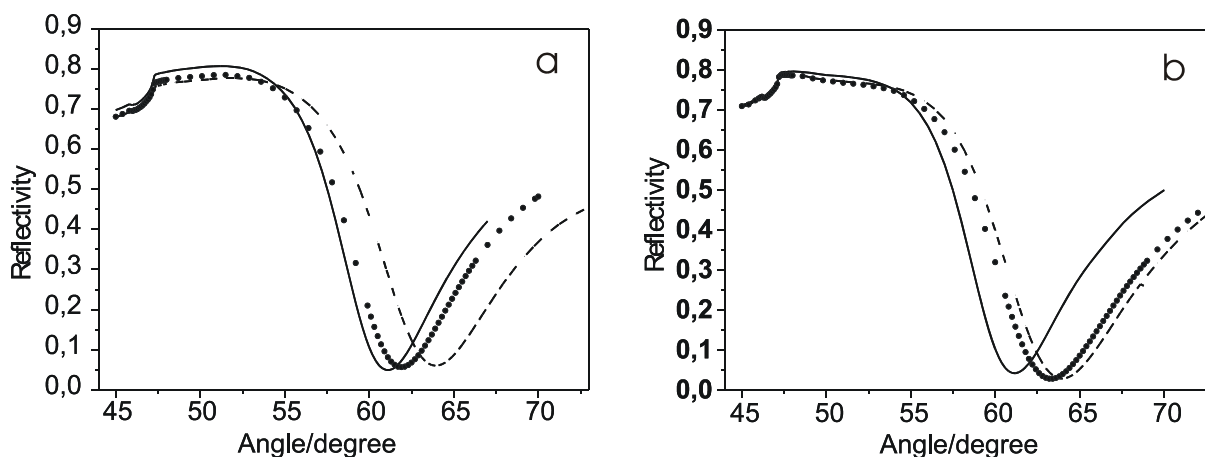


Figure 5.4. Kinetic curves of the deposition (a) and the etching (b) of the gold nanoparticles on polyelectrolyte bilayers obtained by following the resonance angle of the surface plasmon (being roughly proportional to the amount of adsorbed gold) against time. The data points for the unmodified gold colloid are shown as empty circles, and that of modified gold nanoparticles are shown as filled circles.

chosen for the modified and unmodified particles in order to ensure an almost identical number of particles on the surface since the particle size is the same. Subsequently the fluid cell was rinsed thoroughly with milli-Q water in order to remove any excess of electrolyte and particles not bound to the surface.

The etching was performed by injecting a 1.5 mmol/l KCN in water solution into the fluid cell and keeping it for the same period of time on both samples. The kinetics of the process of cyanide dissolution is shown in Figure 5.4.b. After introducing the cyanide solution into the flow cell a rapid decrease of the angle of resonance was observed. The reason for that effect, characteristic for both modified and unmodified particles is not absolutely clear. A possible explanation could be that the cyanide first causes separation of weakly bound particles from the surface and then the real etching process starts. Following the kinetic curves further, a slower process sets in for both samples, which is interpreted as the etching process, the time constant for this process being very different for the two samples. It can be clearly seen that the unmodified particles were almost completely dissolved in about 10 minutes (open circles). In comparison the modified particles exhibited much better stability against etching. The angle of resonance remained almost

unchanged for the same period of time (filled circles).



*Figure 5.5. Changes in SPR curves due to deposition of gold nanoparticles and cyanide etching thereafter. (a) The MSA-modified sample, and (b) the unmodified gold colloid. Solid lines: before particle deposition; Dashed lines: after deposition; Dotted lines: after etching.*

Figure 5.5. shows the SPR resonance before and after deposition of particles (solid and dashed lines, respectively), as well as after the etching process (dotted lines). For the unmodified particles the resonance (Figure 5.5.a) shifts back almost to its original position before deposition, suggesting the particles were nearly completely consumed by cyanide etching during the course of the experiment.

Another interesting effect is that after the deposition of gold particles the width of the plasmon resonance expands due to the contribution of the imaginary part of the refractive index of gold nanoparticles attached to the surface. After etching, the width of reflectivity curve is comparable with that measured before the deposition of particles, supporting the interpretation of the removal of the adsorbed gold colloids but no change in the supporting layer structure.

In contrast, the modified particles (Figure 5.5.b) are much more stable against cyanide etching, suggested by only a slight shift back of the resonance. Similarly to the case of the unmodified particles, an increase of the width of the resonance upon adsorption is observed. The scan after etching (dotted curve) shows a very similar width indicating that the particles remain on the

surface. The slight shift back is interpreted as being due to the rapid process immediately after the introduction of cyanide into the flow cell and not to the dissolution of gold particles.

Taking all the above observations together, it is reasonable to conclude that the adsorbed MSA has a quite high surface coverage, possibly similar to a self-assembled monolayer.

### **Influence on the seeded growth**

A well-known autocatalytic effect, i.e., the chemical reduction of gold chloride with certain reducing agents promoted by the atomic gold surface,<sup>25</sup> was further employed to probe the difference between unmodified and modified samples. It was reported that the citrate-reduced gold particles can be enlarged by exposing them either to H<sub>AuCl</sub><sub>4</sub> at 70° C<sup>26</sup> or to a mixture of H<sub>AuCl</sub><sub>4</sub> and NH<sub>2</sub>OH.<sup>27</sup> Reduction of H<sub>AuCl</sub><sub>4</sub> by citrate ions on the surface of the citrate-reduced gold nanoparticles was also observed at room temperature.<sup>28</sup> In these cases, no new particle nucleation occurs in solution, and all added H<sub>AuCl</sub><sub>4</sub> goes into the growth of the existing particles, by surface-catalyzed reduction with the citrate ions remaining in seeds solution or the added NH<sub>2</sub>OH, respectively. Actually, such an idea has been developed into a common approach to production of larger gold nanospheres<sup>27, 28, 29, 30, 31</sup> and nanorods<sup>32, 33</sup> by using the small citrate-reduced gold particles as seeds, although a general mechanism for particle growth has not been fully clarified. In the beginning, it was speculated that the modified particles would not be growing at all due to the protection of their surface by the MSA monolayer. To our surprise, both samples seem to have similar trends of size changes upon mixing with a solution of H<sub>AuCl</sub><sub>4</sub> (with a final concentration of 0.01% w/v) and when NH<sub>2</sub>OH was added later, as indicated by the change of the position and intensity of UV-Vis band around 530nm due to the plasmon resonance absorption of nanometer sized gold particles (data not shown), suggesting the growth of particles in both cases with or without NH<sub>2</sub>OH.



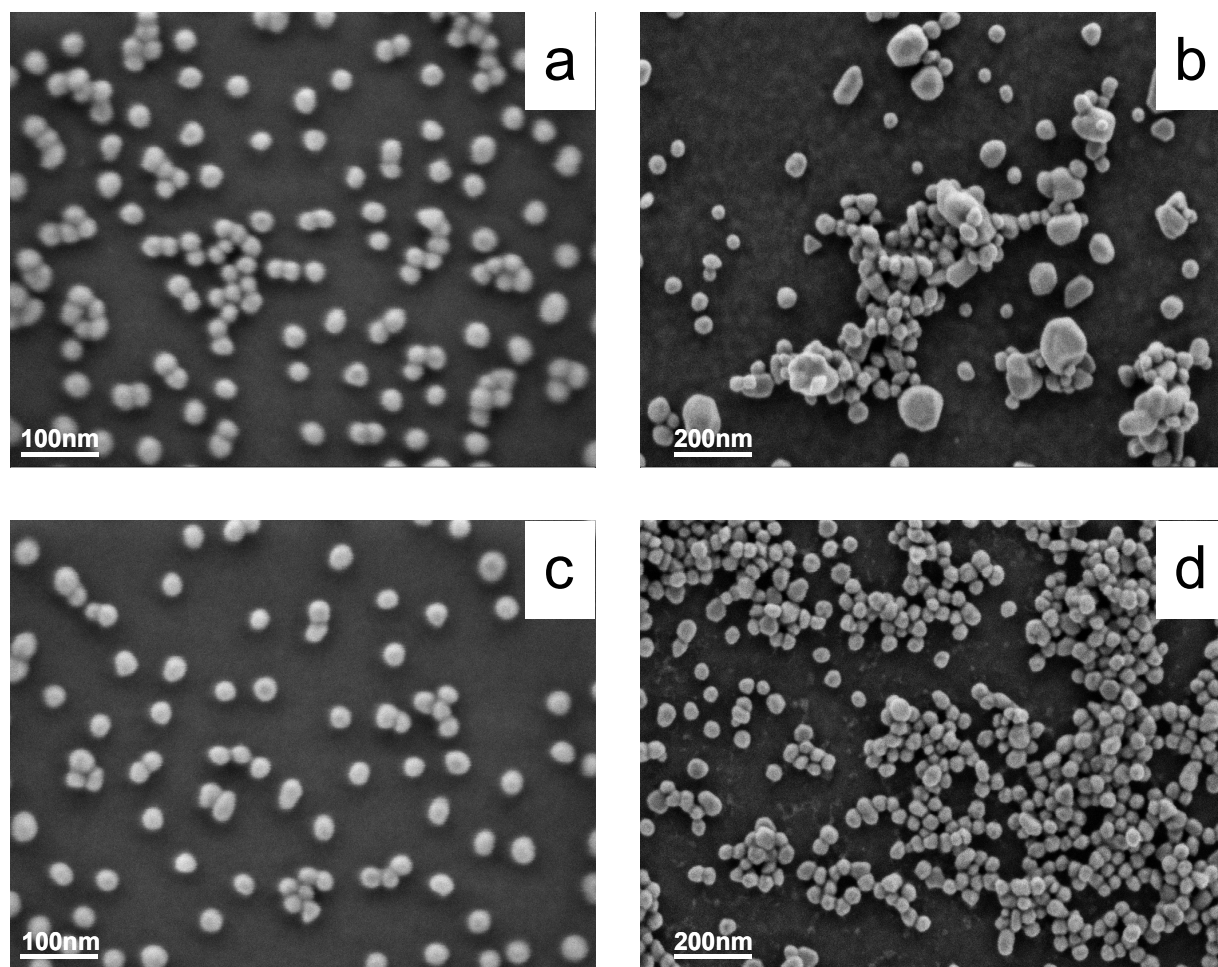


Figure 5.6. SEM images of the unmodified and modified particles, before and after the growing treatment in solution. a) unmodified particles before growing; b) unmodified particles after growing; c) modified particles before growing; d) modified particles after growing.

The growth of both unmodified and modified particles was confirmed by scanning electron microscopic images, given in Figure 5.6., with a and b showing the unmodified particles, c and d showing the modified particles, before and after growing treatment with  $\text{HAuCl}_4$  in the absence of  $\text{NH}_2\text{OH}$ , respectively. To be comparable, the growing treatment was performed by injecting the same volume of dialyzed modified or unmodified particle solutions into the same volume of 0.01% (w/v)  $\text{HAuCl}_4$  solution, left for ca. 24 hr. The same mean size of ca. 20 nm can be determined from Figure 6a and 6c for the unmodified and modified particles, respectively, suggesting that there was no size change of the gold nanoparticles during the surface modification.

## **5. Gold nanoparticles and gold nanowires – surface modification and synthesis**

As can be deduced from Figure 5.6.b and 5.6.d, however, after the growing treatment, unmodified and modified particle populations show a distinctly different size distribution, both with the increased average size of particles.

The modified particles grew, but very regularly, without a significant diversity of particle size and shape. In contrast, the unmodified particles grew to a very broad size distribution with irregular particle shapes. It should be noted that no smaller particles than the original size could be found in both samples after the growing treatment, suggesting that reduction of gold chloride was mainly confined to the surface of existing seed particles.

The growth of a gold seed in the growing solution can be considered as a competition between the surface-assisted chemical reduction and the simultaneous ligand capping on surface of particles. The relative rates of the capping-decapping and the relative reduction rates on the different facets will regulate the final shape of particles.<sup>34</sup> In both solutions of the unmodified and modified samples, although both were dialyzed to a low level of conductivity as mentioned above, there are still some residual citrate ions and even MSA for the latter, which may serve either as the reducing agent for the particle growth or as the capping agent retarding the growth in the presence of gold chloride.

In the case of unmodified samples, irregular shapes grown from the unmodified seeds can presumably be attributed to the physically adsorbed citrate capping the particle surface, which may be heterogeneous in packing density and thickness, therefore being less robust for preventing the preferential growth from the “active sites or facets” on particular particles at the early stage and during the successive growth. The deteriorated size distribution also implies that the growth of unmodified particles did not start at the same time, and/or did not proceed with the same speeds, on different existing particles, suggesting that the citrate capping layer on unmodified particles may also differ from one to another. Irregular growth could become more remarkable when citrate concentration was low, as suggested by the findings of Turkevich et al. that the low citrate concentration leads to irregular shaped particles while "normal concentration" leads to round ones.<sup>26</sup>

For the modified samples after growth, absence of any irregularly shaped particles indicates that there was no preferential growing during the whole process of growth, especially at the early stage, suggesting that the MSA monolayer on modified gold particles might be homogeneous and

## **5. Gold nanoparticles and gold nanowires – surface modification and synthesis**

defect-free. The question why the MSA monolayer could not have protected the modified particles from growing can be answered according to the fact that MSA, which has a similar chemical structure as citrate, can reduce  $\text{HAuCl}_4$  at room temperature in solution. When mixed with gold chloride, surface-assisted reduction of the supplied  $\text{HAuCl}_4$  by MSA adsorbed on the modified particles could occur, enabling the deposition of the first layer(s) of gold atoms onto the seeds surface which will mediate the further particle growth through successive surface reduction with citrate and/or MSA in the solution. In contrast to the uncertain structure of the citrate capping layer on unmodified particles, the MSA monolayer on modified particles is more homogeneous in packing density and thickness, and is identical particle to particle. Therefore, all the modified particles and the surface sites on each particle can be roughly considered to have equal growing speed during the whole enlargement process. Therefore, all the modified particles and the surface sites on each particle can be roughly considered to have equal opportunity to initiate the surface reduction at the same time in the beginning, which is a prerequisite for the later on homogeneous growth to a regular shape and a narrow size distribution.

The sustained size distribution of the modified particles implies that the growth of modified particles not only started roughly at the same time but also proceeded synchronously at different surface sites on different existing particles. In contrast to the unmodified case, further growth of the modified particles proceeds in the presence of a considerable amount of free MSA in solution in addition to citrate, through a different yet unclear mechanism. Considering the different growth behaviors observed in the present study, preliminarily, we suppose that MSA in solution is responsible for the homogenous nature of the successive growth of the modified particles, providing a stable and homogenous surface chemistry of the particles during the whole reaction time.

It is noted that MSA is a stronger capping agent than citrate for gold, facilitating more uniform and robust capping in competition with the surface-assisted reduction for growth, which is favorable for suppressing the difference in surface reduction rates on different facets of a particular particle and/or on different particles.

Taking the two cases together, it can be concluded that the modified and unmodified particles might behave in different ways not only at the early stage for initiating the growth, i.e., the deposition of the first layer(s) of newly reduced gold atoms, but also in the later on whole course of

growing. The presence of MSA adsorbed on modified particles and in solution played important roles in regulating the size distribution and the particle shape at different stage of growth. However, further efforts should be made in order to clarify the seeding growth mechanism of MSA capped gold particles, by studying the capping-decapping kinetics of MSA in the absence and presence of citrate at different concentration ratios, and by probing the surface structure of particles at various stage of growing.

### **5.1.4. Conclusion**

Surface modification of citrate-reduced gold nanoparticles by MSA was carried out in aqueous phase. This provides a way to obtain stable gold nanoparticles with a diameter of around 20 nm functionalised with surface carboxylic groups. The direct comparison with the (unmodified) citrate-reduced gold colloids demonstrated that the modified nanoparticles exhibit an improved stability against pH changes and cyanide etching.

## **5.2. Synthesis of monolayer protected gold nanoparticles**

### **5.2.1. Introduction**

Among the number of thiol derivatives with different chain length and functional groups that were used in the synthesis and in surface modification of gold nanoparticles is 2-mercaptosuccinic acid (MSA). Up to now MSA was studied as a capping agent for gold nanoparticles synthesized using the citrate reduction method.<sup>35</sup> In 1999 Chen and Kimura<sup>8</sup> used MSA in the presence of NaBH<sub>4</sub> as reduction agent for HAuCl<sub>4</sub>. The synthesis was carried out in methanol and resulted in gold particles with a size from 1 to 3.6 nm depending on the ratio HAuCl<sub>4</sub>/MSA. In a recent work Negishi and Tsukuda<sup>36</sup> demonstrated the use of dimercaptosuccinic acid (DMSA) and MSA as a reducing and capping agent for the synthesis of small (size 1 – 3 nm) gold nanoparticles in water at room temperature.

Here 2-mercaptosuccinic acid as a reducing agent for hydrogen tetrachloroaurate is employed as well, and syntheses are carried out at boiling temperature in aqueous medium. The

scope of the presented study is to identify the molar ratios between  $\text{HAuCl}_4$  and MSA which yield gold nanoparticles. The size distribution of the particles is investigated as well as their chemical surface structure and the stability of the resulting colloidal solutions. Implications of these results on the mechanism of particles formation are discussed

### **5.2.2. Materials and methods**

All reagents used in this section were the same as in section 5.1. Substrates for SEM imaging and samples for FTIR were prepared as in section 5.1. The particles size was determined from the gray scale bitmaps by a commercial software “Scion image 4.0.2 Beta” (Scion Corporation). This software counts and measures features of interest. First a threshold is determined automatically to discriminate objects of interest from surrounding background based on their gray values. Connected groups of pixels above threshold are fitted as ellipsoids with major and minor axis. The particle size was defined as the average of both axes.

The synthetic procedure was as follows:

100 ml 0.01% solution of  $\text{HAuCl}_4$  in Milli-Q water were heated to boiling temperature in a 250 ml, two neck, round bottom flask equipped with a reverse condenser. The solution was stirred at 700 rpm using a magnet stirrer. The molar ratio between  $\text{HAuCl}_4$  and MSA is adjusted by adding the appropriate amount of (for example 12.5 ml in the case of a molar ratio 10:5)  $10^{-3}$  mol/l aqueous solution of MSA, pre-neutralized by a stoichiometric amount of NaOH, with a burette (25 ml) to the boiling solution. The reaction is fast and for the molar ratios where small particles are formed (see below), the color of the reaction mixture changes in about 30 s from pale yellow through colorless and purple to red, which is a typical color for colloidal solutions of gold nanoparticles a with size larger than 10 nanometers.

### **5.2.3. Results and discussion**

UV-vis spectra of the resulting reaction mixtures for different molar ratios  $\text{HAuCl}_4$  : MSA are shown in fig. 5.7. In the following the molar ratios  $\text{HAuCl}_4$  : MSA will be referred as relative concentration (in percent) of MSA to  $\text{HAuCl}_4$ . An absorption peak at about  $\lambda = 525$  nm is visible in

the spectra with relative concentration of MSA between 50 % and 100 %. The peak maximum almost does not shift but its intensity is decreasing with increasing molar portion of MSA. The peak almost vanishes in the spectrum with a relative concentration of 110 %. A shift to increasingly longer wavelengths is observed when the MSA concentration is reduced below 40 %. A very weak absorption in the range of 500 nm – 800 nm is measured at MSA concentration of 10 %.

The maximum at about 300 nm, which is present in the spectrum of pure  $\text{HAuCl}_4$ , is also seen in the spectra of the reaction mixtures with relative MSA concentrations of 30, 20 and 10 %. In the spectrum with a relative MSA concentration of 110 % the absence of a plasmon resonance band implies that no particles were formed or the particles are very small (particles with a size of 1-2 nm do not show a plasmon resonance).<sup>37</sup>

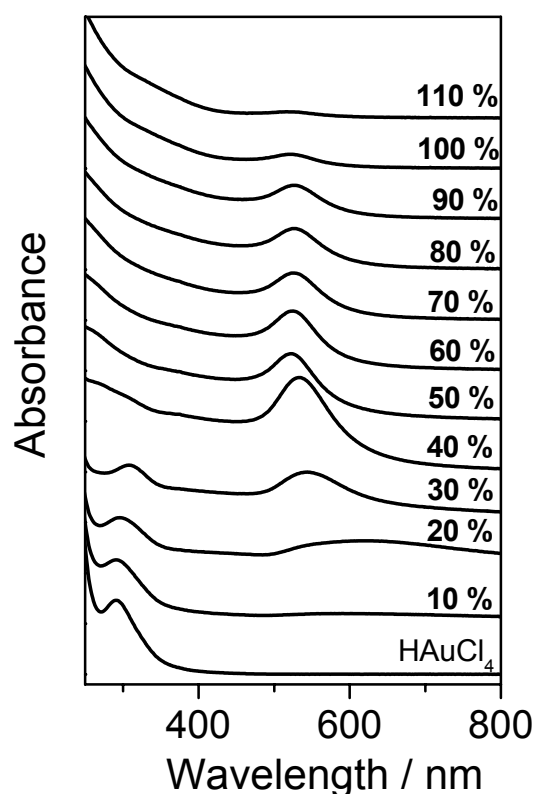


Figure 5.7. UV-Vis spectra of solutions containing gold nanoparticles obtained using different relative concentrations of MSA. The spectra are offset for clarity. The spectrum of pure  $\text{HAuCl}_4$  is shown for comparison.

The peak at  $\lambda = 525$  nm for samples with a relative concentration of MSA between 50 and 100 percent is indicative for the presence of isolated gold nanoparticles with size between 10 and

50 nm.<sup>38, 39, 40</sup> The absorption maximum almost does not change but the intensity decreases, which suggests that the increase of the relative concentration of the MSA leads to a decrease of the amount of Au(0) in particles with radii above 5 nm since the extinction is proportional the amount of gold in the solution.<sup>5, 6</sup> One possible explanation is that the increased concentration of MSA involves more H<sub>2</sub>AuCl<sub>4</sub> in complexation reactions.

The observed red shift in the absorption maximum when the relative concentration of MSA is reduced to 40 % and less suggests the presence of larger particles in the solution. Irregularly shaped particles or particle aggregates would lead to similar effect but this can be excluded from the SEM investigations discussed below.

From the peak intensity at  $\lambda = 300$  nm it can be deduced that for MSA concentrations

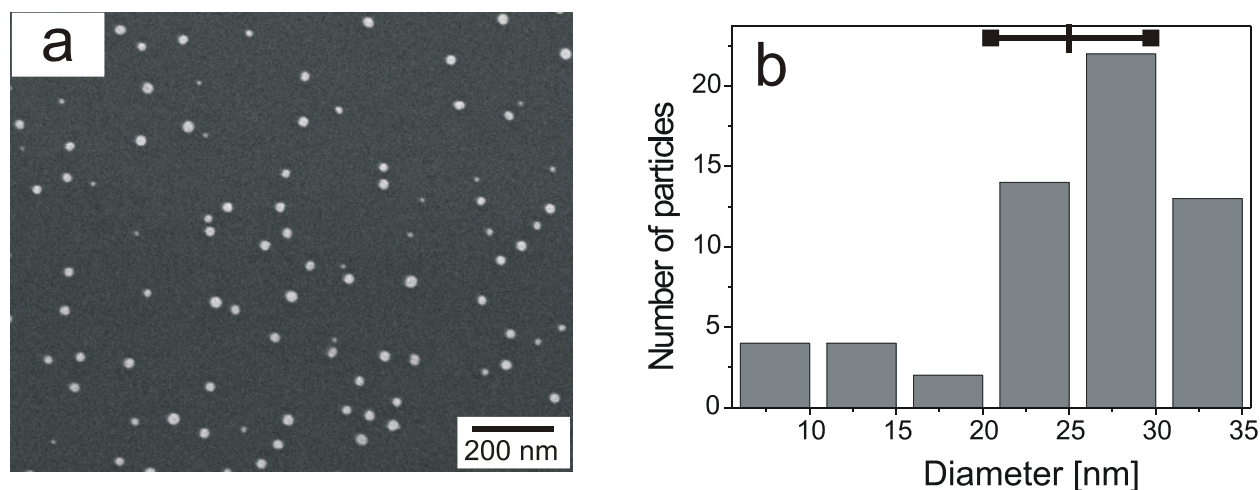


Figure 5.8. (a) SEM image of gold nanoparticles synthesized using a relative MSA concentration of 100%. (b) The corresponding size distribution.

below 30 % the amount of MSA is not sufficient to reduce all H<sub>2</sub>AuCl<sub>4</sub>, leaving free H<sub>2</sub>AuCl<sub>4</sub> in solution. In addition the amount of MSA may be insufficient for a complete coverage of the surface.

The size and morphology of the synthesized particles was investigated by SEM. Gold nanoparticles obtained with a relative MSA concentration of 100 % are shown in fig. 5.8. The particles appear close to spherical with an average size of 24.6 nm and a relatively broad size distribution (average deviation of the mean size of 5.1 nm).

Fig. 5.9. shows the calculated average size and average deviation as a function of the

relative concentration of MSA between 40 % and 100 %, the range of concentrations where stable gold particles were formed

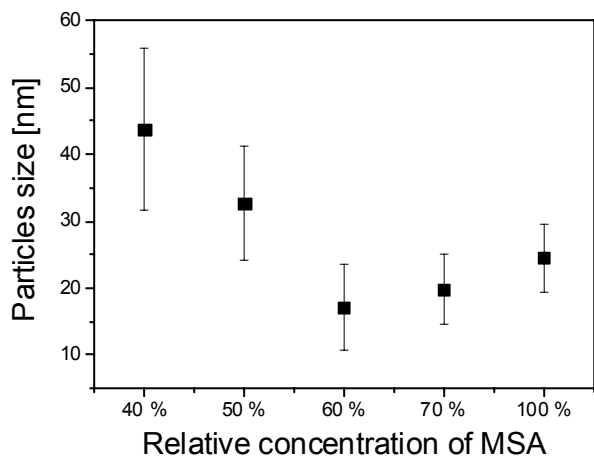


*Figure 5.9. Mean size of the particles with the corresponding average deviation as a function of the relative concentration of MSA.*

As a trend it could be deduced that increasing the molar portion of MSA leads to the formation of smaller particles. Generalizing, the size distribution is rather large but the size of the produced particles can be adjusted between 45 nm and 17 nm simply by varying the molar ratio of  $\text{HAuCl}_4$  to MSA.

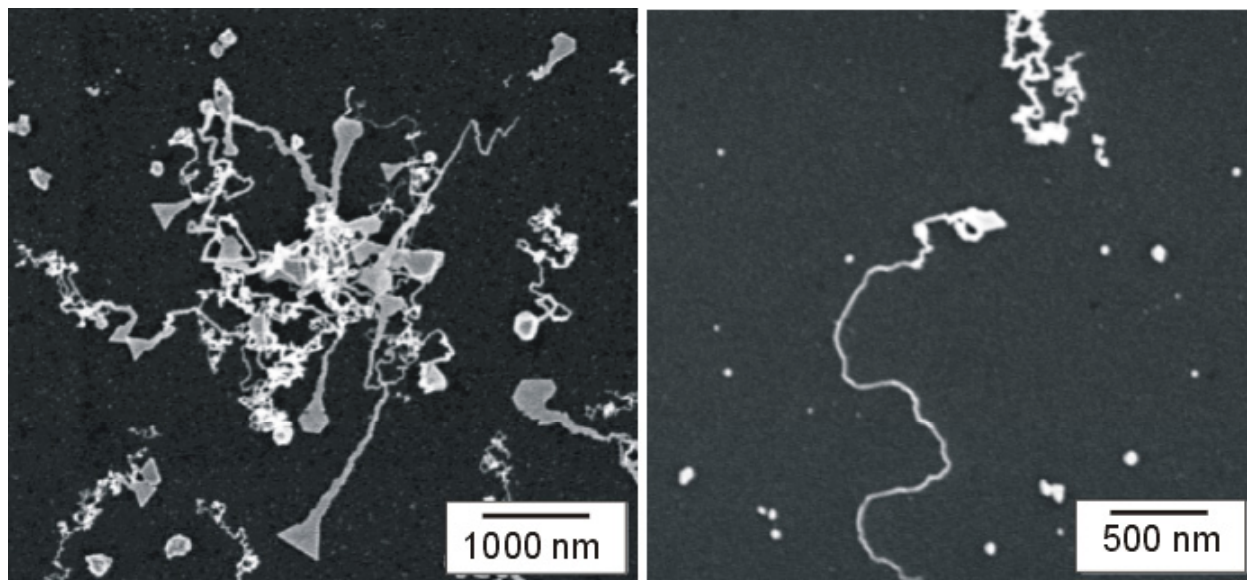


*Figure 5.10. SEM images of gold nanowires obtained using a relative MSA concentration of 10%.*

One interesting phenomenon was found for a MSA concentration of 10 %. In this case gold



nanowires as well as a number of small particles are formed as shown in fig. 5.10. The average cross section of a single wire is 15 nm and the length is typically in the range of micrometers. More details about the synthesis, structure and morphology of the gold nanowires will be given in section 5.3.

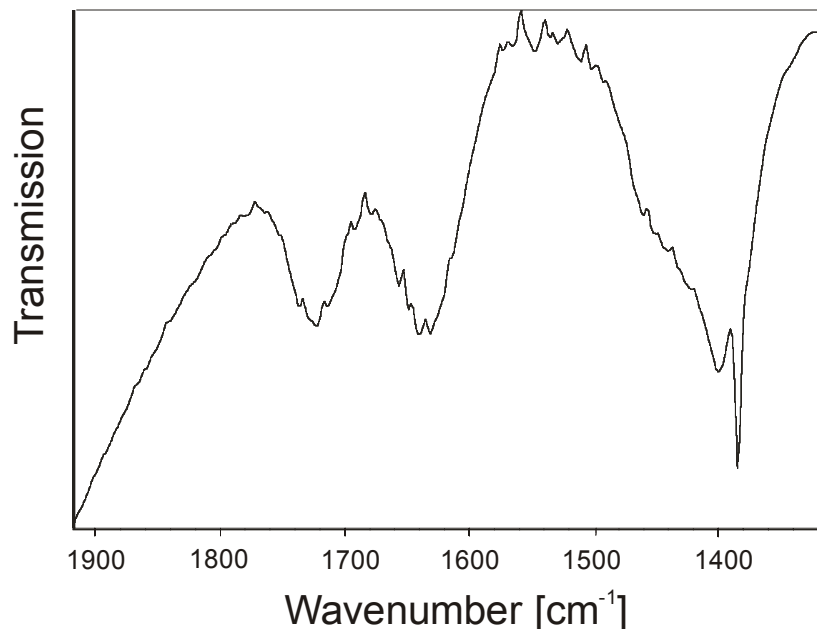
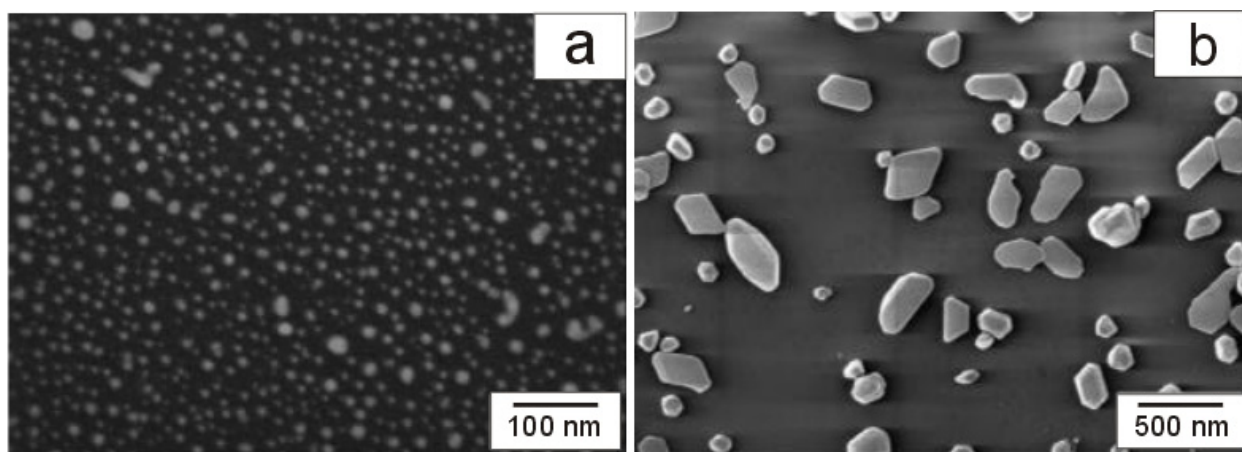


Figure 5.11. FTIR spectrum of a solid precipitate of the particles dispersed in a KBr pellet.

FTIR was measured in order to reveal the chemical surface structure of the gold nanoparticles. The spectrum is shown in fig. 5.11. The IR spectrum exhibits clear peaks at around  $1710\text{ cm}^{-1}$  for the stretching of C=O in the free  $\text{-COOH}$  and at around  $1390\text{ cm}^{-1}$  for the symmetric stretching of  $\text{COO}^-$ , suggesting a stable carboxylic group-carrying species (partially dissociated) on the surface of the gold particles.<sup>41, 1</sup> This observation correlates well with the findings of Negishi and Tsukuda<sup>3</sup>, and Chen and Kimura.<sup>2</sup> Most likely the surface of the particles is covered by products of the reaction. These are disulfide species, which carry carboxylic functional groups.<sup>42</sup> They are bound to the surface of the particles by a covalent Au-S bond owing to the well known Au-S chemistry. It might be possible that also other species as Au-MSA complex and unreacted MSA molecules are deposited on the surface of the particles. The fact that the surface of the particles is negatively charged is supported by the possible electrostatic deposition on a silicon wafer modified by 3-APTES. A substrate modified in such fashion carries amino groups on its surface and is positively charged in water.



*Figure 5.12. Particles synthesized with a relative MSA concentration of 20 % immediately after synthesis (a) and after 1 month (b).*

A stability study was conducted on the gold nanoparticles obtained by this method. An aging effect was observed at the sample synthesized with a relative concentration of 20 % MSA. The particles shown in fig. 5.12.a are deposited on a silicon wafer approximately 5 hours after synthesis. The diameter of most of the particles is below 10 nm but also some larger particles with a size of about 25 nm can be seen. The solution was sealed and left at ambient conditions. The color of the as prepared solution was dark gray. It was noticed that with time the color of the solution changed tending to pale brown-red as the solution became more turbid with some precipitations, which could be redispersed by shaking. After one month particles from the solution were deposited on a silicon wafer and imaged again. It can be seen in fig 5.12.b that the particles have grown as the size of most of them exceeds 200 nm. It seems the big crystals are grown bigger at expense of the smaller particles. Another inspection after 6 months showed that the size of the particles remains unchanged. This effect does not occur when the relative concentration of MSA is 40 % or higher. The colloidal solutions for these ratios keep their color with time and no visible precipitation is observed. The effect of aging correlates well with afore-mentioned that when the relative concentration of MSA is 30 % or below, it is not sufficient for a complete surface coverage of the particles. In addition the leftover  $\text{HAuCl}_4$  might contribute to this slow process of growing. It is possible that active centers existing on the surface lead to coalescence of the particles. Since in the process of coalescence the surface area is reduced, at a certain moment the amount of capping agent in the solution is sufficient for a complete coverage of the surface of the particles. The exact

kinetic of the aging phenomenon has not been studied. It is possible that particles first form aggregates and then merge in homogeneous crystal. This is an interesting point, which deserves attention in the future.

It is known that MSA can serve as a reducing agent for  $\text{HAuCl}_4$ .<sup>9, 43</sup> It was found that MSA reduces Au(III) to Au (I) with oxidative formation of disulfide species and complexation of Au(I) with the remaining MSA. Also, MSA at particular ratios can reduce Au(III) to Au(0) with the formation of small gold nanoparticles with a size of 2-3 nm as demonstrated by Negishi and Tsukuda.<sup>3</sup> In that case the reaction is carried out at ambient temperature and in aqueous medium.

For our case this implies that probably first complexation of the reduced Au(I) ions with MSA occurs and as a next step reduction to Au(0). It is likely that the complex formed, which has oligomeric<sup>9, 10</sup> character aggregates into small nuclei and afterwards the Au(III) reduced to Au atoms contributes to the growth of the nuclei.

The rather large size distribution suggests that nucleation occurs during the whole course of the reaction. The nuclei which are formed at an early stage of the reaction will grow larger in comparison to those formed at later stage due to the complete consumption of the  $\text{HAuCl}_4$  or the reduction agent (MSA).

The molar ratio between  $\text{HAuCl}_4$  and MSA plays an important role on the size of the produced particles. If the concentration of MSA is below 30 %, this leads to an incomplete surface coverage. The latter causes an aging effects and the formation of nanowires observed from MSA concentration of 20 % and 10 %, respectively. On the other hand when the MSA concentration is above 100 % the processes of complexation between MSA and Au(I) dominates and no particles are formed.

### **5.2.4. Conclusion**

In conclusion, it was demonstrated that monolayer protected gold nanoparticles with a diameter exceeding 10 nm can be synthesized by a simple one-step reaction in aqueous medium, involving MSA as both reduction and capping agent. It is believed based on the well established Au-thiol chemistry that a portion of MSA couples on the surface of the particles providing carboxylic functionalities. It was also demonstrated that the size of the particles depends on the

relative concentration of MSA used in the synthesis. For MSA concentrations of 110 % and higher, no particles were found in the reaction mixture and below MSA concentrations of 30 % the gold sols are unstable. In the latter case the concentration of MSA is too low, hence the surface coverage of the particles is not complete, which leads to aging effects of the resulting colloidal solutions. This from itself leads to some unusual effects like the formation of crystalline gold objects with curious shapes. This new route of synthesis also provides the possibility of formation of gold nanowires, which may open new prospective in nanoengineering as wiring of electric circuits at the nanoscale. Monolayer protected gold nanoparticles synthesised by this simple new route could be interesting in applications as cell imaging, DNA labels, catalysts or optical sensors, applications where narrow size distribution is not required.

### **5.3. A simple, one step synthesis of gold nanowires in aqueous solution**

#### **5.3.1. Introduction**

Considerable effort has been concentrated on the structuring of material at the nanometer scale. These activities were motivated on the one hand by the expectation that the classical "top down" strategies in microelectronics will have to be complemented by a "bottom up" to further decrease feature sizes. On the other hand, structure at the nanometer scale can drastically alter material properties, which beyond being interesting from a fundamental point of view, opens the way to tailor superior materials for application<sup>44, 45, 46, 47</sup>. An important structure are metallic wires with diameters in the range of a few nanometers<sup>48</sup>, being necessary in any electronic circuit in future nano-devices. Here, particularly gold and silver play an important role due to their high electrical conductivity and chemical inertness. Gold nanorods with aspect ratio up to 20 have been synthesized in solution<sup>32, 33, 49</sup> while various templating strategies had to be employed to obtain gold nanowires with higher aspect ratio. Wire formation on lithographically prepared templates,<sup>50, 51, 52</sup> in organic and inorganic nanoporous media,<sup>48, 49, 53, 54</sup> in cylindrical core-shell polymer brushes and on DNA,<sup>55, 56</sup> and by organizing gold nanoparticles in 1D arrays<sup>57, 58</sup> were reported.

Xia et al<sup>59, 60</sup> have demonstrated the synthesis of silver and lead nanowires by a high-yield solution-phase method, leading to nanowires with typical diameters of 30-40 nm and lengths up to 50  $\mu\text{m}$ . They pointed out that a simple one-step solution-phase approach offers high flexibility together with cost-effectiveness for future applications.

In this chapter a simple solution-phase synthesis yielding gold nanowires with no apparent upper limit in length is described. Hydrogen tetrachloroaurate ( $\text{HAuCl}_4$ ) and 2-mercaptosuccinic acid (MSA) as reducing agent reacted in aqueous solution with no additional capping agent being required.

### **5.3.2. Experimental**

*Materials:* All materials and cleaning procedures were as in the previous sections (5.1 and 5.2)

*Synthesis:* 100 ml of a 0.01 wt. % solution of  $\text{HAuCl}_4$  in Milli-Q water are heated to 100  $^\circ\text{C}$  in a 250 ml, round bottom, two-neck flask equipped with a coiled condenser. 2.5 ml  $10^{-3}$  mol/l aqueous solution of MSA are pre-neutralized by a stoichiometric amount of NaOH and added by a burette of 25 ml to the boiling solution, leading to a molar ratio of 10 to 1 between  $\text{HAuCl}_4$  and MSA. The reaction mixture is stirred at 700 rpm. Its colour changes from pale yellow before to colourless/greyish after the addition of MSA within a time period of 10 min. The mixture is kept at boiling temperature and stirred for 10 more minutes and then gradually cooled down to ambient temperature.

*Microscopy:* The SEM images were recorded by a LEO 1500 field-emission scanning electron microscope (LEO Electron Microscopy Ltd). TEM was measured by a LEO EM912 Omega electron microscope (LEO Electron Microscopy Ltd). The AFM images were recorded in tapping mode by a Digital Instruments Nanoscope III Multimode (Veeco).

### 5.3.3. Results and discussion

In order to investigate the morphology of the reaction product, a silicon wafer was premodified by a monolayer of 3-aminopropyltri-ethoxysilane (3APTES) and exposed to the

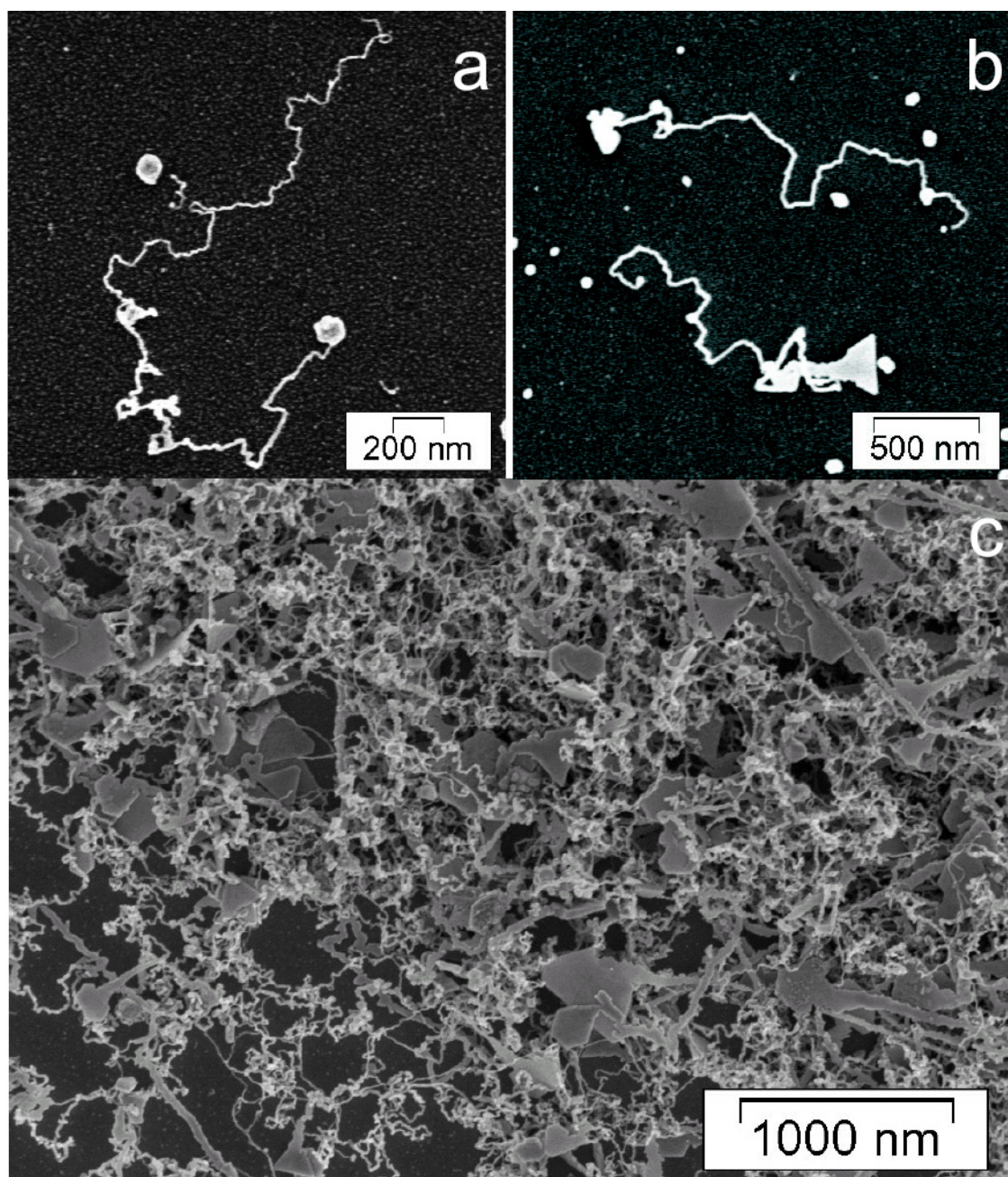


*Figure 5.13. Scanning electron micrographs of the gold nanowires a, b) deposited on a silicon wafer pre-modified by 3-APTES. c) Deposited on a silicon wafer by drying a droplet of the reaction solution*

## 5. Gold nanoparticles and gold nanowires – surface modification and synthesis

solution for 2 hours, allowing for selective electrostatic deposition of isolated negatively charged species from solution. In addition, a droplet of the solution was dried on a Si wafer in order to view the complete solid-phase content. In Fig. 5.13., images recorded on these samples with a scanning electron microscope (SEM) are displayed. In Fig 5.13. (a) and (b) single nanowires with lengths of several microns can be seen. Apart from the wires, some particles with aspect ratios close to one, showing round, triangular or polyhedral shape are found on the surface. Since these species in solution adsorb on a positively charged surface, they appear to be negatively charged. The wires sometimes end in larger spherical or triangular structures, at least the triangular ones suggest monocrystallinity. The wires themselves appear curly and twisted. Fig 5.13.c shows that a huge amount of nanowires is present in solution, indicating a satisfying reaction yield. Again, as a particular feature of most of the wires one can identify a crystalline plate at one end, which usually has a triangular shape and sometimes exceeds 100 nm in size.

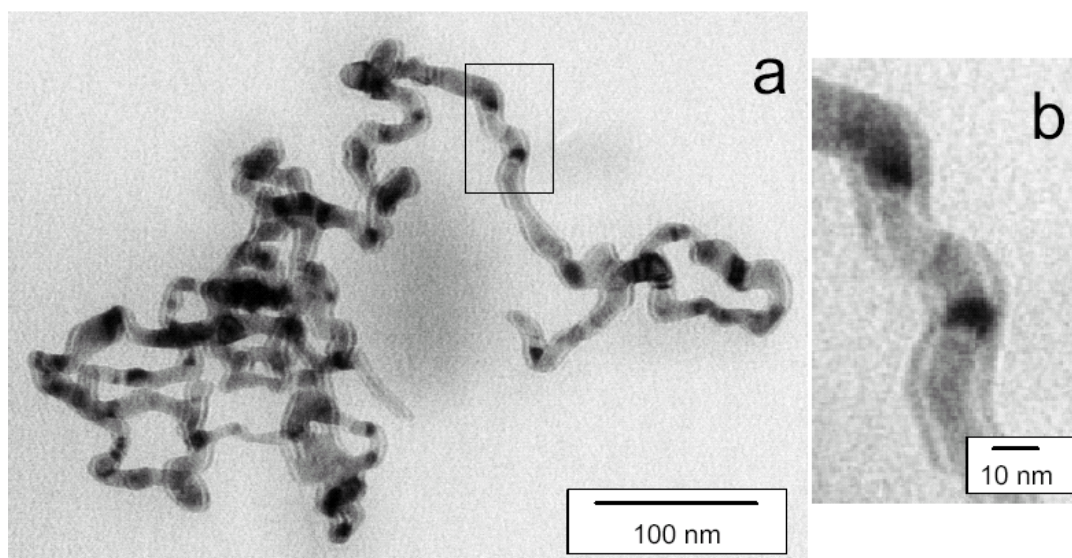


Figure 5.14. Transmission electron micrograph of a gold nanowire. b) is a magnification of the assigned area in a)

Transmission electron images (Fig. 5.14. (a) and (b)) recorded with wire samples prepared according to standard procedures show a strongly varying contrast along the wire with domains of different grey tones alternating. These domains with a typical size comparable to the wire diameter

## 5. Gold nanoparticles and gold nanowires – surface modification and synthesis

are interpreted as monocrystalline domains in a polycrystalline structure built of crystallites of different orientation, which scatter the electron beam in different ways. In Fig. 5.14.b, the wire diameter can be directly measured to be roughly 15 nm.

A gold nanowire imaged by AFM is shown in Fig. 5.15. The topographical image depicts regions with different height. Cross-sections orthogonal to the wire yield apparent wire diameters between 15 nm and 40 nm. This suggests that some portions of the wire extend away from the surface. The AFM phase image (Fig 5.15.b) shows an identical contrast along the wire, indicating a uniform material.

Additional information about the nature of the wires was obtained in a single-wire conductivity and manipulation study, which was done in cooperation with Dr. Michael Wilms. These experiments were performed by a nanomanipulation device, which could be inserted in the vacuum chamber of an SEM apparatus, thus allowing in situ observations.

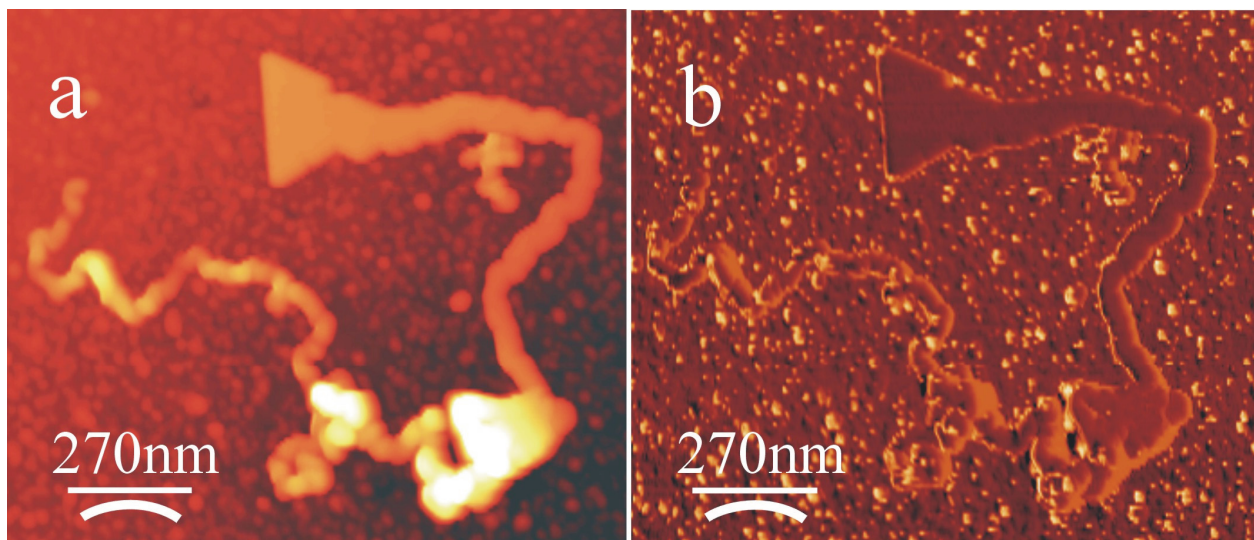


*Figure 5.15. AFM images displaying topology (a) and phase (b) of a single nanowire. The z scale in a) is 100 nm.*

In the conductivity measurements a wire was placed with both ends on two substrate gold electrodes as shown in fig. 5.16.a). A total resistance of  $R_t = 600 \Omega$  was measured in that case. This value includes the two contact resistances between nanowire and electrodes as well as the feed line resistances of the thin substrate electrodes. The total resistance was independent of the applied



## 5. Gold nanoparticles and gold nanowires – surface modification and synthesis

voltage (0 – 100 mV) indicating an ohmic (metallic) behaviour of the nanowires. In another experiment the wire was placed only with one end to the substrate electrodes and contacted by the tip serving as a second electrode (Fig. 5.16.b). The flexibility of the tip electrode offered the possibility to vary the distance between the two contacts, so that the resistance (R) versus length (L) could be measured. The dependence R/L shows linear character which indicates that the contact resistances between tip and wire are largely reproducible assuming ohmic behaviour and homogeneity of the wire. The extrapolation for the length  $L = 0$  gives the sum of all contact and feed line resistances of the circuitry ( $\sum R_{c,f} = 375 \Omega$ ). With the wire radius  $r = 8 \text{ nm}$  taken from a high resolution image and the inverse slope  $\Delta L / \Delta R = 3 \mu\text{m} / 575 \Omega$  the intrinsic conductivity  $\sigma$  of the nanowire is calculated:

$$\sigma = \Delta L / \Delta R \pi r^2 \Rightarrow \sigma = 2.6 \times 10^7 \text{ S/m}$$

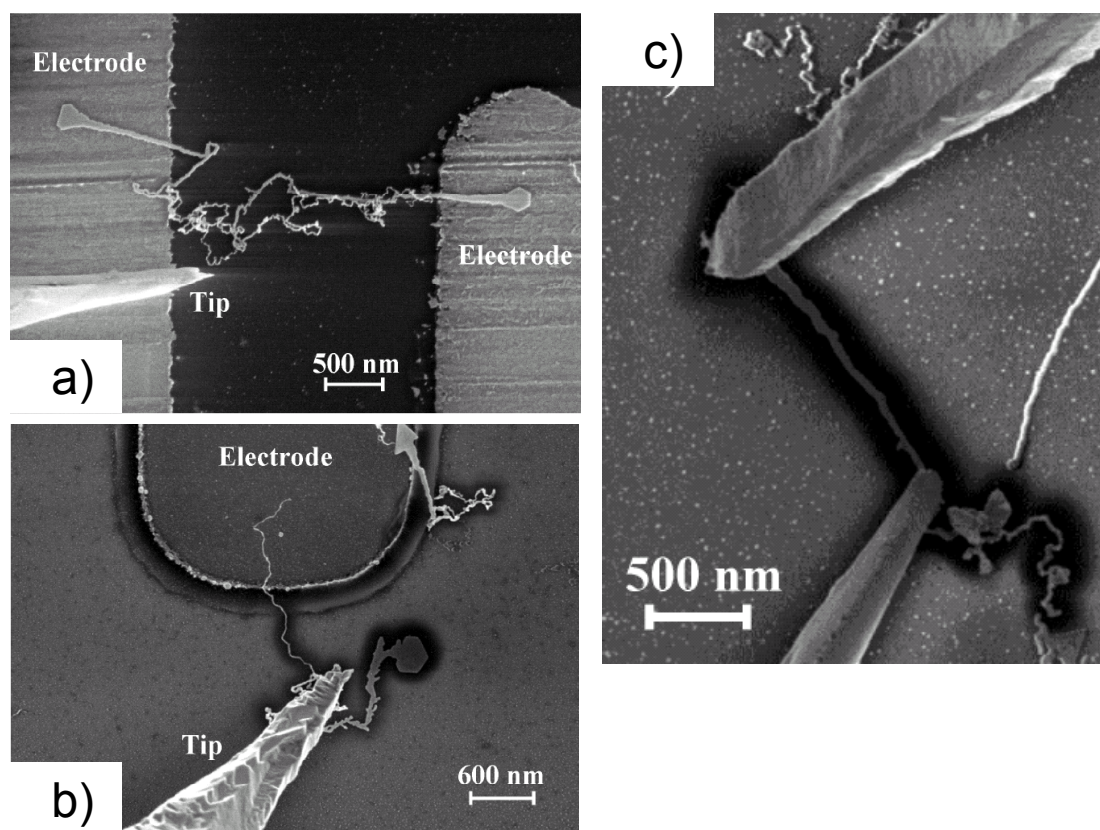


Figure 5.16. a) Gold nanowire bridging two substrate gold electrodes. b) The one end of a gold nanowire is deposited on a substrate electrode and the tip is used as a second electrode. c) A nanowire contacted by the two tip-electrodes.

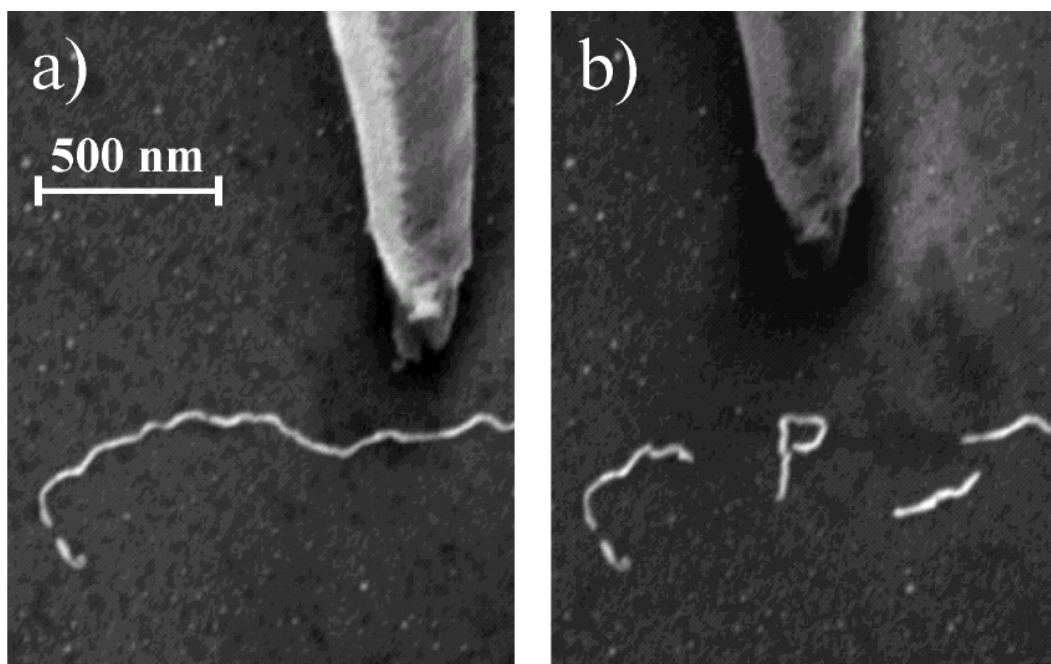


Figure 5.17. Nanomanipulation. A gold nanowire before (a) and after cutting by the tip and forming letters b).

This result of specific conductivity of  $2 \times 10^7$  S/m which is close to the bulk gold value ( $4.3 \times 10^7$  S/m), thus giving the most convincing evidence that these structures are continuous gold structures and may be used as wires in electronic applications. Using two tips for contacting (Fig. 5.16.c), almost any wire on the chip could be measured.

By increasing the applied voltage or reducing the distance between the tips at constant voltage, the current density could be increased until the rupture of the wire. From many such measurements a maximum current density of  $j_{\max} = 4 \times 10^5$  A/mm<sup>2</sup> was calculated (current density just before the wires failed). This value is more than three orders of magnitude higher than, for example, the allowable current density in conventional metal wires like those used in house wiring. The extremely high surface to volume relation of nanowires is the cause for the required large heat dissipation.

In addition, it was demonstrated there that the wires are flexible enough to be deformed without rupture, this allowing for the fabrication of simple structures such as letters without breaking (fig. 5.17). (More details about the nanomanipulation device and the measurements

could be found in ref. <sup>61</sup>)

The mechanism responsible for the formation of the gold nanowires has not yet been clarified. It has been found<sup>43, 44</sup> that MSA reduces the Au(III) present in H<sub>2</sub>AuCl<sub>4</sub> to Au(I) with the oxidative formation of a disulfide species and complexation of the Au(I) with the remaining MSA. This complex has oligomeric even polymeric character and a high density of gold atoms. The previous section 5.2 as well as a recent publication<sup>37</sup> by Negishi and co-workers demonstrated that MSA also can reduce H<sub>2</sub>AuCl<sub>4</sub> to Au(0) at ambient temperatures with the formation of small gold nanoparticles ranging from 2 to 3 nm in size. These findings agree with our observation of bulk gold features in our reaction mixture but the formation of the wire-like morphology requires additional clarification. Most likely MSA and the Au-MSA complex are capping certain facets of the growing crystals thus exposing selectively the non-capped facets to further growth. A similar mechanism was described by Xia for the synthesis of silver and lead nanowires<sup>64, 65</sup>, where PVP serves as a capping agent.

It was observed that only at a H<sub>2</sub>AuCl<sub>4</sub> : MSA ratio < 10:1 wires are formed while for ratios between 10:2 and 10:10 the reaction product consists of nanospheres with variable main size. For an even higher relative concentration of H<sub>2</sub>AuCl<sub>4</sub>, no particles could be detected by SEM but crystals with sizes below 2 nm may be present. These experimental facts support the interpretation of the wire growth mechanism being due to the competition between capping and growth.

Nonetheless, a single growing crystal facet would lead to monocrystalline, straight wires. Such morphologies are indeed observed by Xia, but not in our experiment. The polycrystallinity of our structures may be due to twinning at the growing surface or due to fusion with existing particles from solution and subsequent annealing of the junction points.

### **5.3.4. Conclusion**

In conclusion, the synthesis of long gold nanowires in aqueous solution was demonstrated. The method is simple and does not require the use of any additional surfactants. The inherent curvature of these wires leads to a high flexibility which is a prerequisite for their manipulation. In addition, real "bottom up" wiring of electronic circuits will require the directed growth of the wires

along nontrivial paths. For this goal, inherently curved wires may prove technologically important.

### References and Notes

---

- <sup>1</sup> Badia, A., Lennox, R.B., Reven, L. *Acc. Chem. Res.* **2000**, *33*, 475-481.
- <sup>2</sup> Schwartz, D.K. *Annu. Rev. Phys. Chem.* **2001**, *52*, 107-137.
- <sup>3</sup> Giersig M., Mulvaney P. *Langmuir* **1993**, *9*, 3408-3413.
- <sup>4</sup> Weisbecker, C.S., Merritt, M.V., Whitesides, G.M. *Langmuir* **1996**, *12*, 3763-3772.
- <sup>5</sup> Mayya, K.S., Patil, V., Sastry, M. *Langmuir* **1997**, *13*, 3944-3947
- <sup>6</sup> Aslan, K., Perez-Luna, V.H. *Langmuir* **2002**, *18*, 6059-6065.
- <sup>7</sup> Brust, M., Fink, J., Bethell, D., Schiffrin, D.J., Kiely, C.J. *J. Chem. Soc. Chem. Commun.* **1995**, 1655-1656.
- <sup>8</sup> Chen, S.H., Kimura, K. *Langmuir* **1999**, *15*, 1075-1082.
- <sup>9</sup> Chen, S.H., Kimura, K. *Chem. Lett.* **1999**, 233-234.
- <sup>10</sup> Kimura, K., Takashima, S., Ohshima, H. *J. Phys. Chem. B* **2002**, *106*, 7260-7266.
- <sup>11</sup> No effort was made to quantitatively determine the surface coverage in the present work. However, a self-assembled monolayer can be deduced based on the findings from the cyanide etching and seeding growth tests.
- <sup>12</sup> In the beginning this rough value was taken for estimation. Later a value of 0.156 nm<sup>2</sup> was reported in ref. 10.
- <sup>13</sup> Wang, J., Zhu, T., Song, J.Q., Liu, Z.F. *Thin Solid Films* **1998**, *327*, 591-594.
- <sup>14</sup> Knoll, W. *Annu. Rev. Phys. Chem.* **1998**, *49*, 569-638.
- <sup>15</sup> Cumberland, S.L., Strouse, G.F. *Langmuir* **2002**, *18*, 269-276.
- <sup>16</sup> Olson, L.G., Lo, Y.S., Beebe Jr., T.P., Harris, J.M. *Anal. Chem.* **2001**, *73*, 4268-4276.
- <sup>17</sup> Biggs, S., Mulvaney, P., Zukoski, C.F., Grieser, F. *J. Am. Chem. Soc.* **1994**, *116*, 9150-9157.
- <sup>18</sup> Cheney, G.E., Fernando, Q., Freiser, H. *J. Phys. Chem.* **1959**, *63*, 2055.
- <sup>19</sup> Thompson, D. W., Collins, I. R. *J. Colloid Interf. Sci.* **1992**, *152*, 197.
- <sup>20</sup> Sandroff, C. J.; Herschbach, D. R. *Langmuir* **1985**, *1*, 131.
- <sup>21</sup> Kane, V., Mulvaney, P. *Langmuir* **1998**, *14*, 3303-3311.
- <sup>22</sup> Elsner, L. *J. Prakt. Chem.* **1846**, *37*, 441-446.

- <sup>23</sup> Templeton, A.C., Hostetler, M.J., Kraft, C.T., Murray, R.W. *J. Am. Chem. Soc.* **1998**, *120*, 1906-1911.
- <sup>24</sup> Paulini, R., Frankamp, B.L., Rotello, V.M. *Langmuir* **2002**, *18*, 2368-2373.
- <sup>25</sup> Stremsdoerfer, G., Perrot, H., Martin, J. R., Clechet, P. *J. Electrochem. Soc.* **1988**, *135*, 2881-2886.
- <sup>26</sup> Turkevich, J., Stevenson, P.C., Hillier, J. *Discuss. Faraday Soc.* **1951**, *11*, 55-75.
- <sup>27</sup> Brown, K.R.; Natan, M.J. *Langmuir* **1998**, *14*, 726-728.
- <sup>28</sup> Wall, J.F.; Grieser, F.; Zukoski, C.F. *J. Chem. Soc., Faraday Trans.* **1997**, *93*, 4017-4020
- <sup>29</sup> Brown, K.R., Walter, D.G., Natan, M.J. *Chem. Mater.* **2000**, *12*, 306-313.
- <sup>30</sup> Brown, K.R., Lyon, A.L., Fox, A.P., Reiss, B.D., Natan, M.J. *Chem. Mater.* **2000**, *12*, 314-323.
- <sup>31</sup> Jana, N.R., Gearheart, L., Murphy, C.J. *Langmuir* **2001**, *17*, 6782-6786.
- <sup>32</sup> Jana, N.R.; Gearheart, L.; Murphy, C.J. *J. Phys. Chem. B* **2001**, *105*, 4065-4067.
- <sup>33</sup> Busbee, B.D., Obare, S.O., Murphy, C.J. *Adv. Mater.* **2003**, *15*, 414-416.
- <sup>34</sup> Petroski, J.M., Wang, Z.L., Green, T.C., El-Sayed, M.A. *J. Phys. Chem. B* **1998**, *102*, 3316-3320
- <sup>35</sup> Zhu, T., Vasilev, K., Kreiter, M., Mittler, S., Knoll W. *Langmuir* **2003**, *19*, 9518
- <sup>36</sup> Negishi, Y., Tsukuda, T. *J. Am. Chem. Soc.* **2003**, *125*, 4046
- <sup>37</sup> Schmid, G., Corain, B. *Eur. J. Inorg. Chem.* **2003**, 3081.
- <sup>38</sup> Kreibig, U., Vollmer, M., *Optical properties of metal clusters*; Springer, Berlin **1995**.
- <sup>39</sup> Schmid, G., Corain, B. *Eur. J. Inorg. Chem.* **2003**, 3081.
- <sup>40</sup> Mie, G. *Annal. Phys.* **1908**, *5*, 377.
- <sup>41</sup> Cumberland, S.L., Strouse, G.F. *Langmuir* **2002**, *18*, 269.
- <sup>42</sup> Nomiya, K., Yokoyama, H., Nagano, H., Oda, M., Sakuma, S. *Bull. Chem. Soc. Jpn* **1995**, *68*, 2875.
- <sup>43</sup> Brown, D.H., Paton, M., Smith, W.E. *Inorganica Chimica Acta* **1982**, *66*, L51.
- <sup>44</sup> special issue of Nature **2000**, *406*, 1021.
- <sup>45</sup> Edelstein, A. S., Cammarata, R. C. *Nanomaterials: Synthesis, Properties, and Applications*, Institute of Physics, Philadelphia, PA, **1996**.
- <sup>46</sup> Klabunde K. J. *Nanoscale Materials in Chemistry*, Wiley-Interscience, New York, **2001**.
- <sup>47</sup> Hu, J., Ouyang, M., Yang, P., Lieber, C. M. *Nature* **1999**, *399*, 48.

- <sup>48</sup> Wang, Z., Su, Y-K., Li, H-L. *Appl. Phys. A.* **2002**, *74*, 563.
- <sup>49</sup> Yu, S.F., Li, N.C., Wharton, J., Martin, C.R. *Nano Letters* **2003**, *3*, 815.
- <sup>50</sup> Bietsch, A., Michel, B. *App. Phys. Lett.* **2002**, *80*, 3346.
- <sup>51</sup> Dumpich, G., Friedrichowski, S., Lohau, J. *J. Phys. Soc. Jpn.* **2000**, *69*, 99.
- <sup>52</sup> Schopfer, F., Bauerle, C., Rabaud, W., Saminadayar, L. *Phys. Rev. Lett.* **2003**, *90*, 056801.
- <sup>53</sup> Wirtz, M., Martin, C. R. *Adv. Mater.* **2003**, *15*, 455.
- <sup>54</sup> Han, Y.J., Kim, J.M., Stucky, G.D. *Chem. Mater.* **2000**, *12*, 2068.
- <sup>55</sup> Djalali, R., Li, S-Y., Schmidt, M. *Macromolecules* **2002**, *35*, 4282.
- <sup>56</sup> Harnack, O., Ford, W.E., Yasuda, A., Wessels, J.M. *Nano Letters* **2002**, *2*, 919.
- <sup>57</sup> Teranishi, T., Sugawara, A., Shimizu, T., Miyake, M. *J. Am. Chem. Soc.* **2002**, *124*, 4210.
- <sup>58</sup> Yin, Y., Lu, Y., Gates, B., Xia, Y. *J. Am. Chem. Soc.* **2001**, *123*, 8718.
- <sup>59</sup> Sun, Y., Gates, B., Mayers, B., Xia, Y. *Nano Letters* **2002**, *2*, 165.
- <sup>60</sup> Wang, Y., Herrick, T., Xia, Y. *Nano Letters* **2003**, *3*, 1163.
- <sup>61</sup> “Manipulation and conductivity measurements of gold nanowires” by M. Wilms, J. Conrad, K. Vasilev, M. Kreiter and G. Wegner, submitted to *Applied Surface Science*.

### **6. Plasmon coupling between a flat gold interface and gold nanoparticles.**

#### **6.1. Introduction**

In this outlook oriented chapter the applicability of the multilayered system used in chapter 4.1., for the study of the behaviour of fluorohpores in the vicinity of more complex metal objects as colloidal gold nanoparticles will be described.

SPR in combination with gold nanoparticles for enhancement of the sensitivity of the instrument has been explored in several works.<sup>1, 2, 3, 4</sup> In addition the coupling between a metal layer and a layer of small silver particles in SiO<sub>2</sub> matrix was studied by Kume et al..<sup>5, 6, 7, 8, 9</sup> The effect of the separation distance between an Aluminium film and a Ag-SiO<sub>2</sub> layer as well as the thickness of the Ag-SiO<sub>2</sub> layer on the reflectivity and scattering spectra were investigated.

In this study, colloidal gold nanoparticles with size of about 17 nm were deposited onto polyelectrolyte spacers thus providing variable separation distance between the gold particles and a gold film. The reflectivity spectra obtained at wavelengths between 480 and 780 nm were analysed and the optical constant of each layer extracted.

#### **6.2. Experimental**

Samples for this experiment were prepared as follows. Ultraflat gold surfaces were deposited on glass BK7 by the method of template striping gold from mica (described in Chapter 3.3.). The gold film was then functionalised by a self assembled monolayer of 3-mercaptopropionic acid (procedure described in chapter 3.1.) thus providing carboxylic end groups on the surface which are dissociated in water. A multilayered system of polyallyl amine (PAH) and polystyrenesulfonate (PSS) was build on the surface starting from a positively charged layer of PAH as described in Chapter 3.2. The number of layers was varied in order to provide different separation distance between the gold interface and the layer of gold nanoparticles. Samples composed of 1, 3, 5, 7, 9 layers were prepared. The deposition was always terminated by a positively charged layer of PAH in order to allow for the electrostatic deposition of negatively charged gold nanoparticles on the top.

Gold nanoparticles were synthesized by the method of reduction of hydrogen tetrachloroaurate by 3-sodium citrate. The synthetic recipe is described in Chapter 3.4. The surface of the particles was then modified by 2-mercaptosuccinic acid according to Chapter 5.1. The deposition of gold nanoparticles on polyelectrolyte surface was performed for 10 minutes as

## 6. Plasmon coupling between a flat gold interface and gold nanoparticles.

the colloidal solution of gold nanoparticles was diluted 2 times before use. The dilution was necessary in order to minimize the particles aggregations on the surface.

Scanning Electron Microscopy and Atomic Force Microscopy inspections were done in order to prove the quality of the samples.

Fig. 6.1. shows the surface of a multiplayer system composed of 4 bilayer PSS/PAH deposited on a silicon wafer premodified with 3-APTES. This SEM image reveals a large area of the surface (about 4 x 3 microns). Only single particles and no aggregations are present on the surface.

Since SEM provides information only about the lateral characteristics of the surface AFM was involved in order to reveal the properties of the sample in vertical direction. One

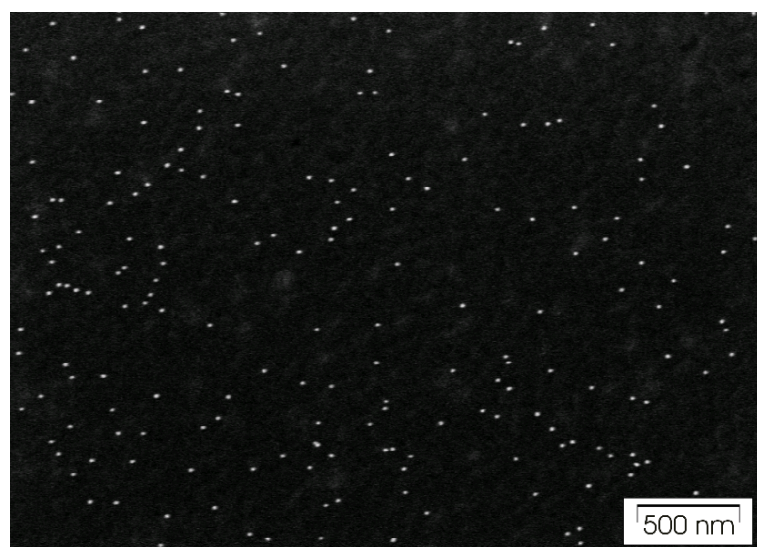


*Figure. 6.1. SEM image of gold nanoparticle on polymer spacer consisting of 4 bilayer PSS/PAH deposited on silicon wafer premodified with 3-APTES.*

topology AFM image of the surface of a sample consisting of 9 layers PAH/PSS deposited on template stripped gold film is shown in fig. 6.2. Again no aggregations of particles are seen on the surface. The particles size measured in z direction is about 17 nm. Also the very smooth surface of the polyelectrolyte spacer is notable. A cross section shows the same height of all particles, which suggests: first a narrow size distribution and second that the particles do not sink into the polymers.

The optical response of the system was investigated by a Surface Plasmon Spectrometer which is described in Chapter. 3.6. Small modifications were made. As a light source a lamp with large spectral range was used. The light was then coupled to a monochromator (HoloSpec™  $f/1.8i$  holographic imaging, Kaiser Optical Systems, Inc.) which allowed the selection of a very narrow wavelength region (1-2 nm) in the range between  $\lambda = 480 - 780$  nm. The light with the selected wavelength was coupled through an optical fibre to a collimator. The collimated light beam then passed the same optical elements like in fig. 3.7. The detection of the reflected



## 6. Plasmon coupling between a flat gold interface and gold nanoparticles.

light was done by a photomultiplier tube since the conventional silicon photodiode was not sensitive enough. For the alignment of the instrument a He-Ne laser was used.

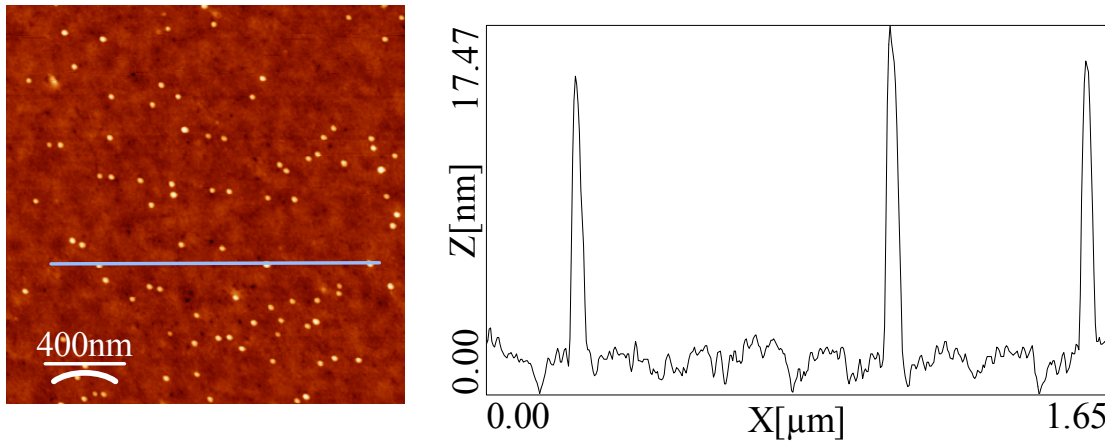


Figure 6.2. AFM image and the corresponding cross section of gold nanoparticles deposited on a polymer spacer consisting of 9 layers PAH/PSS deposited on a template stripped gold film

In order to detect the light intensity at the base of the prism due to scattering losses or/and coupling between the surface plasmon resonance of the gold substrate and the plasmon resonance on the gold nanoparticles the sample was fixed at the angle of excitation of surface plasmon resonance. A He-Ne laser was used for excitation. The PMT was moved at the base of the sample of a range between +50 and -50 degree (if 0 degree corresponds to the point of intercept to the normal of the sample).

### 6.3. Results and discussion

Reflectivity scans of a sample with three layers (PAH/PSS/PAH) are shown in fig 6.3. The solid lines represents samples without gold nanoparticles and the markers show the scans after the deposition of gold nanoparticles. The wavelength used is depicted as a number 1 – 480 nm, 2 – 520 nm, 3 – 570 nm, 4 – 620 nm, 5 - 670 nm, and 6- 750 nm. Several features should be noted. With increasing the excitation wavelength the minimum of the reflectivity shifts to a lower angle and the dip becomes narrower. The intensity of the reflected light before the angle of total internal reflection increases with increasing the excitation wavelength. After deposition of gold nanoparticles a shift to a larger angle for all reflectivity spectra is observed as the width of the resonance broadens. In addition after deposition of gold nanoparticles, at a wavelength larger than 550 nm the minimum of the reflectivity is deeper in comparison to the spectra without gold

## 6. Plasmon coupling between a flat gold interface and gold nanoparticles.

nanoparticles. Such reflectivity scans were detected for samples consisting of 1, 3, 5, 7, and 9 polyelectrolyte layers as the wavelength used was in the range 480 – 780 nm in steps of 10 nm.

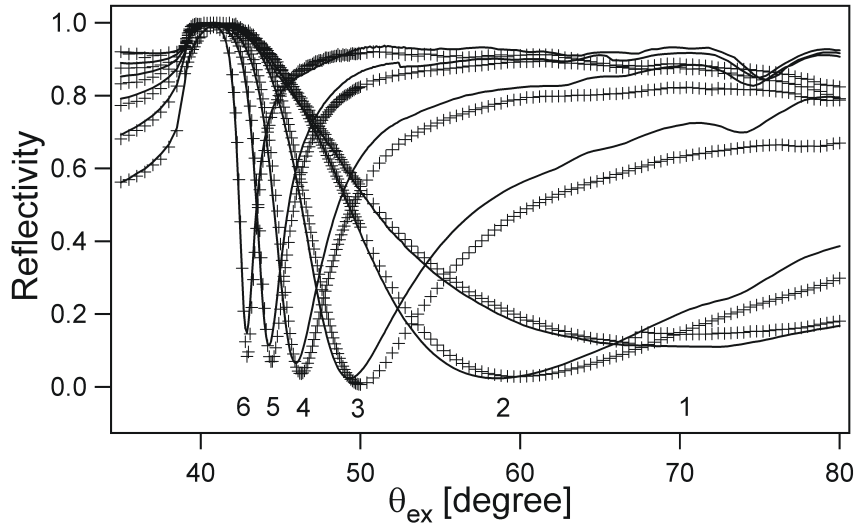


Figure 6.3. Reflectivity spectra of a sample composed of 3 layers with (crosses) and without (solid curves) gold nanoparticles. The scans are at wavelengths of 480 nm (1), 520 nm (2), 570 nm (3), 620 nm (4), 670 nm (5), and 750 nm (6).

All reflectivity scans were analysed by the matrix evaluation method (Chapter 2.1.1.4.). Thus the thickness and the dielectric constants for each layer can be determined. The thickness of the gold layer was found to be 40.6 nm. The effective thickness of the dielectric spacer was 1.1 nm, 4.6 nm, 11.4 nm, 18.4 nm, and 27 nm for 1, 3, 5, 7, and 9 layers, respectively. In the analysis the gold nanoparticles were modelled as a continuous layer and the thickness of this layer of gold nanoparticles was assumed to be 5 nm. Interesting is the behaviour of the gold nanoparticles when they are placed at different separation distance to the gold film. Fig. 6.4.a and 6.4.b show the real and imaginary part of the effective dielectric constant of the layer of gold nanoparticles as a function of the excitation wavelength. The real part of dielectric constant (6.4.a) for particles at the closest separation distance exhibit highly negative values almost like bulk gold. With increasing the separation distance the particles behave less metallic. Also notable is the higher values of the real part of the dielectric function at a wavelength of about 520 nm for the smallest spacer thickness which could be attributed to the plasmon resonance of the gold nanoparticles. This feature is available for all separation distances as the maximum shifts to a longer wavelength and broadens with increasing the spacer thickness. A similar trend is seen with the imaginary part of the dielectric constant of the layer of gold nanoparticles. With increasing the separation distance the values of the imaginary part of the dielectric constant decrease. In the sample consisting of 3 polymer layers a maximum in the imaginary part of the

## 6. Plasmon coupling between a flat gold interface and gold nanoparticles.

dielectric constant at the wavelength of plasmon resonance of the gold nanoparticles is found. Similarly as in the real part of the dielectric constant for the same sample, this peak at about 520 nm is very strong interpreted as an enhanced plasmon resonance of the gold particles. With increasing the separation distance this peak shifts to a longer wavelength and broadens.

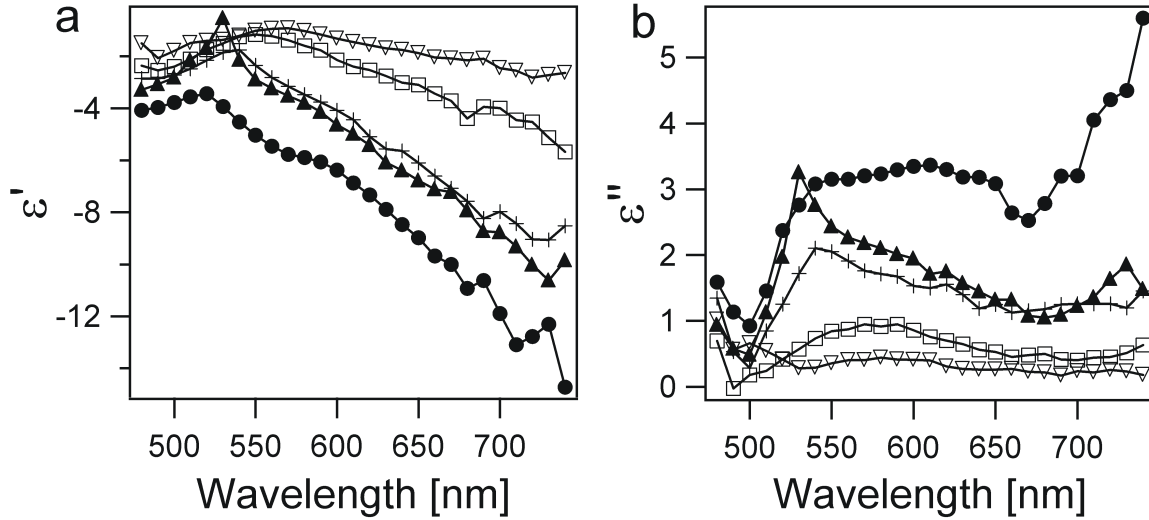


Figure 6.4. The real part (a) and the imaginary part (b) of the dielectric constant of the layer of gold nanoparticles as a function of the wavelength of excitation for samples with different thickness of the polymer spacer: 1.1 nm (filled circles), 4.6 nm (filled triangles), 11.4 nm (crosses), 18.4 nm (open squares), and 27 nm (open triangles).

At the very close separation distance (1 layer) the gold nanoparticles show high absorption, which spans over a long wavelength range (500-650 nm), then slightly decreases and then increases again. This is due to the so called gap mode at the very proximity of the gold nanoparticles to the gold substrate caused by the multipoles that are induced by the image dipole in the substrate.<sup>10</sup>

The light intensity emitted behind the sample was also measured. Fig. 6.5. shows these measurements. The intensity of the scattered light after deposition of gold nanoparticles is 6 orders of magnitude stronger than in the case of bare polymer surface. Scattering pattern was not observed. This is due to the excitation wavelength (632.8 nm) used in these measurements.

The results described above imply that the surface plasmon field excited at the flat gold interface excites a local plasmon field into the gold nanoparticles. The strength of coupling between both fields decreases with increasing of the spacer thickness. This leads to a different optical response of the gold nanoparticles when they are deposited at different separation distance to the gold interface.

## 6. Plasmon coupling between a flat gold interface and gold nanoparticles.

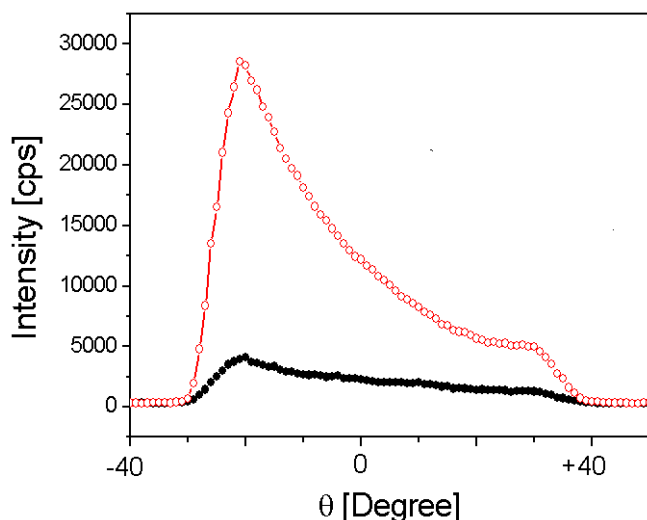


Figure 6.5. Light intensity measured behind the sample for a spacer built of 5 layers, with (open circles) and without (filled circles) gold nanoparticles. The excitation intensity was 632.8 nm.

### 6.4. Conclusion

A controlled multilayered system consisting of metal layer, polymer spacer with variable and defined thickness, and a layer of separate gold nanoparticles was constructed. The optical response of the system in Kretschmann configuration was determined. The dielectric constants of the layer of gold nanoparticles at different separation distance to the gold layer and wavelength were extracted showing distinct reduction of the metallic response of the gold nanoparticles.

This work is the fundament of a possible new research approach for study the fluorescence emitted from dye molecules near metal objects with complex structure. The enhanced electromagnetic field around the gold nanoparticles as well as the coupling with the surface plasmon field of the gold substrate could result in an enhanced fluorescence emission. This could lead to better understanding of the fluorescence phenomenon as well as the development of new sensor techniques.

### References

- <sup>1</sup> Lyon, L. A., Pena, D. J., Natan, M. J. *J. Phys. Chem. B* **1999**, *103*, 5826-5831.
- <sup>2</sup> He, L., Musick, M. D., Nicewarner, S. R., Salinas, F. G., Bencovic, S. J., Natan, M. J., Keating, C. D. *J. Am. Chem. Soc.* **2000**, *122*, 9071-9077.
- <sup>3</sup> Lyon, L. A., Musick, M. D., Natan, M. J. *Anal. Chem.* **1998**, *70*, 5177-5183.
- <sup>4</sup> Yamaguchi, A., Juodkazis, S., Matsuo, S., Misawa, H. *Chem. Lett.* **2002**, 190-191.
- <sup>5</sup> Kume, T., Hayashi, S., Yamamoto, K. *Phys. Rev. B* **1997**, *55*, 4774-4755.
- <sup>6</sup> Kume, T., Nakagawa, N., Hayashi, S., Yamamoto, K. *Solid State Comm.* **1995**, *93*, 171-175.
- <sup>7</sup> Kume, T., Nakagawa, N., Hayashi, S., Yamamoto, K. *Superlattices and Microstr.* **1994**, *15*, 459-462.
- <sup>8</sup> Kume, T., Kitagawa, T., Hayashi, S., Yamamoto, K. *Surf. Sci.* **1998**, *359*, 23-29.
- <sup>9</sup> Kume, T., Hayashi, S., Yamamoto, K. *Mater. Sci. and Eng. A* **1996**, *217/218*, 171-175.
- <sup>10</sup> Okamoto, T., Yamaguchi, I. *J. Phys. Chem. B* **2003**, *107*, 10321-10324.

## **7. Summary and Outlook**

The results of this work can be separated in two parts – the experimental and theoretical assessment of the fluorescence in the vicinity of a flat gold interface, and the surface modification and synthesis of gold nanoparticles and gold nanowires. At the end first steps to a more complex study on the fluorescence intensity near more complex objects as gold nanoparticles were done.

A defined multilayer architecture at the nanometer scale for the study of the fluorescence in the presence of a metal interface was designed and precisely experimentally implemented. An ultrasmooth gold film was used in combination with self-assembled monolayers and layer-by-layer deposition of polyelectrolytes allowing for the separation of fluorescing dyes from a gold interface in a controlled and precise manner. The characteristics (thickness, roughness, optical constants) of the layers were fully analysed by a variety of techniques (Small Angle X-ray Reflectivity, Atomic Force Microscopy, Surface Plasmon Spectroscopy).

In Chapter 4 the behaviour of fluorescing dyes at a planar metal-dielectric interface was investigated in Kretschmann configuration. The fluorescence intensity, angular distribution of the emission, and photobleaching rate of fluorescing molecules placed at different separation distance to the gold interface were experimentally and theoretically evaluated. A perfect correlation between theory and experiment was found for a separation distance larger than 15 nm. Surprisingly, a clear discrepancy between measurement and experiment was determined at very close proximity to the gold layer, though experiments on the excitation lifetime of europium complex conducted by other researchers showed very good correlation to the theory. In order to clarify that, the problem was addressed on single molecule level which confirmed the results with an ensemble of molecules. One speculation on the reason for the discrepancy between the results described here and others results may imply that this is due to the stronger oscillator strength of fluorophore used in the current study (compared to the Europium complex which is phosphorescent) which leads to stronger interaction with the gold interface. Another reason could be the ultrasmooth gold interface used in experiments described here, since it is known that rough metal surfaces can lead to enhancement of the fluorescence. Moreover, it is known that the very elegant Langmuir-Blodgett deposition technique used in the experiments before, often leads to films with pinholes, defects and domains which will be a reason for inhomogeneous distribution of the dye in vertical direction. Although, the complete understanding of the effects described above might need further experimental and theoretical

attention, this study is a significant contribution to the application of Surface Plasmon Fluorescence Spectroscopy as an analytical tool for detection of surface recognition reactions as well as in all processes where a fluorescing dye is used with a metal interface.

The second part of this work was dedicated to gold nanoparticles and gold nanowires (Chapter 5). Firstly, the undefined shell of physically adsorbed ions on the surface of citrate reduced gold nanoparticles was exchanged by a self-assembled monolayer of 2-mercaptopropionic acid. Series of comparative tests unambiguously proved a successful surface modification expressed in a better pH stability and cyanide dissolution resistance. Then a new route for the synthesis of monolayer protected gold nanoparticles with size above 10 nm was established. The syntheses were conducted in aqueous medium as only  $\text{HAuCl}_4$  and 2-MSA were used, without employing any additional reduction agent. This new synthesis can be very useful in cell imaging, DNA labels, catalysts or optical sensors, applications where narrow size distribution is not required. At a particular molar ratio between the reagents this new synthesis resulted in gold nanowires. The synthetic procedure is simple, one step, conducted in aqueous medium and without the use of any additional surfactants. The length of the gold wires is in the order of micrometers and the cross section down to 15 nm. Surface analytical techniques such as SEM, TEM and AFM were used in order to clarify the structure and morphology of the wires. Conductivity measurements of a single wire proved its metallic properties. The suitability of the wires for nanomanipulation as well as the very high current density suggests their usefulness for application in nanoelectronic devices. The synthesis of nanowires in solution is also interesting from a point of view to reaching the gram scale production and their use as fillers, since the production of a composite conducting material will require 10 times less material if metal particles are exchanged with wires.

Pursuing the ultimate goal, or the behaviour of fluorescing dyes near more complex metal objects, a multilayered architecture involving a gold interface and gold nanoparticles, which were separated by a well defined polymer spacer was constructed. The properties of the system were fully characterized by surface and optical analytical techniques. The optical constants of the gold nanoparticles were found to be strongly dependent on the separation distance to the gold interface.

In an outlook, a next step of research involving the multilayered system described in Chapter 6 could be the deposition of fluorescing dyes around the gold nanoparticles. The plasmon field of the gold nanoparticles, excited by the surface plasmon field of the flat gold interface could lead to a modification of the emission rate of the fluorophore expressed in an enhanced emission. The direct consequence of that could be an improved sensitivity of the

instrument. Another possible variation could be the deposition of a polymer spacer around the gold nanoparticles. This could happen in solution or on surface. Then the influence of the separation distance between the curved interface of the gold nanoparticles and a fluorescing dye can be investigated. Another approach can be the deposition of fluorophore between two gold nanoparticles or a gold nanoparticle and a flat gold interface. In this case the enhanced electromagnetic field between the two metal surfaces will impact on the radiative emission of the dye.

This work is to be understood as a small step toward the understanding of the behaviour of fluorescing species in the vicinity of a metal interface. For complete revealing of the corresponding phenomena more work should be done in the future. Due to its complexity, the research should involve the efforts of interdisciplinary teams composed of scientists with diverse background.

Hiermit erkläre ich, daß ich die vorliegende Arbeit selbständig und ausschließlich unter Verwendung der angegebenen Hilfsmittel angefertigt habe. Wörtliche bzw. inhaltliche Zitate werden durch Quellenangaben kenntlich gemacht.

Mainz, 14.05.2004



## ***Acknowledgements***

The author thank deeply to:

*Prof. Wofgang Knoll*

*For giving me the chance to do my Ph. D. at the Max-Plank Institute for Polymer Research, Mainz*

*Prof. Gert Müller*

*For being my Doctorvater at the Martin - Luther University in Halle*

*Dr. Max Kreiter*

*For being my direct supervisor at the Max-Plank Institute for Polymer Research, Mainz. For all the time he spent with me discussing scientific and personal problems. Max thanks for supporting me all the time.*

*Dr. Tao Zhu*

*For introducing me in the world of gold nanoparticles. For the nice one year working together. For the hospitality when we met in China.*

*Dr. Kaloyan Koynov*

*For the many times explaining me basic physical phenomena.*

*Señor Don Fernando Stefani*

*For the enjoyable time working together and having nice time out of work*

*Herrn Volker Jacobsen*

*For helping me to manage with tons of administrative challenges.*

*Dr. Tania Dimitrova*

*For the scientific help and friendship.*

*The author also wish to thank for the help in the research to*

*Gunnar Glasser(for SEM), Dr. Ingo Lieberwirth(for TEM), Dr. Ruediger Berger and Dr. Bernd Grohe (for AFM), Yun Zong, Michael Wilms ( for nanomanipulation), Dr. Rio Kita (for Dynamic Light Scattering), Dr. Yun Zong (for teaching me Small Angle X-ray reflectivity), Dr. Renate Naumann, Hans-Jorg Menges, Walter Schöldei. Fang Yu, Dr. Hose Lopes, Prof. Silvia Mittler*

*The time at the MPIP was one of the most enjoyable in my life and contribution to that have many other colleagues and friends.*

*Dr. Stuart Fraser, Dr. Toby Jenkins, Dr. Adem Akaya, Giorgio Zoppellaro, Dr. Kirstin Peterson, Dr. Angela Vogt, Dr. Gudrun Stengel, Dr. Marco Stemmler, Betina Wendling, Heiko Rochholz, Sabine Pülz, Martina Knecht, Gretl Dworschak, Hyong Sik, Dr. Tomas Neumann, Jennifer Shumaker, Prof. Roger Horn, Catherine Breffa, Natalia Stoyanova, Petko Petkov, Cassis Killian, Galina Vasileva and many others...*

*Special thanks to Agnieszka Merczynska*

# *Curriculum Vitae*

Krasimir Vasilev  
born on 20.08.1972, in Burgas, Bulgaria

## **Education**

1979 - 1987	Primary school, Varna, Bulgaria
1979 - 1987	Secondary Technical School of Electrical Engineering, Varna, Bulgaria
Sept. 1991 – Jan. 1997	Masters Degree in Chemical Engineering “Prof. Dr. A. Zlatarov” University, Bourgas, Bulgaria
March 1996 - Jan. 1997	Diploma Thesis on “Modification of unsaturated rubbers with polysulfide oligomers ”
July 2001 – present	Max-Plank Institute for Polymer Research, Mainz, Germany - Ph. D. student in the group of Prof. Wolfgang Knoll

## **Publications**

Krasimir Vasilev, Wolfgang Knoll, and Maximilian Kreiter, “Fluorescence intensities of chromophores in front of a metal surface”, *Journal of Chem. Physics* **2004**, 120(7), 3439-3445.

Krasimir Vasilev, Fernando Stefani, Volker Jacobsen, Wolfgang Knoll, and Maximilian Kreiter, “Reduced photobleaching of chromophores close to a metal surface”, *Journal of Chem. Physics* **2004**, 120(14), 6701-6704.

T. Zhu, K. Vasilev, M. Kreiter, S. Mittler, W. Knoll, "Surface Modification of Citrate-Reduced Colloidal Gold Nanoparticles with 2-Mercaptosuccinic Acid", *Langmuir* **2003**, 19(22), 9518 – 9525.

Krasimir Vasilev, Tao Zhu, Michael Wilms, Silvia Mittler, Wolfgang Knoll and Maximilian Kreiter “A simple, one step synthesis of gold nanowires in an aqueous solution”, to be submitted to *Langmuir*.

Krasimir Vasilev, Tao Zhu, Silvia Mitler, Wolfgang Knoll and Maximilian Kreiter “A novel method for synthesis of gold nanoparticles and gold nanowires”, to be submitted to *Langmuir*.

M. Wilms, J. Conrad, K. Vasilev, M. Kreiter and G. Wegner, “Manipulation and Conductivity Measurements of single Au-Nanowires”, *Applied Surface Science* **2004**, 238, 490–494

Naumann R, Schiller SM, Giess F, Grohe B, Hartman KB, Karcher I, Koper I, Lubben J, Vasilev K, Knoll W, “Tethered lipid Bilayers on ultraflat gold surfaces”, *Langmuir* **2003**, 19, 5435-5443.

Hernandez-Lopez JL, Bauer RE, Chang WS, Glasser G, Grebel-Koehler D, Klapper M, Kreiter M, Leclaire J, Majoral JP, Mittler S, Mullen K, Vasilev K, Weil T, Wu J, Zhu T, Knoll W “Functional polymers as nanoscopic building blocks”, *Materials Science & Engineering C-Biomimetic And Supramolecular Systems* **2003**, 23 (1-2), 267-274.

Fernando D. Stefani, Krasimir Vasilev, Noelia Bocchio, Natalia Stoyanova, Wolfgang Knoll and Maximilian Kreiter “Surface plasmon mediated single molecule fuorescence through a thin metallic film”, submitted to *Phys. Rev. Lett.*

## Zusammenfassung

Heutzutage ist die Fluoreszenz-Spektroskopie eine verbreitete Methode in der biomedizinischen Forschung und die am meisten genutzte Methode in der medizinischen Diagnose, der DNA-Sequenzanalyse und der Genomforschung. Die Grundlagen der Fluoreszenz sind einschließlich der Faktoren, die die Emission beeinflussen, wohlverstanden (z. B. Quenching, Umwelteinflüsse, Resonanzenergietransfer und Rotationsenergie). Die Fluoreszenz-Spektroskopie wird zur Untersuchung der Struktur und Dynamik von Makromolekülen und deren Wechselwirkung untereinander eingesetzt. Die Intensitäts-, Energietransfer- und Anisotropiemessung sind weit verbreitete Methoden in der DNA-Hybridisierungsmessung, der Arzneimittelentwicklung und der HIV-Analyse.

Es ist bekannt, daß sich das Verhalten fluoreszierender Verbindungen in der Umgebung von metallischen Objekten verändert. Dies kann zur Abschwächung (ebene Metallgrenzfläche) oder Verstärkung (raue Metalloberfläche, Metallpartikel) der emittierten Fluoreszenz führen. Das Ziel dieser zukunftsweisenden Arbeit ist die Erforschung des Verhaltens eines Fluorophores in der direkten Umgebung einer Metalloberfläche, da das Verständnis des zugrunde liegenden Phänomens sehr wichtig für alle Prozesse ist, in denen fluoreszierende Farbstoffe an Metalle angrenzen (Solarzellen, LED's) insbesondere für Anwendungen in der Sensorik.

Die Ergebnisse dieser Arbeit können in zwei Abschnitte eingeteilt werden: Die experimentelle und theoretische Untersuchung der Fluoreszenz an ebenen Goldgrenzflächen und die Synthese und Oberflächenmodifizierung von Goldnanopartikeln und – nanodrähten. Abschließend wurden erste Untersuchungen zur Fluoreszenzintensität in der Umgebung komplexer Objekte durchgeführt.

Zur Untersuchung der Fluoreszenz in Gegenwart metallischer Grenzflächen wurde ein definiertes Mehrlagensystem im nm-Maßstab dargestellt und experimentell untersucht. Eine sehr glatte Goldschicht wurde zusammen mit einer sich selbst anordnenden Monolage und einer schichtweisen Anordnung von Polyelektrolyten benutzt, um einen fluoreszierenden Farbstoff in einem kontrollierbaren Abstand von der Goldoberfläche anzuordnen. Die charakteristischen Eigenschaften (Schichtdicke, Rauigkeit, optische Eigenschaften) dieser Schichten wurden mit verschiedenen Techniken (Kleinwinkel-Röntgenreflektivität, Rasterkraft-Mikroskopie, Oberflächen-Plasmonenspektroskopie) untersucht.

In Kapitel 4 wird das Verhalten fluoreszierender Farbstoffe auf einer flachen metallisch-dielektrischen Oberfläche in Kretschmann-Anordnung untersucht. In diesem Kapitel wurde die Intensität der Fluoreszenz, die Winkelverteilung der Emission und die Bleichungsquote von fluoreszierenden Molekülen, die sich in unterschiedlichen Abständen von der Goldoberfläche befinden experimentell und theoretisch untersucht. Die Ergebnisse der theoretischen und experimentellen Versuche stimmen ab einem Abstand von 15 nm überein. Überraschenderweise kommt es aber bei kürzeren Abständen zu Abweichungen zwischen der Theorie und dem experimentellen Ergebnis, obwohl Experimente mit den entsprechenden Europium-Komplexen über die Lebensdauer im angeregten Zustand eine gute Übereinstimmung zur Theorie ergeben. Um dieses Problem zu klären wurden auch einzelne

Moleküle untersucht, die das vorherige Ergebnis aber bestätigten. Eine mögliche Ursache für die Diskrepanz zwischen den hier beschriebenen und den bisher bekannten Ergebnissen kann die stärkere Oszillator-Kraft der hier verwendeten Fluorophore (im Vergleich zu den phosphoreszierenden Europium-Komplexen) sein, die zu stärkeren Wechselwirkungen mit der Goldoberfläche führt. Eine weitere Ursache für die Abweichung von den bekannten Ergebnissen ist möglicherweise die hier benutzte sehr glatte Goldoberfläche, da bekanntermaßen rauhe Metalloberflächen zu einer Steigerung der Fluoreszenz führen. Ferner ist es bekannt, daß die früher benutzte Langmuir-Blodgett-Abscheide-Methode zu Oberflächen mit Löchern, Fehlern und Bereichen mit inhomogener Verteilung der Farbstoffe in senkrechter Richtung führt. Obwohl es zum vollständigen Verständnis der hier beschriebenen Effekte weiterer experimenteller und theoretischer Anstrengungen bedarf, ist diese Arbeit ein wichtiger Beitrag zur Anwendung der Oberflächen-Plasmonen-Fluoreszenzspektroskopie als Analysenmethode für Reaktionen auf Oberflächen und für Vorgänge bei denen ein fluoreszierender Farbstoff an einer metallischen Grenzfläche benutzt wird.

Der zweite Teil dieser Arbeit befasst sich mit Goldnanopartikeln und – nanodrähten (Kapitel 5). Zunächst wurde die physisorbierte Citrat-Hülle von Citrat-reduzierten Goldnanopartikeln gegen eine selbstorganisierte Monolage von 2-Mercaptobernsteinsäure ausgetauscht. Eine Reihe von Versuchen hat eindeutig bewiesen, daß diese Oberflächenmodifikation zu einer besseren pH - und Cyanidstabilität der Goldnanopartikellösung führt. Weiterhin wurde ein neuer Syntheseweg zur Darstellung monolagen-geschützter Goldnanopartikel (< 10 nm) gefunden. Die Darstellung erfolgt ohne Zugabe weiterer Reduktionsmittel im wäßrigen Medium aus Chlorgoldsäure und 2-Mercaptobernsteinsäure. Dieser neue Syntheseweg kann sich in der Zellabbildung, der DNA-Analyse, der Katalyse oder bei optischen Sensoren als nützlich erweisen, da hier keine engen Größenverteilungen benötigt werden. Bei einem bestimmten Molverhältnis zwischen den beiden Edukten erhält man bei dieser Synthese auch Goldnanodrähte. Die Synthese der Drähte verläuft im wässrigen Medium ohne Zugabe weiterer Detergentien in einem Reaktionsschritt. Die so entstandenen Drähte sind einige Mikrometer lang und der Querschnitt beträgt ca. 15 nm. Verschiedene Oberflächenanalysenmethoden wurden zur Aufklärung der Struktur und Morphologie der Drähte angewandt. Leitfähigkeitsmessungen an einem einzelnen Draht bestätigten seine metallischen Eigenschaften. Diese Drähte eignen sich aufgrund ihrer hohen Stromdichte sowohl für verschiedene Anwendungen in der Nanoelektronik als auch zur „Nanomanipulation“. Die Darstellung der Nanodrähte in wäßriger Lösung im Grammbereich bietet interessante Möglichkeiten für leitende Füllstoffe, da eine Mischung aus leitenden Materialien 10 mal weniger Material benötigt, falls Metallpartikel mit Drähten wechselwirken können.

Zur Erforschung des Verhaltens von fluoreszierenden Farbstoffen in der Umgebung von komplexeren Metallobjekten wurde auf einer Goldoberfläche eine Schicht Goldnanopartikel aufgebracht, die aber von dieser Goldoberfläche durch eine Lage eines Polymers wohldefinierter Größe abgetrennt waren. Die Eigenschaften dieses neu synthetisierten Systems wurden durch Oberflächen- und optische Analysenmethoden charakterisiert. Die optischen Eigenschaften der Goldnanopartikel sind stark abhängig von der Distanz zur Goldoberfläche.

Der nächste Schritt der Erforschung des in Kapitel 6 beschriebenen mehrschichtigen Systems wäre die Auftragung von fluoreszierenden Farbstoffen auf den Nanopartikeln. Das

Plasmonenfeld der Nanopartikel, angeregt durch das Oberflächenplasmon der flachen Goldfläche, könnte zu einer Veränderung der Emissionsrate der Fluorophore führen, was sich durch eine verstärkte Emission ausdrücken würde. Die direkte Konsequenz hieraus wäre eine erhöhte Sensitivität dieses Systems. Eine weitere mögliche Variation dieses Systems wäre die Auftragung eines Polymers als Abstandhalter um die Goldnanopartikel, was sowohl in Lösung als auch direkt auf der Oberfläche möglich ist. Dann wäre es möglich, den Einfluß des Abstandes zwischen der Oberfläche der Goldpartikel und des fluoreszierenden Farbstoffes zu untersuchen. Möglich wäre auch eine Abscheidung der Fluorophore zwischen zwei Goldpartikeln oder zwischen einem Goldpartikel und der Goldoberfläche. In diesem Fall würde die Verstärkung des elektromagnetischen Feldes zwischen den beiden Metalloberflächen die Lichtemission des Farbstoffes beeinflussen.

Diese Arbeit soll ein kleiner Schritt zum Verständnis des Verhaltens von fluoreszierenden Verbindungen in der Nähe von metallischen Grenzflächen sein. Zum vollständigen Verständnis dieser Phänomene ist zukünftig noch viel Arbeit notwendig. Aufgrund ihrer Komplexität erfordert die Erforschung dieses Phänomens die Zusammenarbeit von Wissenschaftlern, die in ein interdisziplinäres Team sowohl chemische als auch physikalische Erfahrung einbringen.